



UNIVERSIDADE FEDERAL DO RIO DE JANEIRO
INSTITUTO DE FÍSICA

**Consequences of H Doping in the Electronic and
Optical Properties of Carbon Nanotubes**

Rafael Rodrigues Del Grande

Tese de Doutorado apresentada ao Programa de Pós-Graduação em Física do Instituto de Física da Universidade Federal do Rio de Janeiro - UFRJ, como parte dos requisitos necessários à obtenção do título de Doutor em Ciências (Física).

Orientador: Rodrigo Barbosa Capaz
Coorientador: Marcos Gonçalves de Menezes

Rio de Janeiro

Junho de 2021

P436 Del Grande, Rafael Rodrigues

Consequences of H doping in the electronic and optical properties of Carbon Nanotubes / Rafael Rodrigues Del Grande - Rio de Janeiro: UFRJ/IF, 2021.

xiv, 154f.

Orientador: Rodrigo Barbosa Capaz

Coorientador: Marcos Gonçalves de Menezes

Tese (doutorado) - UFRJ / Instituto de Física / Programa de Pós-graduação em Física, 2021.

Referências Bibliográficas: f. 124-145.

1. Carbon Nanotubes Review.
 2. Theoretical Methods.
 3. Results and Discussions.
 4. Conclusions.
- I. Capaz, Rodrigo Barbosa.
II. Menezes, Marcos Gonçalvez de.
III. Universidade Federal do Rio de Janeiro, Instituto de Física, Programa de Pós-graduação em Física.
IV. Consequences of H doping in the electronic and optical properties of Carbon Nanotubes.

Resumo

Consequences of H doping in the electronic and optical properties of Carbon Nanotubes

Rafael Rodrigues Del Grande

Orientador: Rodrigo Barbosa Capaz

Coorientador: Marcos Gonçalves de Menezes

Resumo da Tese de Doutorado apresentada ao Programa de Pós-Graduação em Física do Instituto de Física da Universidade Federal do Rio de Janeiro - UFRJ, como parte dos requisitos necessários à obtenção do título de Doutor em Ciências (Física).

As propriedades óticas de Nanotubos de Carbono (NTC) são ditadas por efeitos excitônicos. Em espectros de absorção são observados picos E_{11} , E_{22} , etc, correspondentes a excitons compostos pelas transições de diferentes pares de bandas de valência e condução. As propriedades desses excitons dependem da quiralidade e diâmetro do tubo, e típicos valores de energias de ligação são da ordem de algumas centenas de meV, o que é muito maior do que no caso de semicondutores tridimensionais. Além disso, como NTCs são materiais unidimensionais, as suas propriedades excitônicas são altamente influenciadas pelo ambiente.

Na última década, vários trabalhos estudaram propriedades óticas de NTCs dopados covalentemente. Após essa funcionalização, novos picos são observados no espectro de absorção ótica. Estes novos picos são deslocados para o vermelho (têm menor energia e maior comprimento de onda) em relação aos picos observados em nanotubos puros e a magnitude desse deslocamento se relaciona com a natureza química dos grupos de

funcionalização ligados ao tubo. Ademais, estes picos são correlacionados com regiões específicas dos tubos, indicando que a região com defeito funciona com uma armadilha de excitons, diminuindo a energia dos picos de absorção. Alguns trabalhos interpretam esses picos deslocados para o vermelho como um exciton escuro presente em NTCs puros que se tornam claros após essa funcionalização.

Nesta tese nós combinamos cálculos *ab initio* e *tight binding* para NTCs zigzag dopados com átomos de hidrogênio para estudar a origem física desse fenômeno. Na estrutura eletrônica, vemos que a inclusão de defeitos quebra a degenerescência no topo (fundo) da banda de valência (condução) e cria uma banda de impureza constante (sem dispersão) no meio do gap. Na absorção ótica, vemos novos picos com energias menores do que o pico E_{11} original do tubo puro. Nossos resultados *ab initio* mostram que esses picos são associados a excitons compostos de transições envolvendo o estado de impureza, que é localizado em volta do defeito. Portanto, esses picos podem ser relacionados com picos deslocados para o vermelho observados experimentalmente e sua localização espacial. Além disso, encontramos novos estados escuros, descartando a possibilidade de que novos estados claros são provenientes estados escuros dos NTCs puros e que se tornaram claros. Nossos resultados são reforçados por análises de simetrias da densidade eletrônica dos estados de valência, condução e de impurezas que determinam que estados são acoplados entre si.

Palavras-chave: Excitons, Nanotubos de carbono, Defeitos, Localização, GW/BSE

Abstract

Consequences of H Doping in the Electronic and Optical Properties of Carbon Nanotubes

Rafael Rodrigues Del Grande

Orientador: Rodrigo Barbosa Capaz

Coorientador: Marcos Gonçalves de Menezes

Abstract da Tese de Doutorado apresentada ao Programa de Pós-Graduação em Física do Instituto de Física da Universidade Federal do Rio de Janeiro - UFRJ, como parte dos requisitos necessários à obtenção do título de Doutor em Ciências (Física).

The optical properties of carbon nanotubes (CNTs) are ruled by excitonic effects. In the optical spectra, the peaks E_{11} , E_{22} , etc, are observed and are related to excitons composed by transitions of different valence and conduction bands pairs. The excitons properties depend on the tube chirality and diameter, and typical binding energies are about a few hundreds of meV, which are much higher than typical binding energies in 3D semiconductors. Additionally, as CNTs are 1D materials, the excitonic properties are highly influenced by the environment.

In the last decade, several works studied the optical properties of sp³-doped CNTs. After this functionalization, new peaks are observed in the optical absorption spectrum. Those new peaks are redshifted with respect to the peaks observed in pristine CNTs and the magnitude of this redshift is related to the chemical nature of the functionalization group bonded to the tube. Moreover, these peaks are correlated to spatial regions of the CNTs, indicating that the defect site works as a trapping potential for excitons that

lowers the emission energy. Some works interpret this redshifted peak as a dark exciton from the pristine CNT that becomes bright after the functionalization.

In this thesis we perform a combination of *ab initio* and tight binding calculations for zigzag CNTs doped with hydrogen atoms in order to investigate the physical origin of these phenomena. In the electronic structure, we see that the defect lifts the degeneracies at the top (bottom) of the valence (conduction) band and induces a flat impurity band in the middle of the bandgap. In the optical absorption, we see new peaks with energies lower than that of the pristine E_{11} peak. Our *ab initio* results show that these peaks are associated to excitons composed of transitions involving the impurity state, which is localized around the defect site. Therefore, these peaks could be related to the experimentally observed redshifted peaks and their spatial localization. Additionally, new dark excitons are also found, ruling out the possibility that the new bright states result from dark states of the pristine tube that were brightened. Our results are also supported by a symmetry analysis of the electronic densities associated to the valence and conduction bands and the impurity state, which determines which states are coupled.

Keywords: Excitons, Carbon nanotubes, Defects, Localization, GW/BSE

Agradecimentos

Listar agradecimentos aqui, inclusive à agência de fomento que concedeu a bolsa de pós-graduação.

Contents

Abstract	viii
List of Figures	x
List of Tables	xxi
1 Carbon Nanotubes Review	1
1.1 Carbon Nanomaterials	1
1.2 Carbon Nanotubes Properties	3
1.2.1 Structure	3
1.2.2 Electronical properties	7
1.2.3 Symmetries	10
1.3 Excitons in Carbon Nanotubes	13
1.3.1 Excitons	13
1.3.2 Optical properties	16
1.3.3 Selection Rules	19
1.4 Exciton Localization	21
2 Theoretical Methods	25
2.1 Tight Binding Calculations	27
2.1.1 Theoretical Background	27
2.1.2 Computational Details	29

2.2	Density Functional Theory	32
2.2.1	Theoretical Background	32
2.2.2	Computational details	38
2.3	Many Body Perturbation Theory	40
2.3.1	GW approximation	43
2.3.2	Bethe-Salpeter Equation	47
2.3.3	Computational details	52
3	Results and Discussions	54
3.1	Pristine Carbon Nanotubes	54
3.2	Band Structure of Covalently Doped Carbon Nanotubes	57
3.3	Impurity Level	65
3.4	Optical Properties of Covalently Doped Carbon Nanotubes	70
3.5	Exciton Symmetries and Selection Rules	81
3.6	Binding Energy	93
4	Conclusions	97
References		99
A	Empty Cylinder Model	126
A.1	Pristine CNT	126
A.2	CNT-H	128

List of Figures

1.1	Schematic view of graphene generating others materials, respectively from left to the right: fullerene (0 dimensional), carbon nanotube (1 dimensional), graphite (3 dimensional). Figure reproduced from [1]	2
1.2	Left: hexagonal sublattices A and B of graphene. Right: graphene reciprocal lattice. First Brillouin zone and some high symmetry points (Γ , M , K and K'). Note that the reciprocal lattice is rotated by 30° in relation to the real space lattice. Figure reproduced from ref. [2]	4
1.3	Left: graphene lattice and the CNT chiral and translational vectors. Right: structure of armchair, zigzag and chiral CNTs. Figure adapted from ref. [3].	5
1.4	Example of cutting lines in graphene BZ.	6
1.5	Graphene's electronic dispersion. The inset focus on the Dirac cone localized around the K point. Fig. reproduced from ref. [2]. Note that in this plot second-neighbor interactions were included as there is an electron-hole asymmetry.	8
1.6	Cutting lines in graphene dispersion. Figure reproduced from [3].	8
1.7	Example of CNTs energy dispersions calculated using equation 1.12 for (8,0), (9,0), (4,4) and (4,2) CNTs, respectively from left to right.	10
1.8	Different ways of constructing CNT (4,2) structure: (a) helical-helical, (b) linear-helical and (c) helical-angular.	12

1.9 Kataura plot for E_{11} and E_{22} transition energies for semiconducting CNTs and E_{11} for metallic CNTs. Open and filled circles are for $\text{mod}(2n+m, 3) = 1$ and $\text{mod}(2n + m, 3) = 2$ (two different families of semiconductor CNTs) respectively and crossed circles are for metallic CNTs. Fig. reproduced from ref. [4] using original data from ref. [5].	16
1.10 Exemplification of how the screening behaves in low dimensional materials. In bulk 3D materials all electric field lines pass through the material and for low dimensional materials most of field lines pass through the surrounding environment. Fig. reproduced from ref. [6]	17
1.11 (a) The appearance of a new redshifted peak after the functionalization of CNT(6,5) with 4-nitrobenzenediazonium tetrafluoroborate. (b) Evolution in time of E_{11} and E_{11}^- peaks intensities since the functionalization started. (c) E_{11} and E_{11}^- peaks intensities for different concentrations of reactants. (a) and (b) correspond to diazonium salt to carbon molar ratio of 1:300. Fig. reproduced from ref. [7]	22
1.12 Normalized intensities of E_{11} and E_{11}^* peaks for CNTs functionalized with different reactants. The E_{11}^* signal is spatially localized. Fig. reproduced from ref. [8]	23
2.1 TB calculation in graphene with optimized parameters to reproduce DFT data.	30
2.2 Parameters convergence for CNT(11,0). p_1 , p_2 , p_3 and p_4 are the overlap s , first neighbor hopping, second neighbor hopping and third neighbor hopping, respectively. Blue dots are the parameters that shows the best fits in that generation (step).	31

2.3 Bandsctruture for CNTs (8,0), (10,0) and (11,0). Black dashed lines are GW calculations, red lines are TB calculations including overlap and hopping until third neighbors and blue lines are calculations just including hopping between first neighbors.	33
2.4 Schematic algorithm to solve self-consitently the Kohn-Sham equations. The σ index indicates the spin degree of freedom, which is not discussed in this work. Figure reproduced from ref. [9]	39
2.5 Supercell size	40
2.6 Convergence of χ_{00} and $\chi_{\mathbf{G}_m \mathbf{G}_m}$ as a function of the energy cutoff for the construction of χ matrix. \mathbf{G}_m is the last vector used in the matrix evaluation. That is why $\chi_{\mathbf{G}_m \mathbf{G}_m}$ is not well converged as χ_{00} . In those calculations we used 12 k points in our grid.	45
2.7 ε_{00}^{-1} for CNT(11,0) with different k point samplings. In those calculations we used 400 empty conduction bands in the summations.	46
2.8 Theoretical band gap calculated at DFT (using LDA exchange correlation functional) and GW level versus experimental bandgap for several semiconductors. The perfect agreement is on the diagonal line. Data from [10] .	48
2.9 GW gap as a function of the number of conduction bands for different cutoff energies in epsilon. In those calculations 12 k points were used in grids.	49
2.10 GW gap as function of the number of k points included in calculations. In those calculations 300 empty conduction bands were included and a cutoff of 10 Ry was used to construct the dielectric matrix.	50

2.11 Left: Example of absorption spectra evaluated at three different levels: with electron-hole interaction (in black) and without it using GW (green) and DFT (red) results. Right: Bandstructures at DFT (red lines) and GW (black lines) levels. Note that the GW bands gap is greater than the DFT gap. The bands that give rise to the E_{11} and E_{22} absorption peaks are indicated. Those results are for CNT(11,0).	51
2.12 Convergence of E_{11} (a) and E_{22} (b) absorption peaks for NTC (11,0) with respect to the number of K points in coarse grid and number of bands for epsilon and sigma. The number of K points in the fine grid is eight times the number of K points in the coarse grid. $E_{22} - E_{11}$ difference (c) and binding energy (d) for those two excitons.	53
3.1 Left: bandstructure from of (8,0), (6,5), (10,0) and (11,0) pure CNTs at DFT (red lines) and GW levels (black lines). The E_{11} exciton energy and its binding energy are also indicated for each case. Right: Gap at Γ point at DFT and GW levels as a function of the tube diameter (in ascending order: (8,0), (6,5), (10,0) and (11,0)).	54
3.2 Absorption spectra for pure CNTs for different chiralities (indicated in the figure) evaluated at DFT, GW and BSE levels.	55
3.3 Example of exciton wavefunction as a function of the distance between the electron and the hole for the pristine (10,0) CNT. The dashed black curve is given by $e^{-(z_e-z_h)^2/\sigma^2}$ where σ is given by eq. 3.2.	57
3.4 Band structure of pristine (black dashed lines) and CNT(10,0)-H (red solid line) calculated at DFT level. The double degenerate valence (conduction) band of pristine CNT splits in the v_1 and $v_{1'}$ (c_1 and $c_{1'}$) of the functionalized CNT and an impurity band i emerges in the middle of the bandgap.	59

3.5 Bandstructure at DFT level of CNT(10,0)-H with different supercell sizes (indicated in the figure) and different net charges. Red lines, blue lines and green lines are $q = 1$, $q = -1$ and $q = 0$ cases respectively.	60
3.6 Main gap (a), splits of the first two valence bands (b), splits of the first two conduction bands (c) and impurity level (d) as function of the number of unit cells included in calculations (lower label) or the linear concentration of defects (upper label). Square (circle) symbols correspond to calculations at GW (DFT) level and red, blue and green symbols are calculations with $q = +1$, $q = -1$ and $q = 0$ respectively.	61
3.7 TB dependence of the splits of the valence (conduction) band and the impurity state as a function of the unit cells included in the calculation for CNT(10,0)-H. TB parameters used for the calculation are the ones in the first row of table 3.2.	62
3.8 DFT bandstructures for (8,0), (10,0) and (11,0) CNTs with four unit cells (defect concentration equals to 0.6 defect/nm). Red lines, blue lines and green lines correspond to net charges of $q = 1$, $q = -1$ and $q = 0$ respectively.	62
3.9 Logarithm of the electronic density in polar coordinates for the impu- rity state in calculations with 4 (a), 6 (b), 8 (c) and 10 (d) unit cells of CNT(10,0)-H. The atomic positions are presented as well. The linear elec- tronic density in the axial and radial directions are also presented and were calculated by $ \psi(z) ^2 = \int r dr d\theta \psi(z, \theta, r) ^2$ and $ \psi(\theta) ^2 = \int r dr dz \psi(z, \theta, r) ^2$. The hydrogen atom is represented by the pink star at the origin.	63

3.10 Electronic density in polar coordinates for the c_1 , $c_{1'}$, $v_{1'}$ and v_1 bands states in calculations with 10 unit cells of CNT(10,0)-H. The atomic positions are presented as well. The linear electronic density in the axial and radial directions are also presented and were calculated by $ \psi(z) ^2 = \int r dr d\theta \psi(z, \theta, r) ^2$ and $ \psi(\theta) ^2 = \int r dr dz \psi(z, \theta, r) ^2$. The hydrogen atom is represented by the pink star at origin.	64
3.11 Linear electronic density along the z direction for the impurity band for calculations with $L= 4(a)$, $6(b)$, $8(c)$ and $10(d)$ unit cells. Black dashed lines are gaussian functions $e^{-(z/\sigma)^2}$, where σ is the standard deviation given by eq. 3.3. Those results are calculations at DFT level with $q = 0$	66
3.12 Localization length of the impurity state calculated at DFT level. Green, red and blue symbols correspond to $q = 0$, $q = 1$ and $q = -1$, respectively. This data was fitted with the expression $\delta(L) = \delta_0(1 - \exp(-L/L_c))$ (dashed lines) in each case. The fitted parameters are shown in the legend of the figure and their unit is nanometers.	67
3.13 Impurity state and split of the conduction and valence bands calculated at DFT level for different quantities of defect concentration and doping. The doping was calculated until the maximum (minimum) value to make the impurity band totally full (empty).	68
3.14 Impurity level E_i and splits Δ_v and Δ_c varying the parameters t_{HC} and E_{0H} (see text) calculated at TB level for the CNT(10,0)-H with four unit cells. Black, red and blue solid lines are level curves where the difference between TB results and DFT results for CNT(10,0)-H with $q = 0$, $q = +1$ and $q = -1$, respectively, are less than 10^{-3} . In the first panel dots are the best TB parameters to reproduce the DFT impurity level and are listed in table 3.2	69

3.15 TB band structure of CNT(10,0) bonded to 1 H (a) or 10 H (b and c) atoms. (b) and (c) are calculations done with the same concentration of defects but are different random samples. Those calculations were done with 20 unit cells in the supercell (supercell length is 8.4 nm and it contains 800 carbon atoms).	70
3.16 Distribution of impurity levels considering all 100 calculations for sev- eral defect concentrations, indicated in each subpanel which units are de- fect/nm. Black dashed lines represent the bottom of the conduction band and the top of the valence band is set to zero.	71
3.17 Impurity level (upper panel), split of the conduction band (middle panel) and split of the valence band (lower panel) as a function of the defect concentration.	71
3.18 Mean DOS for several defect concentrations. The linewidth in each case is twice the standard deviation of the samples.	72
3.19 Absorption spectra at DFT (left) and BSE (right) levels for CNT(10,0)-H with charge $q = 0$ (green curves), $q = 1$ (red curves) and $q = -1$ (blue curves) for different supercell sizes. Black dashed lines are results for E_{11} in pristine CNT ($q = 0$) for reference.	72
3.20 Redshifts in the absorption spectra taking the E_{11} transition energy as reference and at BSE level for CNT(10,0)-H with charge $q = +1$ (red lines) and $q = -1$ (blue lines). Supercell sizes are indicated in the figure.	74
3.21 (a-d): Peak positions for E_{11} (black symbols) and E_- (red symbols) ex- citons calculated with BSE (a and b) and at DFT level (c and d). (e-f): Binding energies for E_{11} (black symbols) and E_- excitons (red symbols). (g-h) Redshifts ($ E_- - E_{11} $) calculated using BSE (squares) and DFT (cir- cles) results. Left (right) panels are results for $q = 1$ ($q = -1$).	75

3.22 Absorption spectra for (8,0) (a and b), (10, 0) (c and d) and (11, 0) (e and f) without defect (black lines) and with hydrogen atoms (0.6 H atoms per nm) and with charge $q = 1$ (red curves) and $q = -1$ (blue curves). DFT results are in the left and BSE results are in the right.	76
3.23 Redshifts in the absorption spectra of (8,0) (a), (10, 0) (b) and (11, 0) (c) without defect (black lines) and with hydrogen atoms (0.6 H atoms per nm) and with charge $q = 1$ (red curves) and $q = -1$ (blue curves) at BSE level.	77
3.24 Results for (8,0), (10,0) and (11,0) CNTs. (a-d): Peak positions for E_{11} (black symbols) and E_- (red symbols) excitons calculated with BSE (a and b) and at DFT level (c and d). (e-f): Binding energies for E_{11} (black symbols) and E_- excitons (red symbols). (g-h) Redshifts ($ E_- - E_{11} $) calculated using BSE (squares) and DFT (circles) results. Left (right) panels are results for $q = 1$ ($q = -1$) and black empty circles are results for the E_{11} peaks in pristine CNTs (see table 3.1).	78
3.25 Ratio between the intensities of the first redshifted peak and the E_{11} peak calculated using BSE. Red (blue) symbols are calculations for CNT(10,0) bonded to H with net charge $q = 1$ ($q = -1$).	79
3.26 Absorption spectra calculated at TB level (except the black dashed line, which was calculated at GW level without e-h interaction) for several defects concentrations. In each curve, the linewidth is twice the standard deviation of the samples. The sample size for each case is 20.	80

3.27 Dark (black lines) and bright excitons (colored lines) for CNT bonded with hydrogen atom for different number of unit cells included in calculations. Green lines are the E_{11} excitons for each case and blue (red) lines are bright excitons for calculations with $q = -1$ ($q = 1$). Calculations were done for pristine CNT and supercells with 4, 6, 8 and 10 unit cells (indicated in the figure).	82
3.28 Dark (black lines) and bright excitons for CNT bonded with hydrogen atom for different diameters. Green, red and blue lines are bright excitons for the cases of pristine tube, CNT-H with $q = 1$ and CNT-H with $q = -1$, respectively.	83
3.29 Optical absorption at BSE level (upper panel) and exciton composition (lower panel) for different number of unit cells for CNT(10,0)-H with $q = 1$. In the lower panels the bright (dark) excitons are colored (dark) vertical lines. Bright excitons are associated to absorption peaks by vertical dashed lines. In the upper panel black dashed line is the optical absorption of pristine CNT(10,0).	84
3.30 Optical absorption at BSE level (upper panel) and exciton composition (lower panel) for different number of unit cells for CNT(10,0)-H with $q = -1$. In the lower panels the bright (dark) excitons are colored (dark) vertical lines. Bright excitons are associated to absorption peaks by vertical dashed lines. In the upper panel black dashed line is the optical absorption of pristine CNT(10,0).	85

3.31 Absolute value of dipole transition matrix elements for different transitions evaluated at DFT level for negatively charged ($q = -1$) CNT(10,0)-H for several tube lengths. Black (continuous) dashed lines are optical absorptions evaluated at DFT level for CNT(10,0)-H (pristine CNT(10,0)). From the top to the bottom the unit cell length is: 1.7nm, 2.5nm, 3.4nm and 4.2nm.	87
3.32 Absolute value of dipole transition matrix elements for different transitions evaluated at DFT level for CNT(10,0)-H with unit cell length 4.2 nm with $q = 0, \pm 1$ (indicated in each panel).. Black (continuous) dashed lines are optical absorptions evaluated at DFT level for CNT(10,0)-H (pristine CNT(10,0))	88
3.33 Optical absorption at BSE level (upper panel) and exciton composition (lower panel) for pristine CNT(8,0) (left) and CNT(8,0)-H with $q = 1$ (middle) and $q = -1$ (right), where the concentration of defects is 0.6 defect/nm. In the lower panels the bright (dark) excitons are colored (dark) vertical lines. Bright excitons are associated to absorption peaks by vertical dashed lines. In the upper panels (b) e (c) green dashed line is the optical absorption of pristine CNT(8,0).	90
3.34 Optical absorption at BSE level (upper panel) and exciton composition (lower panel) for pristine CNT(11,0) (left) and CNT(11,0)-H with $q = 1$ (middle) and $q = -1$ (right), where the concentration of defects is 0.6 defect/nm. In the lower panels the bright (dark) excitons are colored (dark) vertical lines. Bright excitons are associated to absorption peaks by vertical dashed lines. In the upper panels (b) e (c) green dashed line is the optical absorption of pristine CNT(11,0).	91

List of Tables

1.1	Irreducible representations for the valence and conduction bands of zigzag CNTs. If $\tilde{\mu} < 2n/3$ valence (conduction) band has $E_{\tilde{\mu}u}$ ($E_{\tilde{\mu}g}$) representation for $\tilde{\mu}$ even and $E_{\tilde{\mu}g}$ ($E_{\tilde{\mu}gu}$) for $\tilde{\mu}$ odd, and when $\tilde{\mu} > 2n/3$ it is the opposite [3].	12
2.1	Tight binding parameters	32
3.1	Exciton properties of pristine CNTs	58
3.2	Optimal TB parameters that reproduce DFT results for CNT(10,0)-H with four unit cells and net charges $q = 0, \pm 1$. The hopping between carbon atoms is still $t_{CC} = 4.681\text{eV}$ and on-site energies for carbon atoms are zero.	67
3.3	Compatibility relations	86
3.4	Bright exciton compositions for CNT(8,0) and CNT(8,0)-H ($q = \pm 1$) . . .	91
3.5	Bright exciton compositions for CNT(11,0) and CNT(11,0)-H ($q = \pm 1$) . . .	92
3.6	Point groups for different geometries of zigzag CNTs bonded to two hydrogen atoms. Configurations can be seen in Fig. 3.35.	93

Chapter 1

Carbon Nanotubes Review

1.1 Carbon Nanomaterials

Carbon nanomaterials have gained attention in the last years, specially sp^2 based carbon nanomaterials [1, 2, 4, 11–18] due to their physical properties that are very diverse depending on their dimensionality.

The fullerene molecule (C_{60}) was discovered by Kroto, Curl and Smalley [19, 20] who won the Nobel Prize in Chemistry in 1996. The C_{60} molecule is a 0D material composed of 60 equivalent carbon atoms and it has the shape of a soccer ball. Not just C_{60} has been studied but also numerous others including C_{70} , C_{80} , etc [21]. An illustration of this molecule is shown in Fig. 1.1.

Graphene is a two-dimensional crystal where the carbon atoms are arranged in a honeycomb structure. It was first synthesized in 2004 by Geim and Novoselov [1, 14, 17, 22] by mechanical exfoliation of graphite. They won the Nobel Prize in Physics in 2010. Graphene's energy dispersion is linear around the K and K' points of its Brillouin Zone (BZ) and it is analogous to the physics of quantum electrodynamics for massless Dirac fermions with speeds 300 times smaller than the speed of light c [2]. New phenomena arise from this as the anomalous integer quantum Hall effect [2, 23]

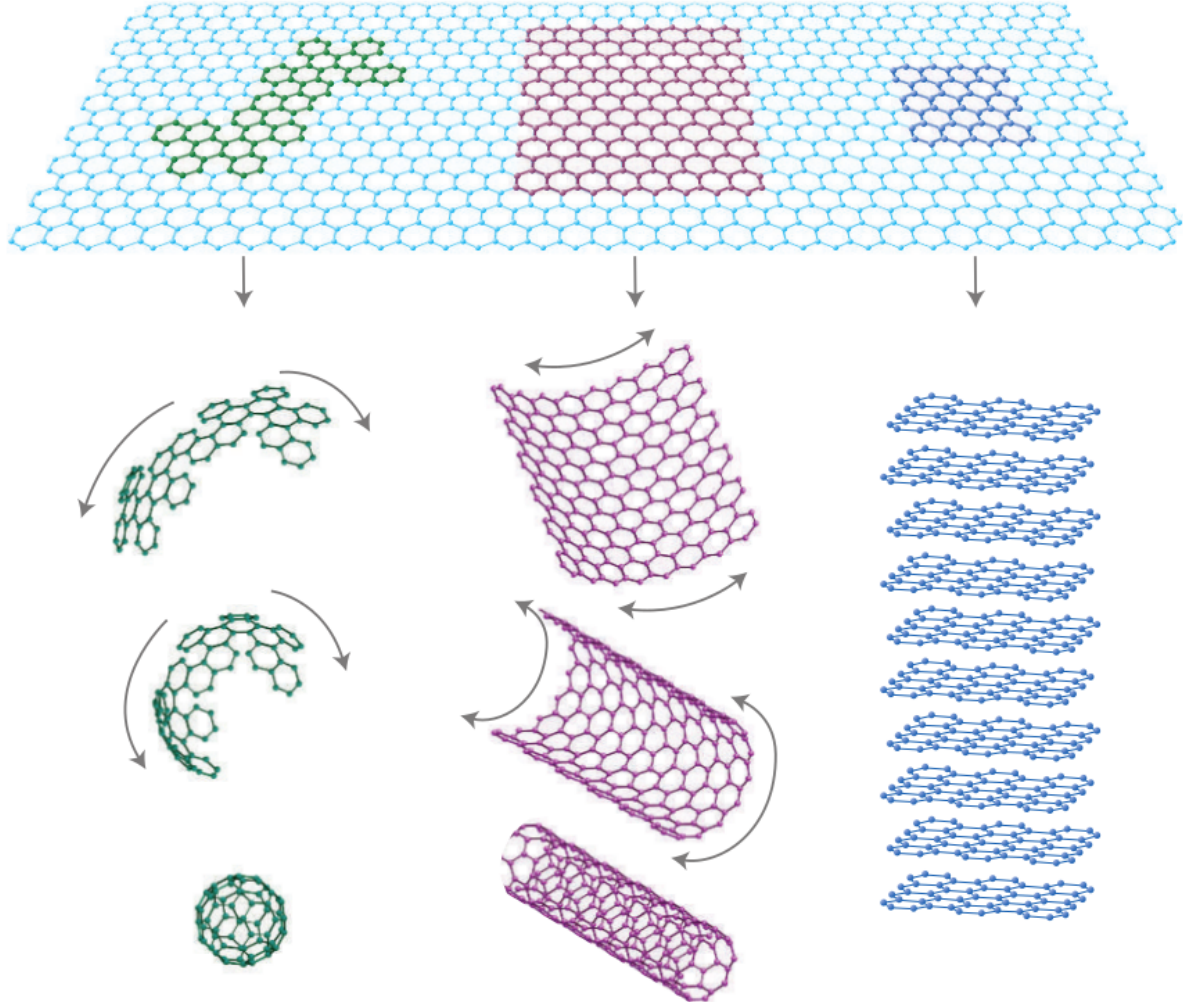


Figure 1.1: Schematic view of graphene generating others materials, respectively from left to the right: fullerene (0 dimensional), carbon nanotube (1 dimensional), graphite (3 dimensional). Figure reproduced from [1]

The graphene research called attention to other 2D materials such as MoS_2 and WS_2 and its van der Waals heterostructures, where two or more layers of different materials are stacked together bound by van der Walls interactions [24–27]. Multilayer graphene has attracted attention as well. The electronic and mechanical properties depend on the number of layers and their stacking. Particularly, we have calculated at DFT level frequencies of shear and layer breathing modes of N -layer graphene ($N = 1, 2, 3, 4, 5, 6$) and we observed that those frequencies depend on the number of layers and the highest frequency converges to the graphite case [28].

Another degree of freedom in 2D layered materials is the relative twist angle among layers. This gave rise to a new sub area of 2D materials called twistronics [29–34]. In bilayer graphene, twists give rise to Moiré patterns and Cao et. al found a magic angle around $\theta \approx 1.1^\circ$ where superconductivity was observed [35, 36]. We published a work studying the electronic structure of twisted double bilayer graphene where we observed flat bands for a range of angles between $1.1^\circ - 1.23^\circ$ [37]

Carbon Nanotubes (CNTs) are cylindrical molecules with typical lengths that range from nanometers to few micrometers and diameters that are less than few nanometers. They were synthesized for the first time in 1991 [38]. Those tubes may be metallic or semiconductors depending on their chirality [3]. We published a work that focused on the mechanical properties of CNTs in which we studied the collapse of tubes due to the van der Waals attraction between opposite walls [39].

In the 2000 decade, several works studied CNTs and discovered that their optical properties are ruled by excitonic effects [4, 40, 41]. From 2010 to now, several works studied optical properties of covalent functionalized CNTs [42–44]. In this work we study this system theoretically and in the next sections we discuss general properties of CNTs, and then we review the literature on this topic.

1.2 Carbon Nanotubes Properties

1.2.1 Structure

CNTs can be understood as rolled graphene layers, although CNTs are not synthesized from graphene. First, we need to look at the graphene structure, which is composed of two hexagonal sublattices: A and B (see Fig. 1.2). The primitive vectors are given by

$$\begin{aligned}\mathbf{a}_1 &= a \left(\frac{\sqrt{3}}{2}, \frac{1}{2} \right) \\ \mathbf{a}_2 &= a \left(\frac{\sqrt{3}}{2}, -\frac{1}{2} \right)\end{aligned}\tag{1.1}$$

and the basis can be defined as

$$\begin{aligned}\boldsymbol{\tau}_A &= (0, 0) \\ \boldsymbol{\tau}_B &= a \left(\frac{2}{\sqrt{3}}, 0 \right)\end{aligned}\tag{1.2}$$

where $a = 2.46\text{\AA}$ is the lattice parameter and the bond length is $d_{CC} = a/\sqrt{3} = 1.42\text{\AA}$.

The reciprocal lattice vectors are given by

$$\begin{aligned}\mathbf{b}_1 &= \frac{2\pi}{a} \left(\frac{1}{\sqrt{3}}, 1 \right) \\ \mathbf{b}_2 &= \frac{2\pi}{a} \left(\frac{1}{\sqrt{3}}, -1 \right)\end{aligned}\tag{1.3}$$

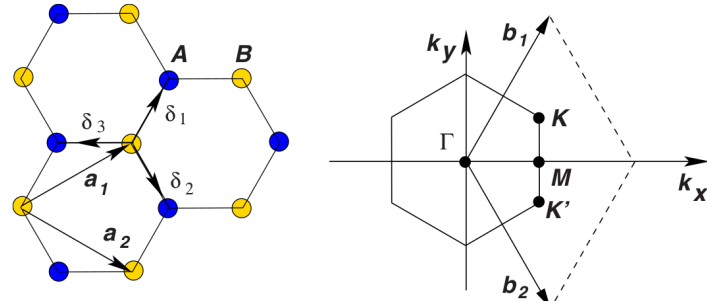


Figure 1.2: Left: hexagonal sublattices A and B of graphene. Right: graphene reciprocal lattice. First Brillouin zone and some high symmetry points (Γ , M, K and K'). Note that the reciprocal lattice is rotated by 30° in relation to the real space lattice. Figure reproduced from ref. [2]

The CNT structure [3, 45] can be understood as a rolled graphene sheet defined by a so-called chiral vector (see Fig. 1.3), given by

$$\mathbf{C}_h = n\mathbf{a}_1 + m\mathbf{a}_2\tag{1.4}$$

where n and m are positive integer numbers and the tube diameter is given by $d_t = |\mathbf{C}_h|$.

The chiral angle is the angle between the chiral vector and \mathbf{a}_1 as indicated in Fig. 1.3.

The CNTs are classified by the (n, m) indexes. If $n = m$ the tube is called “armchair”, if $n > m = 0$ the tube is called “zigzag” and if $n > m > 0$ the tube is called chiral. Those structures are shown in Fig. 1.3. The CNT diameter and chiral angle can be written as $d_t = a\sqrt{n^2 + nm + m^2}/\pi$ and $\tan \theta = \sqrt{3}m/(2n + m)$.

The translation vector \mathbf{T} is a vector perpendicular to \mathbf{C}_h and its magnitude is the CNT lattice constant (different from a , which is the graphene lattice constant). \mathbf{T} is given by

$$\mathbf{T} = t_1 \mathbf{a}_1 + t_2 \mathbf{a}_2 \quad (1.5)$$

where $t_1 = (2m + n)/d_R$ and $t_2 = -(2n + m)/d_R$ and d_R is the greatest common divisor of $2n + m$ and $2m + n$ ($\text{gcd}(2n + m, 2m + n)$). The length of \mathbf{T} is $\sqrt{3}C_h/d_R$.

In Fig. 1.3 all atoms of the tube unit cell lie inside the area delimited by \mathbf{C}_h and \mathbf{T} . The total number of hexagons inside this area is $N = 2(n^2 + nm + m^2)/d_R$ and the total number of carbon atoms is $2N$.

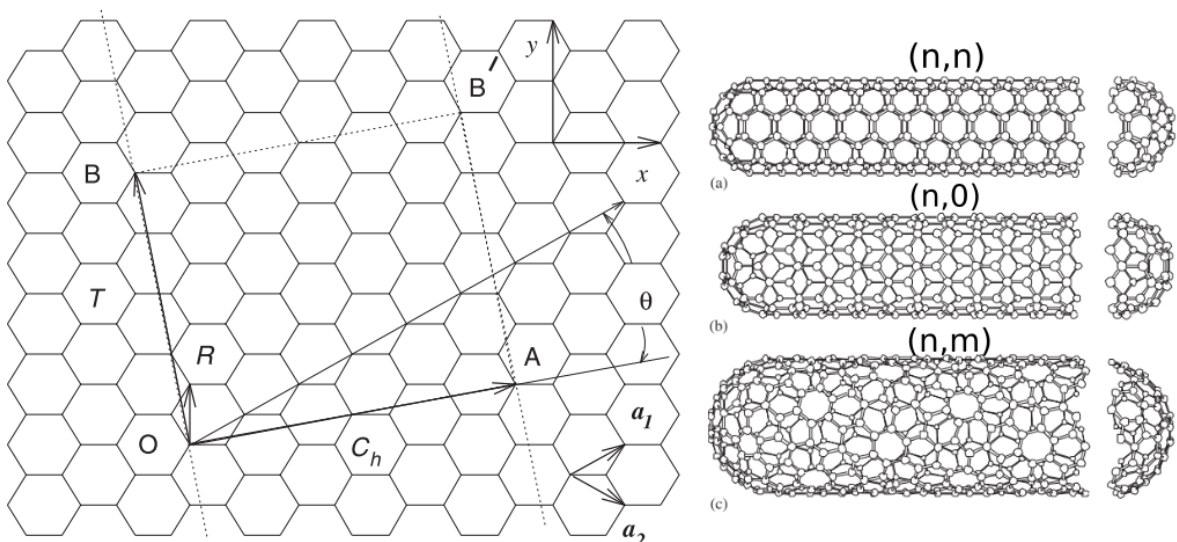


Figure 1.3: Left: graphene lattice and the CNT chiral and translational vectors. Right: structure of armchair, zigzag and chiral CNTs. Figure adapted from ref. [3].

CNTs are periodic just in the direction parallel to \mathbf{T} , so the primitive reciprocal vector is $\mathbf{G}_1 = 2\pi/T\hat{z}$. Diferently from \mathbf{T} , \mathbf{C}_h plays a role of generator of rotations, then we can define a vector \mathbf{G}_2 , which obeys $\mathbf{T} \cdot \mathbf{G}_2 = 0$ and $\mathbf{C}_h \cdot \mathbf{G}_2 = 2\pi\mu$, where $\mu = \text{integer}$. With that, \mathbf{G}_2 must be a vector parallel to \mathbf{C}_h and its modulus is given by $2\pi\mu/d_t$. As \mathbf{T} and \mathbf{C}_h are orthogonal to each other, so are \mathbf{G}_1 and \mathbf{G}_2 .

As an example, let's consider the $(n, 0)$ zigzag CNTs. The chiral vector is given by $\mathbf{C}_h = n\mathbf{a}_1$, $d_R = n$ and $\mathbf{T} = \mathbf{a}_1 - 2\mathbf{a}_2$, which is perpendicular to \mathbf{C}_h . \mathbf{T} modulus is $a\sqrt{3} = 4.26\text{\AA}$ and it is independent of n . In this case there are $2N = 4n$ ($N = 2n$) carbon atoms (hexagons) in a unit cell. The reciprocal lattice vectors are integer multiples of $\mathbf{G}_1 = 2\pi/(a\sqrt{3})\hat{T}$ and $\mathbf{G}_2 = (\pi\mu/na)\hat{a}_1$, where \hat{T} (\hat{a}_1) is the unitary vector parallel to \mathbf{T} (\mathbf{a}_1).

The cutting line method [3,12,46–48] maps the CNT reciprocal space into the graphene reciprocal space, so we can obtain an approximate CNT electronic dispersion from graphene. In Fig. 1.4 we show the \mathbf{G}_1 and \mathbf{G}_2 vectors in the graphene reciprocal space. The CNT allowed states lie over the lines parallel to \mathbf{G}_1 . Those parallel lines are separated by a distance equal to $2\pi/d_t$ from each other. The total number of lines is N and each line has an index μ where it can be $\mu = -N/2 - 1, \dots, 0, \dots, N/2 - 1, N/2$ (or alternatively $\mu = 0, 1, \dots, N - 1$).

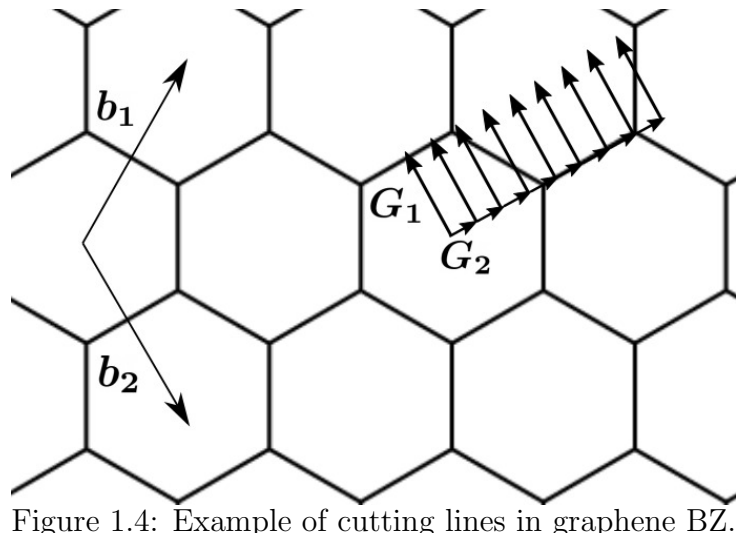


Figure 1.4: Example of cutting lines in graphene BZ.

1.2.2 Electronical properties

We will explain the basic features of CNT electronic structure based on graphene's properties.

In graphene, each carbon atom is bonded to three first neighbors, as shown in Fig. 1.2. In a tight-binding (see section 2.1) approach, the hamiltonian for p_z orbitals of graphene is given by

$$H(\mathbf{k}) = -t \begin{pmatrix} 0 & f(\mathbf{k}) \\ f^*(\mathbf{k}) & 0 \end{pmatrix} \quad (1.6)$$

where t is the first-neighbor hopping and

$$f(\mathbf{k}) = \sum_{\tau_i} \exp(i\mathbf{k}\tau_i) = \exp\left(\frac{ik_x a}{\sqrt{3}}\right) + 2 \exp\left(-\frac{ik_x a}{2\sqrt{3}}\right) \cos\left(\frac{k_y a}{2}\right) \quad (1.7)$$

The electronic dispersion is given by

$$E_{graph}(\mathbf{k}) = \pm t|f(\mathbf{k})| \quad (1.8)$$

where the $+$ ($-$) sign stands for the conduction (valence) band.

Around the K point the dispersion is approximately given by $E(\mathbf{q}-\mathbf{K}) \approx (\sqrt{3}ta/2)|\mathbf{q}|$, which is a conical dispersion (see Fig. 1.5) and $\sqrt{3}ta/2 = v_F \approx 10^{-6}\text{m/s}$ is the Fermi velocity [2,49]. Graphene is a zero gap semiconductor.

The eigenvectors [2,12] are given by

$$\psi(\mathbf{r}) = \frac{1}{\sqrt{2}} (p_z(\mathbf{r} - \mathbf{R}_A) \pm e^{i\Theta} p_z(\mathbf{r} - \mathbf{R}_B)) \quad (1.9)$$

where $R_{A(B)}$ is the atomic position of a carbon atom in the sublattice A(B), $p_z(\mathbf{r} - \mathbf{R}_A)$ are Bloch sums over localized p_z orbitals in the sublattice A and

$$e^{i\Theta} = \frac{f(\mathbf{k})}{|f(\mathbf{k})|} \quad (1.10)$$

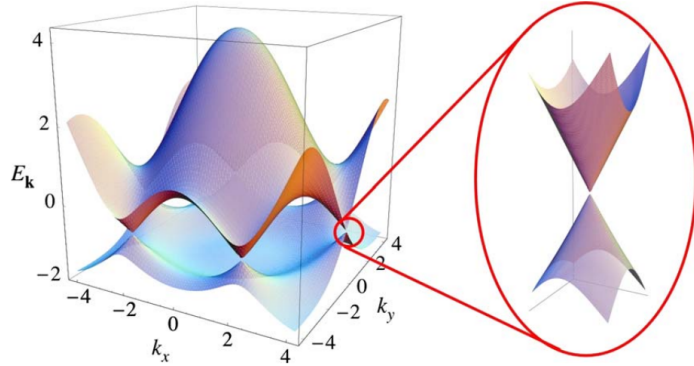


Figure 1.5: Graphene’s electronic dispersion. The inset focus on the Dirac cone localized around the K point. Fig. reproduced from ref. [2]. Note that in this plot second-neighbor interactions were included as there is an electron-hole asymmetry.

For $e^{i\Theta} = 1$ the above equation is a symmetric (anti-symmetric) combination of atomic orbitals in case of the sign equals to + (−), corresponding to the valence (conduction) state.

In a CNT unit cell there are $2N$ carbon atoms, therefore there are N valence (conduction) bands. In the cutting lines scheme each pair of conduction and valence bands is associated to a cutting line with index μ and those cutting lines placed over the graphene dispersion give rise to the CNT dispersion, as shown in Fig. 1.6.

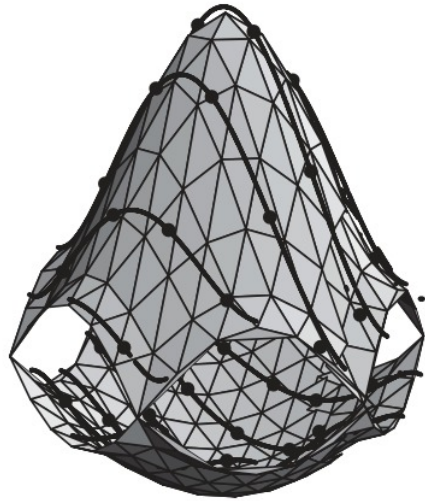


Figure 1.6: Cutting lines in graphene dispersion. Figure reproduced from [3].

For a CNT band with index μ at a given k_z point of the CNT BZ, the respective k_{graph}

point in the graphene BZ is

$$k_{graph} = k_z \mathbf{G}_1 + \mu \frac{\mathbf{G}_2}{|\mathbf{G}_2|} \quad (1.11)$$

Then the CNT dispersion for the bands with index μ is given by [47, 50–52]

$$E_\mu(k_z) = E_{graph} \left(k_z \mathbf{G}_1 + \mu \frac{\mathbf{G}_2}{|\mathbf{G}_2|} \right) \quad (1.12)$$

and the corresponding eigenvector is given by [53, 54]

$$\psi_{\mu,k_z}^{v(c)}(\mathbf{r}) = \frac{1}{\sqrt{2N}} \sum_{j=1}^N e^{i\Theta_{\mu,k}} e^{i\mathbf{k}\cdot\mathbf{R}_A^j} p_z(\mathbf{r} - \mathbf{R}_A^j) \pm e^{i\mathbf{k}\cdot\mathbf{R}_B^j} p_z(\mathbf{r} - \mathbf{R}_B^j) \quad (1.13)$$

where

$$\mathbf{k} \cdot \mathbf{R}_A^j = \mu \theta_A^j + k_z z_A^j \quad (1.14)$$

The p_z orbitals in the above equation point in the radial direction. The cutting lines approach is valid for sufficiently high diameter CNTs. For small diameter cases curvature effects emerge and there is a rehybridization of atomic orbitals, so an extended tight binding model including other orbitals is necessary [55].

In expression 1.12, it is possible to see that if the cutting lines pass through the K point, then the CNT is metallic, otherwise the tube is semiconductor. The condition for the tube to be metallic is that $n - m = 3l$ with $l = \text{integer}$. For non-armchair "metallic" tubes, a small gap opens due to curvature effects. In Fig. 1.7 we show some examples calculated using eq. 1.12.

Armchair $((n, n))$ tubes are metallic and their band crossing is between the Γ and X points. Semiconductor (metallic) zigzag tubes $((n, 0))$ show a minimum band gap (band crossing) at the Γ point and chiral tubes show two minimum band gaps in two different points k and $-k$ between Γ and X points.

The main gap in semiconducting CNTs relates to the hopping t by [11, 49, 52, 56]

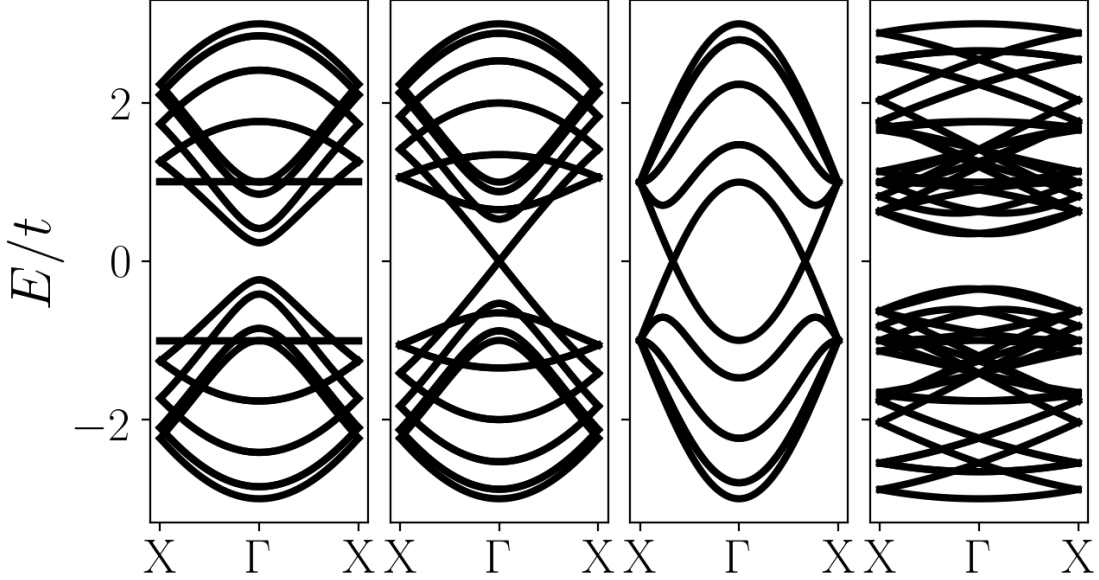


Figure 1.7: Example of CNTs energy dispersions calculated using equation 1.12 for (8,0), (9,0), (4,4) and (4,2) CNTs, respectively from left to right.

$$E_g(n, m) = \frac{2d_{CC}t}{d_t} \quad (1.15)$$

1.2.3 Symmetries

CNTs belong to nonsymmorphic space groups, which means that they belong to space groups that include screw axes operations (operations that involve fractional translations of the Bravais lattice) [3, 45].

By looking at the unfolded CNT structure (the area in Fig. 1.3 delimited by \mathbf{C}_h and \mathbf{T}) a general symmetry operation is given by the vector

$$\mathbf{t}_{p,q} = p\mathbf{a}_1 + q\mathbf{a}_2 \quad (1.16)$$

where p and q are integer numbers. Those symmetries operations are screw translations in CNTs (a combination of a rotation R_ϕ by an angle ϕ and a small translation τ , that is represented by $\{R_\phi|\tau\}$).

This vector can be written in terms of \mathbf{C}_h and \mathbf{T} as

$$\mathbf{t}_{p,q} = \mathbf{t}_{u,v} = \frac{u}{N} \mathbf{C}_h + \frac{v}{N} \mathbf{T} \quad (1.17)$$

where $u = ((2n+m)p + (2m+n)q)/d_R$ and $v = mp - nq$.

Then $\mathbf{t}_{u,v}$ can be written as an space group element given by

$$\mathbf{t}_{u,v} = \{C_N^u | vT/N\} \quad (1.18)$$

where C_N^u is rotation of $u(2\pi)/N$ and $\{E|vT/N\}$ is pure translation of vT/N (E is the identity operator).

As $\{C_N^u | vT/N\}$ is a symmetry operation of CNTs, so does $\{C_N^u | vT/N\}^s$ (with s integer) and $\{C_N^u | vT/N\}^N$ is equal to $\{E|vT\}$. The nanotube structure can be constructed by two noncollinear screw vectors $\{C_N^{u_1} | v_1 T/N\}$ and $\{C_N^{u_2} | v_2 T/N\}$ and there are numerous combinations for those vectors as shown in Fig. 1.8. In refs [57, 58] a symmetry tight binding model is used to calculate electronic properties of CNTs with the advantage of using just two carbon atoms in a unit cell (as shown in Fig. 1.8). The helical-helical (see Fig. 1.8-a) construction can be originated by making $\mathbf{t}_1 = \mathbf{a}_1$ and $\mathbf{t}_2 = \mathbf{a}_2$ with 2 atoms per unit cell, the linear-helical (helical-angular) is originated by making one of the vectors parallel to \mathbf{a}_1 and the other parallel to \mathbf{T} (\mathbf{C}_h), as show in the Fig. 1.8-b (1.8-c) and the linear-angular construction can be achieved by making $\mathbf{t}_1 = \mathbf{T}$ and $\mathbf{t}_2 \parallel \mathbf{C}_h$ and this construction does not allow a two atoms unit cell. In the particular case of zigzag CNTs we have that $\mathbf{t}_1 = \mathbf{T}$ and $\mathbf{t}_2 = \mathbf{C}_h/n$ in the linear-angular construction.

The irreducible representations of the factor groups of CNTs are labeled by the quasiangular momentum number $\tilde{\mu}$ ($1 - N/2 \leq \tilde{\mu} \leq N/2$) which is associated to the $\{R_\phi|\tau\}$ operation projected in the circumferential direction [3, 59]. The quantum number $\tilde{\mu}$ can be associated to the cutting line indexes.

Now we focus our discussion on zigzag CNTs, as our calculations are performed mostly

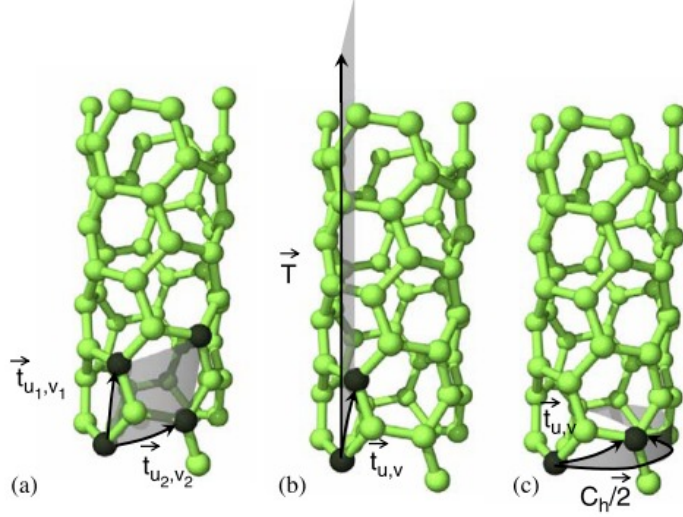


Figure 1.8: Different ways of constructing CNT (4,2) structure: (a) helical-helical, (b) linear-helical and (c) helical-angular.

for those kind of tubes. For a detailed discussion on armchair and chiral CNTs see ref. [3]. The group of the wavevector for $k = 0$ and $k = \pi/T$ ($0 < k < \pi/T$) of CNT $(n, 0)$ is isomorphic to the point group D_{2nh} (C_{2nv}) and its character table and compatibility relations may be found in ref. [3]. The C_{2nv} (D_{2nh}) group has four (eight) 1D representations and $(n-1)$ ($2(n-1)$) 2D representations. Cutting lines with indexes μ and $-\mu$ are associated to the same 2D irreducible representation with index $\tilde{\mu}$. Valence and conduction bands with index $0 < \tilde{\mu} < n$ have $E_{\tilde{\mu}}$ symmetry, when $\tilde{\mu} = 0$ their symmetry is A and when $\tilde{\mu} = n$ their symmetry is B . The irreducible representations for the valence and conduction bands are then summarized in the Table 1.1. Those representations play a crucial role in the discussion of selection rules (see section 1.3.3).

Point group	Valence		Conduction	
	D_{2nh} $k = 0, \pi/T$	C_{2nv} $0 < k < \pi/T$	D_{2nh} $k = 0, \pi/T$	C_{2nv} $0 < k < \pi/T$
$\tilde{\mu} = 0$	A_{1g}	A'	A_{2u}	A'
$0 < \tilde{\mu} < n$	$E_{\tilde{\mu}u, \tilde{\mu}g}$	$E_{\tilde{\mu}}$	$E_{\tilde{\mu}g, \tilde{\mu}u}$	$E_{\tilde{\mu}}$
$\tilde{\mu} = n$	B_{1g}	B'	B_{2u}	B'

Table 1.1: Irreducible representations for the valence and conduction bands of zigzag CNTs. If $\tilde{\mu} < 2n/3$ valence (conduction) band has $E_{\tilde{\mu}u}$ ($E_{\tilde{\mu}g}$) representation for $\tilde{\mu}$ even and $E_{\tilde{\mu}g}$ ($E_{\tilde{\mu}gu}$) for $\tilde{\mu}$ odd, and when $\tilde{\mu} > 2n/3$ it is the opposite [3].

1.3 Excitons in Carbon Nanotubes

The optical properties of semiconductor CNTs are dominated by excitonic effects [4, 60], then in this section we will first review some aspects of the theory of excitons and then look at excitons in CNTs. For more detailed reviews see refs [4, 13, 56, 61]

1.3.1 Excitons

An exciton is bound electron-hole pairs. When an electron is excited from a valence to a conduction band, a hole is created, then there is an attractive Coulomb potential between those two quasiparticles. Generally, the exciton wavefunction in a solid is given by

$$|\Psi\rangle = \sum_{\mathbf{k},v,c} A_{\mathbf{k},v,c} a_{\mathbf{k},c}^\dagger b_{\mathbf{k},v}^\dagger |G\rangle \quad (1.19)$$

where $a_{\mathbf{k},c}^\dagger$ ($b_{\mathbf{k},v}^\dagger$) creates an electron (hole) in the conduction (valence) band, $A_{\mathbf{k},v,c}$ are coefficients to be determined and $|G\rangle$ represents the system ground state. In our work, the coefficients $A_{\mathbf{k},v,c}$ are determined by the Bethe-Salpeter Equation (BSE) and this method is explained in section 2.3.2.

Another way of writing eq. (1.19) is

$$\Psi(\mathbf{r}_e, \mathbf{r}_h) = \sum_{\mathbf{k},v,c} A_{\mathbf{k},v,c} \psi_{\mathbf{k},c}(\mathbf{r}_e) \psi_{\mathbf{k},v}(\mathbf{r}_h) \quad (1.20)$$

The excitons are classified as Frenkel excitons if the typical electron-hole distance is smaller than a lattice constant or Wannier excitons when the electron hole distance is large when compared to the lattice constant and the pair is weakly bound [62]. In the case of semiconductor CNTs the exciton size is about a few nanometers (see Table 3.1) [63], so we focus on Wannier excitons.

In general, $A_{\mathbf{k},v,c}$ is a localized function in k space, which we can approximate to $A_{\mathbf{k},v,c} \approx A_{0,v,c} e^{-(k-k_0)^2/\Delta k^2}$ for a transition centered in \mathbf{k}_0 . By considering that an exciton is composed by one valence band and one conduction band, we write the exciton

wavefunction as

$$\Psi(\mathbf{r}_e, \mathbf{r}_h) = F(\mathbf{r}_e - \mathbf{r}_h)\psi_c(\mathbf{r}_e)\psi_v(\mathbf{r}_h) \quad (1.21)$$

where $F(\mathbf{r}_e - \mathbf{r}_h)$ is an envelope function. In the Appendix A we calculate the exciton wavefunction in the empty cylinder model.

We will follow the discussion of refs. [64, 65]. Let's consider an electron in the conduction band with effective mass m_e^* and a hole in the valence band with effective mass m_h^* . Those quasiparticles interact with each other by a Coulomb attraction, so the Schrödinger equation for the two-particle system is given by

$$\left(-\frac{\hbar^2 \nabla_e^2}{2m_e^*} - \frac{\hbar^2 \nabla_h^2}{2m_h^*} - \frac{e^2}{4\pi\epsilon r_{eh}} \right) \Psi = E\Psi \quad (1.22)$$

where ϵ is the macroscopic dielectric constant of the material.

Assuming that the exciton is just composed by one electron in the conduction band and one hole in the valence band, we can write Ψ as

$$\Psi = g(\mathbf{R})f(\mathbf{r}) \quad (1.23)$$

where $\mathbf{r} = \mathbf{r}_e - \mathbf{r}_h$ is the electron hole separation and $\mathbf{R} = (\mathbf{r}_e + \mathbf{r}_h)/2$ is the average electron-hole coordinate. We can rewrite the gradients as $\nabla_R = (\nabla_e + \nabla_h)/2$ and $\nabla_r = \nabla_e - \nabla_h$.

We have that $\mathbf{p}_R = -i\hbar\nabla_R$ commutes with the above hamiltonian, so $g(\mathbf{R}) = e^{i\mathbf{KR}}$. Then we have the following equation for $f(r)$

$$\left(\frac{p_r^2}{2\mu} - \frac{e^2}{4\pi\epsilon r} - \frac{\hbar}{2} \left(\frac{1}{m_e^*} - \frac{1}{m_h^*} \right) \mathbf{K} \cdot \mathbf{p} \right) f(r) = \left(E - \frac{\hbar^2 K^2}{8\mu} \right) f(r) \quad (1.24)$$

where μ is the exciton reduced mass and is given by

$$\frac{1}{\mu} = \frac{1}{m_e^*} + \frac{1}{m_h^*} \quad (1.25)$$

By introducing the following transformation

$$f(\mathbf{r}) = e^{i\alpha\mathbf{K}\cdot\mathbf{r}} F(\mathbf{r}) \quad (1.26)$$

with $\alpha = (1/2)(m_e^* - m_h^*)/(m_e^* + m_h^*)$, eq. 1.24 becomes

$$\left(\frac{p^2}{2\mu} - \frac{e^2}{4\pi\epsilon r} \right) F(\mathbf{r}) = \left(E - \frac{\hbar^2 K^2}{2(m_e^* + m_h^*)} \right) \quad (1.27)$$

The above transformations are equivalent to change to the center of mass coordinate $\mathbf{R} = (m_e \mathbf{r}_e + m_h \mathbf{r}_h)/(m_e + m_h)$.

The solutions for eq. 1.27 are the same of the hydrogenic problem, which we call $F_{lmn}(\mathbf{r})$. The eigenvalues are given by

$$E_n(\mathbf{K}) = \frac{\hbar^2 K^2}{2(m_e^* + m_h^*)} - \frac{\mu e^4}{2\hbar^2 \epsilon^2 n^2} \quad (1.28)$$

where the first term is center of mass kinetic energy and the second is the Rydberg series. When $K = 0$ the exciton may decay directly by emitting a photon and if $K \neq 0$ the decay process needs phonons due to momentum conservation.

The wavefunction is given by

$$\Psi_{lmn, \mathbf{K}}(\mathbf{r}_e, \mathbf{r}_h) = e^{i\mathbf{K}\cdot(\mathbf{R}+\alpha\mathbf{r})} F_{lmn}(\mathbf{r}) \quad (1.29)$$

The energy to separate the electron-hole pair (exciton binding energy) is $\mu e^4 / (2\hbar^2 \epsilon^2) \approx 0.01 \text{ eV}$ for most bulk semiconductors. The exciton radius is given by $a_{\text{ex}} = a_0 \epsilon m_e / \mu$, where $a_0 = 0.529 \text{ \AA}$ is the Bohr radius. For semiconductors $m_e/\mu > 1$ and $\epsilon \approx 10 - 20$, so $a_{\text{ex}} \approx 100 a_0$, which justifies the Wannier approach of extended excitons [62].

Equation 1.28 is valid for 3D excitons with isotropic dispersion. For 2D excitons, the dispersion in the case of isotropic dispersion is given by [66]

$$E(K) = E_0 + A|K| + \frac{\hbar^2 K^2}{2M} \quad (1.30)$$

while 1D excitons have the general dispersion [66]

$$E(K) = E_0 + BK^2 \log |K| + \frac{\hbar^2 K^2}{2M} \quad (1.31)$$

In low dimensional materials the exciton binding energies do not follow Rydberg series because the dielectric function has a spatial dependence [5, 6, 67–71] (see section 1.3.2).

1.3.2 Optical properties

In the 2000's decade, the scientific community concluded that the optical properties of CNTs are ruled by excitonic effects [4, 5, 41, 63, 67, 68, 72–77], even in the case of metallic CNTs [78, 79]. The E_{ii} transitions (transitions from the i -th valence band to the i -th conduction band) are highly dependent on the tube chirality and diameter [40, 58, 80–83], as shown in Fig. 1.9.

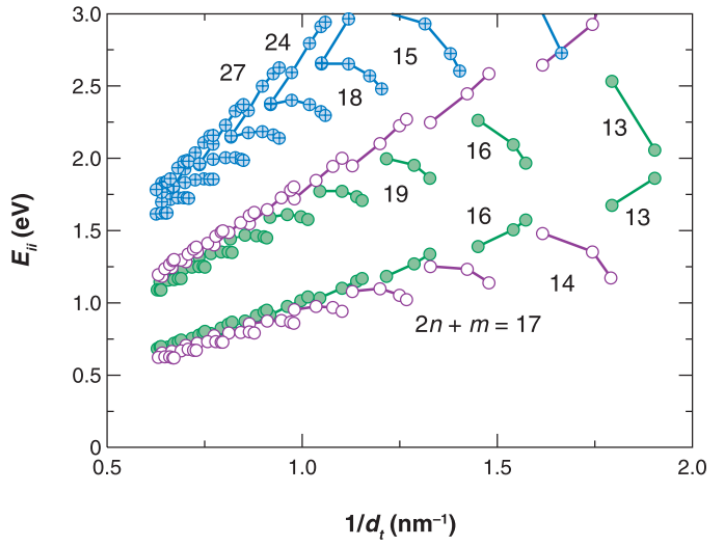


Figure 1.9: Kataura plot for E_{11} and E_{22} transition energies for semiconducting CNTs and E_{11} for metallic CNTs. Open and filled circles are for $\text{mod}(2n + m, 3) = 1$ and $\text{mod}(2n + m, 3) = 2$ (two different families of semiconductor CNTs) respectively and crossed circles are for metallic CNTs. Fig. reproduced from ref. [4] using original data from ref. [5].

Exciton binding energies in CNTs are about hundreds of meV (see table 3.1) which are much higher than usual binding energies in bulk 3D semiconductors. In low dimensional

materials the screening is nonlocal and shows a very different behavior than in 3D cases, as most of the electric field lines do not pass through the material (see Fig. 1.10).

For example, in WS_2 (a 2D layered material) the potential between two point charges is not the Coulomb potential but a sum of Struve and Bessel functions [6, 69], which diverges logarithmically when $r \rightarrow 0$ (r is the distance between the two charges) instead of $1/r$ (the Coulomb potential) that diverges faster than $\log(r)$. Such potential leads to a non hydrogenic series for the excitonic binding energies. Similar behavior is seen in CNTs [41, 67, 68]. For low dimensional materials (1D and 2D) the dielectric function goes to unity at both large and small wavelengths, which means that there is no screening at both short and large separation distances [5, 6, 68–71].

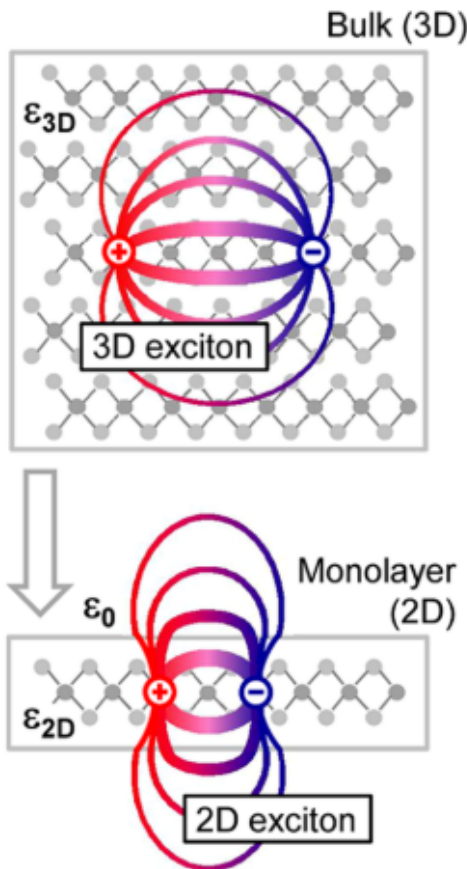


Figure 1.10: Exemplification of how the screening behaves in low dimensional materials. In bulk 3D materials all electric field lines pass through the material and for low dimensional materials most of field lines pass through the surrounding environment. Fig. reproduced from ref. [6]

Due to its low dimensionality, the surrounding screening environment changes the emission energies substantially [61, 84–89]. Other effects such as electrical doping [90–94] and stress [95] change peak positions as well. So, the sensitivity of absorption peaks to those effects may be used in applications on optical devices.

Not all excitons present in CNTs are directly accessible by optical experiments. Direct optical processes occur when the exciton center of mass momentum is nearly zero (equal to the photon momentum E/c , which is much smaller than the BZ boundaries), otherwise finite momentum phonons are necessary. In addition to that, selection rules also dictate if the optical process is allowed or not [3, 59] (to be discussed in section 1.3.3). The optical active (inactive) excitons are called bright (dark) excitons. Besides that, dark excitons play an important role in the temperature dependence of photoluminescence (PL) experiments [96–99]. The lowest dark exciton energy is lower than the lowest bright exciton [100, 101], what explains the low quantum efficiency of CNTs [102]. The split between the first bright and dark excitons decreases when the tube diameter increases [96, 101, 103] and in ref. [85] it is found to be proportional to d_t^{-2} (d_t is the tube diameter). Dark excitons become bright when magnetic fields are applied on CNTs due to the Aharonov-Bohm effect [101].

As excitons are excited quasiparticles, they have a radiative lifetime which is the expected time necessary to a exciton to decay emitting photons. Typical values for PL lifetimes for bright excitons range between 20 to 200 ps even for individual tubes [56, 99, 104] and those radiative times increase with the tube diameter [87, 100]. In ref. [99] the intrinsic lifetime was found to be too large to be determined experimentally. Large discrepancies for radiative lifetimes arise from extrinsic effects such as defects in the CNTs [104].

1.3.3 Selection Rules

Now we discuss optical processes involving excitons in CNTs from a symmetry point of view. In this section, we consider excitons with center of mass momentum equal to zero.

In optical processes the electromagnetic interaction is given by the following term

$$H' = -\frac{e}{2mc} \mathbf{p} \cdot \mathbf{A} \quad (1.32)$$

where \mathbf{A} is the vector potential and is parallel to the polarization direction of the incident radiation. The perturbation transforms as a vector of the group of Schrödinger's equation [45]. For light polarized parallel to the tube axis, H' will transform as the vector z , which transform as the A_{2u} (A_2) Irreducible Representation (IRREP) for achiral (chiral) CNTs at the Γ point. For light polarized perpendicular to the tube axis, H' will transform as vectors x and y , which transform as the E_1 (E_{1u}) IRREP for chiral (achiral) CNTs. For zigzag CNTs the conduction and valence bands IRREPS are listed in Table 1.1.

Let's consider a Wannier exciton composed by just one valence and one conduction band. Using equation 1.21, we may write it as [3, 59]

$$\Psi_{\text{ex}}(\mathbf{r}_e, \mathbf{r}_h) = F_\nu(z_e - z_h) \psi_c(\mathbf{r}_e) \psi_v(\mathbf{r}_h) \quad (1.33)$$

where the index $\nu = 0, 1, 2, \dots$ indicates the envelope function parity that can be even (for ν even) or odd (for ν odd) under the operation $z \rightarrow -z$.

The irreducible representation (IRREP) of the excitonic state will be given by the direct product of the valence band IRREP, conduction band IRREP and the envelope function IRREP

$$D(\Psi_{\text{ex}}) = D(\psi_c) \otimes D(\psi_v) \otimes D(F_\nu) \quad (1.34)$$

Here we discuss the optical processes for zigzag CNTs. For more detailed discussions, see ref. [3].

Let's first consider the exciton associated to transitions between bands with the same $\tilde{\mu}$ indexes.

At the Γ point the valence and conduction bands transform as $E_{\tilde{\mu}g}$ and $E_{\tilde{\mu}u}$ (one has even and the other has odd parity) IRREPs of the D_{2nh} group. Those representations are 2D and correspond to degenerate states. Then the combination of those two bands leads to four excitonic states, whose symmetries are given by

$$E_{\tilde{\mu}g} \otimes E_{\tilde{\mu}u} \otimes A_{1g} = A_{1u} + A_{2u} + E_{\tilde{\mu}'u} \quad (1.35)$$

for ν even (the representation for F_ν is A_{1g}) and

$$E_{\tilde{\mu}g} \otimes E_{\tilde{\mu}u} \otimes A_{2u} = A_{2g} + A_{1g} + E_{\tilde{\mu}'g} \quad (1.36)$$

for ν odd (the representation for F_ν is A_{2u}).

As the light polarized parallel (perpendicular) to the tube axis transforms as A_{2u} (E_1), the only bright exciton is the A_{2u} exciton that appears for $F_{\nu=\text{even}}$ and light parallel to the tube axis. The transitions associated to this exciton are the E_{ii} transitions.

Now, let's consider excitons associated to transitions between bands with the different $\tilde{\mu}_1$ and $\tilde{\mu}_2$ indexes.

In this case, the valence and conduction bands may have the same or opposite parities and bright excitons come from transitions where $\tilde{\mu}_1 = \tilde{\mu}_2 \pm 1$, which are also known as $E_{i,\pm i}$ transitions.

For valence and conduction bands with same parity

$$E_{\tilde{\mu}\pi} \otimes E_{(\tilde{\mu}\pm 1)\pi} \otimes A_{1g(2u)} = E_{\tilde{\mu}'g(\tilde{\mu}'u)} + E_{1g(1u)} \quad (1.37)$$

and for valence and conduction bands with opposite parities

$$E_{\tilde{\mu}\pi} \otimes E_{(\tilde{\mu}\pm 1)\pi'} \otimes A_{1g(2u)} = E_{\tilde{\mu}'u(\tilde{\mu}'g)} + E_{1u(1g)} \quad (1.38)$$

where π indicates the parity (u or g).

For light perpendicular to the tube axis, bright double degenerate excitons are present for $\nu = \text{odd(even)}$ when the conduction and valence bands parities are the same (opposite).

Optical transitions with the polarization of light perpendicular to the tube axis occur, although their intensities are much smaller than in cases where the light is parallel to the tube axis [56, 61, 100, 105]. Group theory predicts whether optical transitions are allowed by symmetry but can not predict their intensities.

1.4 Exciton Localization

In 2010's decade, several experimental [7, 8, 42, 43, 106–130] and theoretical works [123, 126, 130–136] studied the optical properties of CNTs with covalent bonded defects. As those molecules bind to the CNTs, new redshifted peaks appear in the photoluminescence (PL) experiments, with shifts around 100–400 meV from the native E_{11} peak. Generally those redshifted peaks are called E^* or E^- peaks. As the defect concentration increases, the E_{11} (E^*) peak intensity decreases (increases) [7, 42, 109, 114, 120, 124, 125]. Similar redshifts are also observed theoretically in CNTs with vacancies and Stone-Wales defects [137, 138], which are important in the case of CNTs exposed to high intensity light beams.

As a representative example, we show in Fig. 1.11 results from Ref. [7]. In this experimental work, after the functionalization with 4-nitrobenzenediazonium tetrafluoroborate of CNT(6,5) a new redshifted peak was observed, called E_{11}^- . Both E_{11} and E_{11}^- peaks intensities were highly dependent on the defect concentration and the new redshifted peak shows an intensity higher than the native peak.

The energy difference between the E_{11} peak and E^* is proportional to d^{-2} (d is the tube diameter) in the case of tubes functionalized with aryl groups [7]. Environment (solvents, for example) effects also affect those redshifts [108, 115, 134, 135, 139] as well as the conformation and interaction among defects along the tube [115, 121, 123, 131, 134, 135]. In general, the presence of covalently bonded defects in CNTs is confirmed by observing

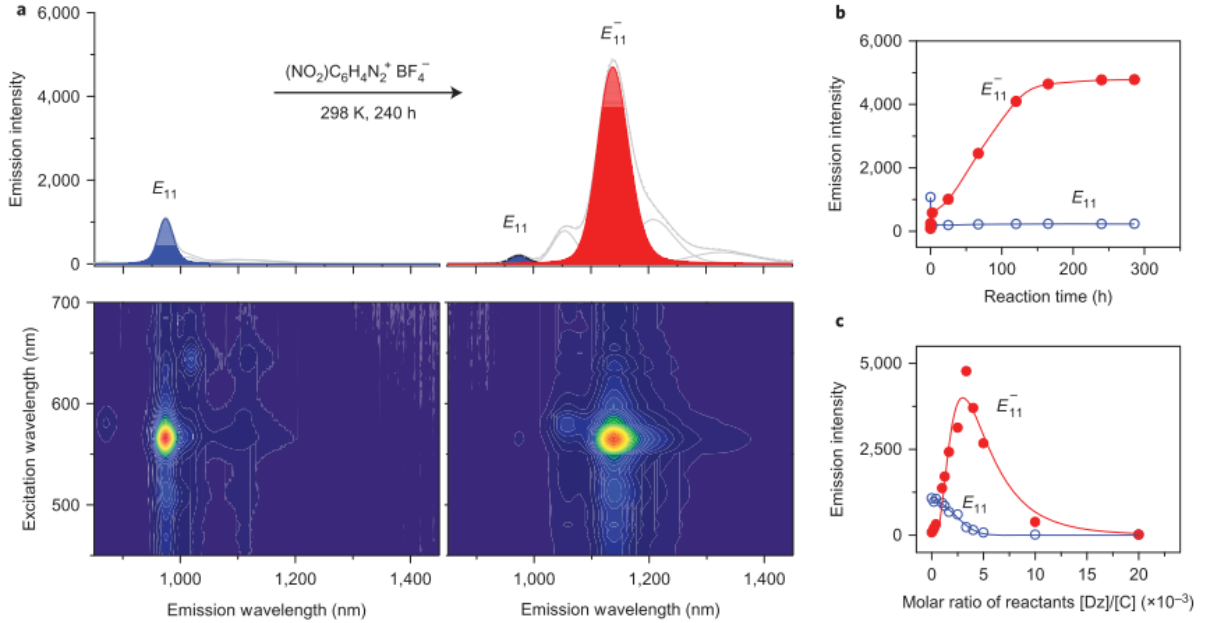


Figure 1.11: (a) The appearance of a new redshifted peak after the functionalization of CNT(6,5) with 4-nitrobenzenediazonium tetrafluoroborate. (b) Evolution in time of E_{11} and E_{11}^- peaks intensities since the functionalization started. (c) E_{11} and E_{11}^- peaks intensities for different concentrations of reactants. (a) and (b) correspond to diazonium salt to carbon molar ratio of 1:300. Fig. reproduced from ref. [7]

the evolution of the ratio between the D peak and G peak in Raman Spectroscopy [7, 111, 116, 124] and X-ray photoelectron spectroscopy [111].

In Ref. [140] after hydrogen adsorption, redshifted peaks were observed with shifts fitted to $\Delta E = 68[\text{meV}]/d^2$, where d is given in nanometers. Those new peaks were associated to triplet dark excitons as the theoretical predictions matched the experimental values for the (20, 0) CNT [140].

In Ref. [111] it is observed that the redshifts are given by $\Delta E = A/d^2$ for CNT functionalized with C_6F_{13} groups, (where $A = 18.7\text{meV}/\text{nm}^2$) suggesting that the new peaks arises from brightening of dark excitons as those values are close to the splitting between bright and dark excitons and show the same $1/d^2$ dependence [96, 141, 142]. Other works associate those redshifted peaks to dark states of the pristine tube that were brightened by vacancies [106] or covalently bonded groups in the CNTs [7]. Dark excitons play an important role in the temperature dependence of the PL spectra of CNTs and the

splitting between dark and bright excitons is about 1-10 meV [96, 142]. Bright to dark and vice versa mechanism are important to evaluate the radiative lifetimes observed in PL peaks [7, 109]. In ref. [119], variable temperature PL experiments showed that defects were responsible for the scattering of excitons from dark to bright states.

Hartmann et. al [8] correlated the redshifted peak to dopant sites localization in CNTs using a 2-color PL imaging technique and observed a blinking mechanism. In Fig. 1.12 we show those PL images, where the redshifted peaks intensities are spatially localized. Wu et. al [122] accomplished to identify single defects in CNTs by acquiring PL spectra for all pixels in a full image.

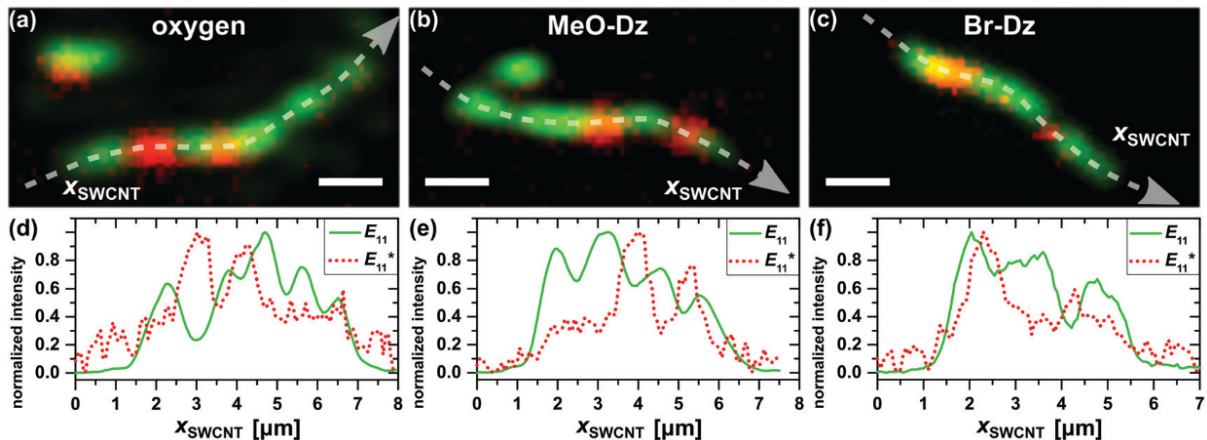


Figure 1.12: Normalized intensities of E_{11} and E_{11}^* peaks for CNTs functionalized with different reactants. The E_{11}^* signal is spatially localized. Fig. reproduced from ref. [8]

In ref. [94] the localization of pristine native excitons and trions is due to counterions adsorbed in the CNT surface interacting with free charges in electric doped CNTs with typical localizations lengths about 4 nm. In Ref. [132] theoretical calculations provided scaling laws for the exciton localization and redshift of the localized exciton as a function of the impurity effective charge and distance from the CNT surface. In Ref. [143] trions trapped in alkyl functional groups have shown binding energies about 100 meV. More redshifted peaks relate to more localized excitons [126, 135].

Those new redshifted excitons have lifetimes higher than the lifetime of the E_{11} exciton [107, 109]. In Ref. [109] the increase of aryl defects concentration reduce the E_{11}

excitons lifetime and trapped excitons show lifetimes 5-10 times higher than lifetimes of free excitons. The decay mechanism is related to the coupling of bright and dark excitons with phonons [7, 109].

The main explanation is that a trapping potential around the defect captures the native exciton associated to the E_{11} peak as locally the defect decreases the NTC electronic bandgap [42, 128]. This redshift depends on the defect chemistry nature, the tube diameter and chirality [7, 109, 111, 114, 116, 128]. This shift depends on the Hammet constant for aryl defects [7, 109, 111, 116, 144] or the Taft constant for alkyl defects [144], in other words, it depends on the capability of this defect to withdraw/donate electrons from/to the CNT. Even different isomers bonded in the CNT give different redshifts [128]. In [116] meta-aryl groups showed redshifts about 1-5meV higher than redshifts from para-aryl groups.

In Ref. [131], Time Dependent Density Functional Theory (TDDFT) calculations were performed for CNTs bonded with two hydrogen atoms (to maintain the aromaticity) in several configurations. Their results suggest a redistribution of oscillator strengths among states.

According to Density Functional Theory (DFT) calculations reported in Ref. [111] carbon atoms near the defect acquire net charges and in Ref. [123] shows a correlation between the redshift and the net charges of CNT atoms directly bonded to the defect.

CNTs bonded to covalent defects are good candidates for optoelectronical applications as the chemical nature of the bonded defect and the CNT chirality tunes the redshifted peak position [8, 43, 121]. Several works had success to produce room temperature single-photon emitters at telecom wavelengths towards quantum photonic applications [43, 118, 145].

For interesting reviews on the subject, please see references [56, 118, 128, 129].

Chapter 2

Theoretical Methods

In this work we used three different electronic structure methods: *Tight Binding* (TB), *Density Functional Theory* (DFT) and *Many Body Perturbation Theory*, specifically the GW approximation followed by the solution of the Bethe-Salpeter Equation (BSE). Each one has a level of complexity and, in general, the more complex is the method, more computational demanding it is and, in principle, more accurate as well.

DFT and GW/BSE are so called *ab initio* methods, which means that those methods are fundamental quantum calculations whose necessary experimental information are just atomic positions. On the other hand, TB is an empirical method where information from experiments or *ab initio* data are included such as band gap energies, hopping energies or effective masses for example.

All of the above methods deals with the following electronic hamiltonian

$$H = H_{\text{el}} + H_{\text{el-ion}} + H_{\text{ion-ion}} \quad (2.1)$$

where we are considering a system (ie. a molecule or a crystal) where the ion positions are fixed and we already used the Born-Oppenheimer (BO) approximation. The BO approximation is justified as we are studying semiconductor CNTs with bandgaps much higher than the typical ionic kinetic energy. Also, in this work we are just dealing with

direct vertical transitions, where the crystal momentum variation is null and phonons are not included.

The first term in eq. 2.1 is given by

$$H_{el} = -\frac{\hbar^2}{2m_e} \sum_i \nabla_i^2 + \frac{e^2}{4\pi\epsilon_0} \sum_{i>j} \frac{1}{|\mathbf{r}_i - \mathbf{r}_j|} \quad (2.2)$$

where the first term is the kinetic energy and the second is the sum of the Coulomb repulsion between electron pairs and a electron i is localized at the position \mathbf{r}_i .

The second term is given by

$$H_{el-ion} = \sum_{i,A} V_{el-ion}(\mathbf{R}_A - \mathbf{r}_i) \quad (2.3)$$

where \mathbf{R}_A is the ion A position and V_{el-ion} is the Coulomb attraction between the electron and the atomic nucleus modified by the screening of core electrons (electrons not involved in covalent bonding and in deeper electronic levels) [146, 147]. As the ions are kept fixed, we can consider this potential as an external potential over the electrons as

$$H_{el-ion} = \sum_i V(\mathbf{r}_i) \quad (2.4)$$

The last term is given by

$$H_{ion-ion} = \sum_{A,B} V_{ion-ion}(\mathbf{R}_A - \mathbf{R}_B) \quad (2.5)$$

and as the ions positions are kept fixed this term is a constant value in our calculations.

Now we can rewrite the electronic hamiltonian more clearly as

$$H_{el} = \sum_i \underbrace{-\frac{\hbar^2 \nabla_i^2}{2m_e}}_{h_1(\mathbf{r}_i)} + V(\mathbf{r}_i) + \sum_{i>j} \underbrace{\frac{1}{4\pi\epsilon_0 |\mathbf{r}_i - \mathbf{r}_j|}}_{h_2(\mathbf{r}_i - \mathbf{r}_j)} \quad (2.6)$$

where h_1 (h_2) is the one-body (two-body) part of this hamiltonian.

2.1 Tight Binding Calculations

2.1.1 Theoretical Background

The tight binding method consists of writing the hamiltonian eigenvectors $\psi_n(\mathbf{r})$ as a linear combination of atomic orbitals $\varphi(\mathbf{r} - (\mathbf{R}_A + \boldsymbol{\tau}_i))$, where \mathbf{R}_A is a lattice vector and $\boldsymbol{\tau}_i$ is the atomic positions inside a periodic cell:

$$\psi_n(\mathbf{r}) = \sum_A \sum_i c_{i,n} \varphi(\mathbf{r} - (\mathbf{R}_A + \boldsymbol{\tau}_i)) \quad (2.7)$$

In the case of crystals we can use the Bloch theorem

$$\psi_{n,\mathbf{k}}(\mathbf{r}) = \sum_A \sum_i c_{i,n,\mathbf{k}} e^{i\mathbf{k}(\mathbf{R}_A + \boldsymbol{\tau}_i)} \varphi(\mathbf{r} - (\mathbf{R}_A + \boldsymbol{\tau}_i)) \quad (2.8)$$

Using the Dirac notation and defining $\varphi_{iA} \equiv \varphi(\mathbf{r} - (\mathbf{R}_A - \boldsymbol{\tau}_i))$ we get

$$|\psi_{n,\mathbf{k}}\rangle = \sum_A \sum_i c_{i,n,\mathbf{k}} e^{i\mathbf{k}(\mathbf{R}_A + \boldsymbol{\tau}_i)} |\varphi_{iA}\rangle \quad (2.9)$$

Then the Schröedinger equation becomes

$$\begin{aligned} H |\psi_{\mathbf{k},n}\rangle &= E_n(\mathbf{k}) |\psi_{\mathbf{k},n}\rangle \\ H \sum_A \sum_i c_{i,n} e^{i\mathbf{k}(\mathbf{R}_A + \boldsymbol{\tau}_i)} |\varphi_{iA}\rangle &= E_n(\mathbf{k}) \sum_A \sum_i c_{i,n} e^{i\mathbf{k}(\mathbf{R}_A + \boldsymbol{\tau}_i)} |\varphi_{iA}\rangle \end{aligned} \quad (2.10)$$

Applying $e^{-i\mathbf{k}\boldsymbol{\tau}_j} \langle \varphi_{j0}|$ in the above equation we get

$$\sum_{iA} c_{i,n,\mathbf{k}} e^{i\mathbf{k}(\mathbf{R}_A + \boldsymbol{\tau}_i - \boldsymbol{\tau}_j)} \langle \varphi_{j0} | H | \varphi_{iA} \rangle = E_n(\mathbf{k}) \sum_{iA} c_{i,n,\mathbf{k}} e^{i\mathbf{k}(\mathbf{R}_A + \boldsymbol{\tau}_i - \boldsymbol{\tau}_j)} \langle \varphi_{j0} | \varphi_{iA} \rangle \quad (2.11)$$

On the right side of this equation we have

$$\langle \varphi_j | \varphi_i \rangle = \begin{cases} 1, & \text{if } i = j \text{ and } \mathbf{R}_A = \mathbf{R}_0 \\ s, & \text{if } iA \text{ and } j0 \text{ are first neighbors} \\ 0, & \text{else} \end{cases} \quad (2.12)$$

where $1 > s > 0$ is called the overlap between first neighbors and we do not consider overlap between second neighbors and so on.

On the left side we have

$$\langle \varphi_j | H | \varphi_i \rangle = \begin{cases} E_0, & \text{if } i = j \\ -t_1, & \text{if } iA \text{ and } j0 \text{ are first neighbors} \\ -t_2, & \text{if } iA \text{ and } j0 \text{ are second neighbors} \\ \text{and so on} & \end{cases} \quad (2.13)$$

where E_0 is called the on site energy and t_a is the hopping of order a . In general, hoppings until third order are considered.

In the summations \sum_i , we are summing over all atoms inside a unit cell and counting the interaction between atoms i and j , which are inside the unit cell and the interaction of i with all atoms in other periodic images. The generalized eigenvalue problem can be written in matrix form as

$$H(\mathbf{k}) \begin{bmatrix} c_{n,1} \\ c_{n,2} \\ \vdots \\ c_{n,N} \end{bmatrix} = E(\mathbf{k}) S(\mathbf{k}) \begin{bmatrix} c_{n,1} \\ c_{n,2} \\ \vdots \\ c_{n,N} \end{bmatrix} \quad (2.14)$$

where $H(\mathbf{k})$ ($S(\mathbf{k})$) is a $N \times N$ matrix (N is the total number of atoms in a unit cell), with matrix elements given by

$$H_{ij}(\mathbf{k}) = \begin{cases} E_0, & \text{if } i = j \\ -t_1 e^{i\mathbf{k}(\tau_i - \tau_j)} (\sum_A e^{i\mathbf{k}\mathbf{R}_A}), & \text{if } iA \text{ and } j0 \text{ are first neighbors} \\ -t_2 e^{i\mathbf{k}(\tau_i - \tau_j)} (\sum_A e^{i\mathbf{k}\mathbf{R}_A}), & \text{if } iA \text{ and } j0 \text{ are second neighbors} \\ \text{and so on} & \end{cases} \quad (2.15)$$

and

$$S_{ij}(\mathbf{k}) = \begin{cases} 1, & \text{if } i = j \text{ and } \mathbf{R}_A = \mathbf{R}_0 \\ s e^{i\mathbf{k}(\tau_i - \tau_j)} (\sum_A e^{i\mathbf{k}\mathbf{R}_A}), & \text{if } iA \text{ and } j0 \text{ are first neighbors} \\ 0, & \text{else} \end{cases} \quad (2.16)$$

Once the above problem is solved we obtain a parametric solution $E_n(k)$ that depends on hoppings, on site energies and overlaps. Those parameters are then chosen to reproduce reference data that can be from experiments or other theoretical results. In our work we use as reference DFT and GW bandstructures.

We also calculated the optical absorption at TB level using the Kubo-Greenwood equation for the dynamical conductivity for light polarized along the z direction (the direction parallel to the tube axis) [148]

$$\sigma_{zz}(\omega) = \frac{e^2 \hbar}{iL} \sum_{\mathbf{k}, \alpha, \beta} \frac{f_{FD}(\epsilon_\alpha) - f_{FD}(\epsilon_\beta)}{\epsilon_\alpha - \epsilon_\beta} \frac{|\langle \psi_\alpha | v_z | \psi_\beta \rangle|^2}{\epsilon_\alpha - \epsilon_\beta + \hbar\omega + i\eta} \quad (2.17)$$

where L is the unit cell length, $f_{FD}(\epsilon)$ is the Fermi-Dirac distribution, $|\psi_\alpha\rangle$ is an eigenvector of eq. 2.14, ϵ_α is an eigenvalue of eq. 2.14, $v_z = i/\hbar[H, z]$ is the velocity operator in the z direction (parallel to the tube axis) and η is a phenomenological broadening. The optical absorption is given by the real part of σ_{zz} .

By expanding the eigenvectors $|\psi_\alpha\rangle = \sum_i c_{i,\alpha} |\varphi_i\rangle$ we get

$$\langle \alpha | v_z | \beta \rangle = \sum_{i,j} c_{\alpha,i}^* c_{\beta,j} \langle \varphi_i | v_z | \varphi_j \rangle \quad (2.18)$$

and each element $\langle \varphi_i | v_z | \varphi_j \rangle$ is approximately given by [149]

$$\langle \varphi_i | v_z | \varphi_j \rangle = \frac{i}{\hbar} \langle \varphi_i | H z - z H | \varphi_j \rangle \approx \frac{i}{\hbar} \langle \varphi_i | H | \varphi_j \rangle (z_i - z_j) \quad (2.19)$$

2.1.2 Computational Details

For graphene, we just consider one electron per atom in the p_z orbital, as the bands originated from those orbitals are the closest to the Fermi energy and play an important role in the optical and electronic properties of graphene. For CNTs we also just consider one electron per atom in the p_r orbital, which is analogous to the p_z orbital, but it points in the radial direction.

In Fig. 2.1 we show TB calculations fitted to reproduce DFT data for the graphene dispersion. The more terms are included, the best is the fit and optimized parameters are reported in Table 2.1.

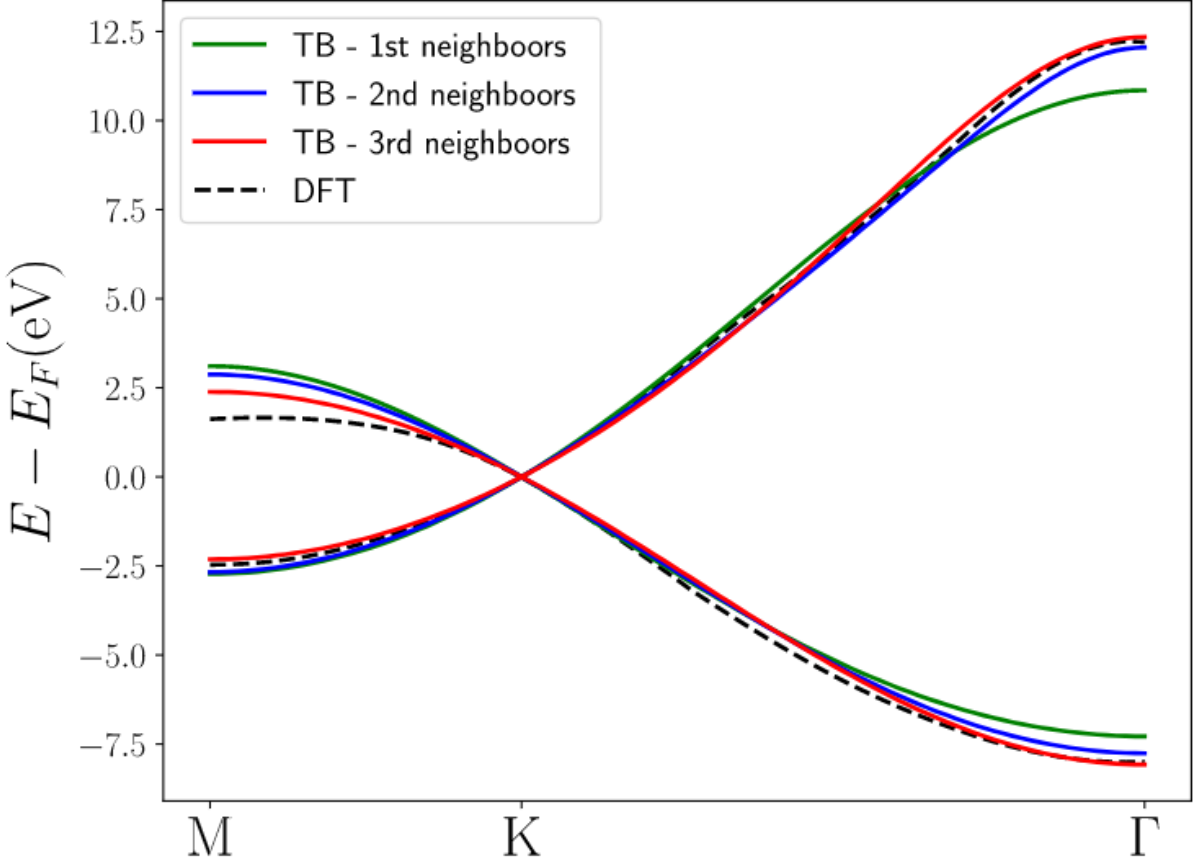


Figure 2.1: TB calculation in graphene with optimized parameters to reproduce DFT data.

To obtain the optimized TB parameters, we used the genetic algorithm [150]. In this optimization method, a set (called population) of vectors (called chromosome) with parameters (called genes) (p_1, p_2, \dots, p_N) are randomly created.

For each vector, an error function is calculated. This error function shows how far a given property of this vector is from a reference property. For example, in the graphene case the error function is given by $\text{Error} = \sum_{k,i} (E_{\text{TB},i}(k) - E_{\text{DFT},i}(k))^2$ where $E_{\text{TB},i}(k)$ ($E_{\text{DFT},i}(k)$) is the TB (DFT) dispersion for the band i and our reference data are DFT calculations. For semiconductor CNTs our error function was defined as $\text{Error} =$

$\sum_{k,i} (E_{\text{TB},i}(k) - E_{\text{GW},i}(k))^2 + 10^3(E_{\text{TB},g} - E_{\text{GW},g})^2$ where $E_{\text{TB},g}$ ($E_{\text{GW},g}$) is the TB (GW) gap. The 10^3 factor was necessary to make the method reproduce the electronic gap. We take as reference values the GW data and our main interest in this calculation is to reproduce the GW gap.

The vectors which show the smallest errors are selected, then in the next step a new population is created where the new chromosomes are created by linear combinations of the previous selected chromosomes (which called parents). This procedure is repeated until convergence is achieved as shown in the Fig. 2.2.

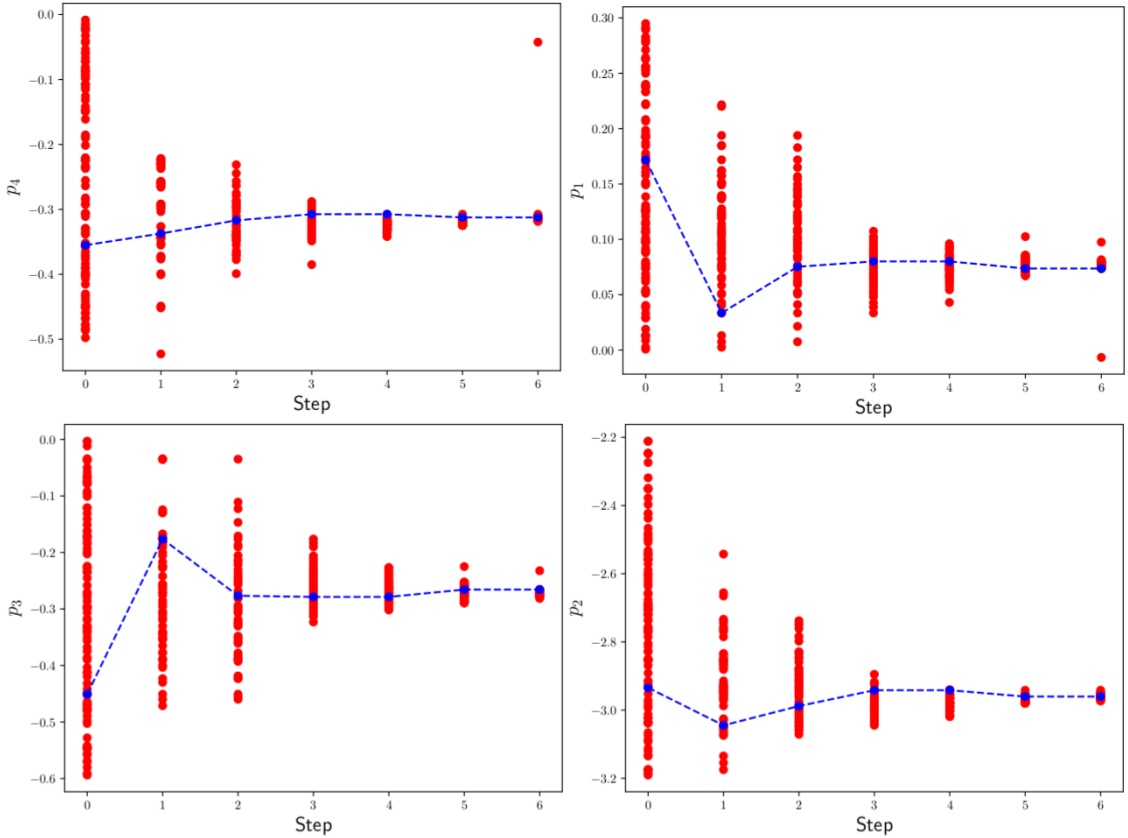


Figure 2.2: Parameters convergence for CNT(11,0). p_1 , p_2 , p_3 and p_4 are the overlap s , first neighbor hopping, second neighbor hopping and third neighbor hopping, respectively. Blue dots are the parameters that shows the best fits in that generation (step).

In the table 2.1 we show our optimized parameters for graphene, CNT(8,0), CNT(10,0) and CNT(11,0) and in Fig. 2.3 we show the band structure for CNTs at TB level for CNTs.

We also performed simpler TB calculations just considering first order neighbors and in this case, as the electronic band gap depends linearly on the hopping parameter [52], the hopping parameter was chosen to reproduce the minimum bandgap.

Both methods show similar performance to reproduce the minimum band gaps and show poor performance to reproduce other energies. For CNTs, when higher order hopping parameters are included the curvature of bands is better reproduced. It is important to note that our hoppings are about 4.6 - 6.0 eV which is higher than usual values 2.7-3.0 eV [12, 151] used in other works because our reference data are GW calculations that usually shows bandgaps higher than DFT calculations.

	s	t_1 (eV)	t_2 (eV)	t_3 (eV)
Graphene - 1st	0.066	2.905	-	-
Graphene - 2nd	0.259	2.268	0.616	-
Graphene - 3rd	0.191	2.596	0.413	0.163
CNT(8,0) - 1st	-	4.814	-	-
CNT(8,0) - 3rd	0.119	5.215	0.228	0.350
CNT(10,0) - 1st	-	4.681	-	-
CNT(10,0) - 3rd	0.132	5.003	0.484	0.330
CNT(11,0) - 1st	-	6.019	-	-
CNT(11,0) - 3rd	0.143	6.393	0.700	0.575

Table 2.1: Tight binding parameters

2.2 Density Functional Theory

2.2.1 Theoretical Background

Density Functional Theory (DFT) [9] is an *ab initio* method which aims transforming the interacting many body problem in a set of noninteracting one particle problems in a effective potential through the Kohn-Sham equations [152]. This effective potential is a functional of the electronic density and then, by the variational principle, one may obtain the ground state for a given collection of electrons in a solid or molecule.

One of the greatest advantages of working with the electronic density instead of the electronic wavefunction is that we are dealing with a function of three coordinates

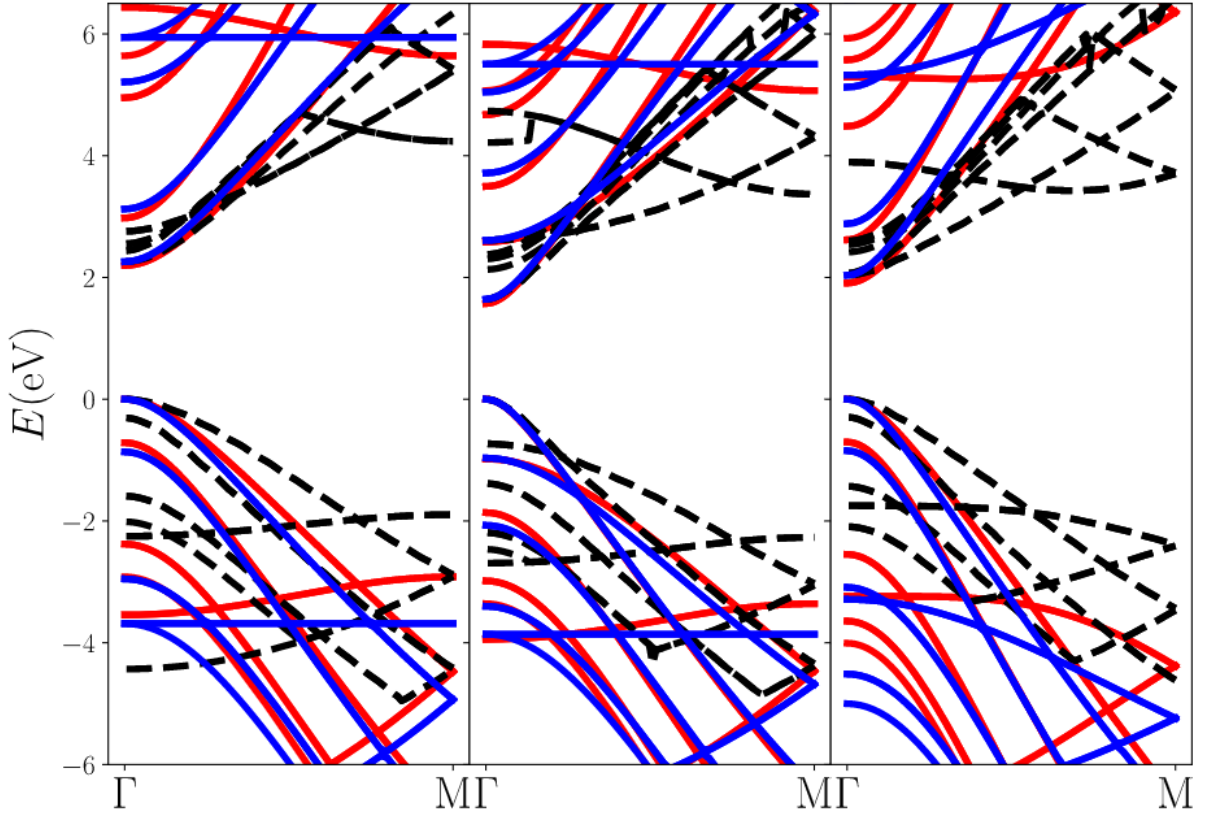


Figure 2.3: Bandsctructure for CNTs (8,0), (10,0) and (11,0). Black dashed lines are GW calculations, red lines are TB calculations including overlap and hopping until third neighbors and blue lines are calculations just including hopping between first neighbors.

$(\rho(x, y, z))$ instead of a many-body wave function that depends on $3N$ coordinates $(\psi(\mathbf{r}_1, \mathbf{r}_2, \dots, \mathbf{r}_N))$, where N is the total number of electrons. Even if it was possible to solve this kind of problem using the N-body wavefunction, the analysis and storage of information would be a great computational challenge as explained in the Walter Kohn's Nobel lecture [153], "In general the many-electron wave function $\psi(\mathbf{r}_1, \mathbf{r}_2, \dots, \mathbf{r}_N)$ for a system of N electrons is not a legitimate scientific concept, when $N > N_0 \approx 10^3$ ".

For DFT we work with the hamiltonian in the following form

$$H = H_{ele} + V_{ext}(\mathbf{r}) \quad (2.20)$$

where H_{ele} is the same in eq. (2.2) and $V_{ext}(\mathbf{r})$ includes the electron-ion interaction and other external potentials, as for example an electrostatic potential.

The DFT method is based on the Hohenberg-Kohn theorems [154]. The first theorem is:

Theorem 1. *For any system of interacting particles in an external potential $V_{ext}(\mathbf{r})$, the potential $V_{ext}(\mathbf{r})$ is determined uniquely, except for a constant, by the ground state particle density $n_0(\mathbf{r})$*

Proof. Suppose that for a given external potential V_{ext} the ground state is $|\psi\rangle$ and for another external potential V'_{ext} the ground state is $|\psi'\rangle$. Our assumption is that both V_{ext} and V'_{ext} give the same electronic density $n_0(\mathbf{r})$. By the variational principle, the ground state energies E and E' for each potential satisfy

$$E = \langle\psi|H_{el} + V_{ext}|\psi\rangle < \langle\psi'|H_{el} + V_{ext}|\psi'\rangle; \quad (2.21)$$

$$E' = \langle\psi'|H_{el} + V'_{ext}|\psi'\rangle < \langle\psi|H_{el} + V'_{ext}|\psi\rangle; \quad (2.22)$$

Adding and subtracting $\langle\psi'|V'_{ext}|\psi'\rangle$ in the inequality 2.21 we get:

$$\begin{aligned} E &< \langle\psi'|H_{el} + V_{ext} + V'_{ext} - V'_{ext}|\psi'\rangle \\ E &< \langle\psi'|H_{el} + V'_{ext}|\psi'\rangle + \langle\psi'|V_{ext} - V'_{ext}|\psi'\rangle \\ E &< E' + \int d^3r (V_{ext} - V'_{ext}) n_0(\vec{r}); \end{aligned} \quad (2.23)$$

where in the second step we have used 2.22. Repeating the procedure for E' in 2.22 we get

$$E' < E + \int d^3r (V'_{ext} - V_{ext}) n_0(\mathbf{r}); \quad (2.24)$$

summing 2.23 and 2.24 we have

$$E + E' < E' + E, \quad (2.25)$$

which is absurd. Since we have assumed the same density $n_0(\mathbf{r})$ for $V_{ext} \neq V'_{ext}$, we conclude that this assumption is incorrect, thus proving the theorem.

□

The second theorem is:

Theorem 2. *A universal functional for the energy $E[n]$ in terms of the density $n(\vec{r})$ can be defined, valid for any external potential $V_{ext}(\vec{r})$. For any particular $V_{ext}(\mathbf{r})$, the exact ground state energy of the system is the global minimum value of this functional, and the density $n(\mathbf{r})$ that minimizes that functional is the exact ground state density $n_0(\mathbf{r})$*

Proof. We can write the total energy as a functional of the density

$$E[n] = \langle \psi | H_{ele} + V_{ext} | \psi \rangle = F[n] + \langle \psi | V_{ext} | \psi \rangle; \quad (2.26)$$

where $F[n]$ is an unknown universal functional and $\langle \psi | V_{ext} | \psi \rangle$ depends on the system. In particular for the ground state

$$E[n_0] = \langle \psi_0 | H_{ele} + V_{ext} | \psi_0 \rangle = F[n_0] + \langle \psi_0 | V_{ext} | \psi_0 \rangle; \quad (2.27)$$

Using the variational principle and assuming $n \neq n_0$

$$\begin{aligned} E[\psi_0] &< E[\psi] \\ \langle \psi_0 | H_{ele} + V_{ext} | \psi_0 \rangle &< \langle \psi | H_{ele} + V_{ext} | \psi \rangle \\ F[n_0] + \langle \psi_0 | V_{ext} | \psi_0 \rangle &< F[n] + \langle \psi | V_{ext} | \psi \rangle \\ E[n_0] &< E[n]; \end{aligned} \quad (2.28)$$

In conclusion, there is a variational principle valid to the electronic density as there is one for the wave-function.

□

Therefore, the first theorem states a one to one relation between the external potential $V_{ext}(\mathbf{r})$ and the particle density and the second one states that for this potential there is a functional $E[n]$ for which the global minimum is given by $n_0(\mathbf{r})$.

The Hohenberg-Kohn theorems describe an exact many-body theory expressing the energy of the system as a functional of the electronic density. However, it does not tell us anything about how this electronic density functional is constructed or how to solve the problem. For this, the Kohn-Sham ansatz [152] is needed.

Following the Hartree-Fock approach, the Kohn-Sham ansatz [152] aims to reduce the interacting N -body problem to N one body problems in the presence of an effective potential that depends on the particle density. It assumes that the exact ground state density can be represented by the density of an auxiliary system of non-interacting particles and the auxiliary hamiltonian is chosen to have the usual kinetic energy operator and an effective local potential. The density of the non-interacting system is

$$n(\vec{r}) = \sum_i |\psi_i(\vec{r})|^2; \quad (2.29)$$

where ψ_i are single-particle states. The auxiliary hamiltonian

$$H_{aux} = -\frac{\hbar^2}{2m_e} \nabla^2 + V_{eff}(\vec{r}); \quad (2.30)$$

The independent-particle kinetic energy is given by

$$T_s = -\frac{\hbar^2}{2m_e} \sum_i \langle \psi_i | \nabla^2 | \psi_i \rangle; \quad (2.31)$$

The classical electronic coulomb interaction is given by the Hartree term

$$H_{Hartree}[n] = \frac{1}{2} \frac{e^2}{4\pi\epsilon_0} \int d^3r d^3r' \frac{n(\vec{r})n(\vec{r}')}{|\vec{r} - \vec{r}'|}; \quad (2.32)$$

The Kohn-Sham approach is to rewrite the Hohenberg-Kohn expression 2.26 as

$$E_{KS} = T_s[n] + H_{Hartree}[n] + \int d^3r V_{ext}(\vec{r}) n(\vec{r}) + E_{xc}[n]; \quad (2.33)$$

where the new term E_{xc} , the exchange-correlation energy, includes all the exchange and the so-called correlation effects. Comparing 2.26 and 2.33 we can see that

$$E_{xc}[n] = F[n] - (T_s[n] + E_{Hartree}[n]); \quad (2.34)$$

or more explicitly with $\langle T \rangle$ and $\langle V_{int} \rangle$ being the mean kinetic energy and mean internal energy respectively

$$E_{xc}[n] = \langle T \rangle - T_s[n] + \langle V_{int} \rangle - E_{Hartree}[n]; \quad (2.35)$$

The last equation shows that E_{xc} is just the difference of the kinetic and internal energies of the true many-body system from those auxiliary independent-particle system. If the exact E_{xc} were known, then the exact ground state energy and density of the many-body problem could be found by minimizing the functional 2.33 with the constraint $\int d^3r n(\vec{r}) = N$.

Now we should minimize 2.33 with respect to the electronic density. Since T_s is a functional of the single-electron orbitals, which are functionals of density themselves, and all the other terms are functionals of density explicitly, we can minimize the total energy functional E_{KS} with respect to any given orbital ψ_i^* and use the chain rule for $n(\vec{r})$.

$$\frac{\delta E_{KS}}{\delta \psi_i^*(\vec{r})} = \frac{\delta T_s}{\delta \psi_i^*(\vec{r})} + \left[\frac{\delta E_{ext}}{\delta n(\vec{r})} + \frac{\delta E_{Hartree}}{\delta n(\vec{r})} + \frac{\delta E_{xc}}{\delta n(\vec{r})} \right] \frac{\delta n(\vec{r})}{\delta \psi_i^*(\vec{r})} = 0; \quad (2.36)$$

with the orthonormalization condition

$$\langle \psi_i | \psi_j \rangle = \delta_{i,j}. \quad (2.37)$$

From 2.31:

$$\frac{\delta T_s}{\delta \psi_i^*(\vec{r})} = -\frac{\hbar^2}{2m_e} \nabla^2 \psi_i; \quad (2.38)$$

and from 2.29:

$$\frac{\delta n(\vec{r})}{\delta \psi_i^*} = \psi_i. \quad (2.39)$$

By using the Lagrange multiplier method, we get the Kohn-Sham equations

$$(H_{KS} - \varepsilon_i) \psi_i = 0, \quad (2.40)$$

where ε_i are the eigenvalues and H_{KS} is the effective hamiltonian, given by

$$H_{KS} = -\frac{\hbar^2}{2m_e} \nabla^2 + V_{KS}, \quad (2.41)$$

in which the Kohn-Sham potential is given by

$$V_{KS} = V_{ext} + \frac{\delta E_{Hartree}}{\delta n(\vec{r})} + \frac{\delta E_{xc}}{\delta n(\vec{r})}; \quad (2.42)$$

To solve the KS equations, it is necessary to know the ground state electronic density to construct the functionals in eq. (2.33), which means that the KS potential depends on its solution. To overcome this problem, the KS equations are solved self-consistently: an initial guess for $n(\vec{r})$ is necessary (usually a linear combination of atomic orbitals), construct the KS potential, solve the KS equations and then a new density is calculated from those solutions $\{\psi_i\}$ and then this process is repeated until convergence is achieved, as shown in the diagram of Fig. 2.4. Such a sequence is called a Self Consistent Field (SCF) calculation

2.2.2 Computational details

We studied (n, 0) CNTs (n=8, 10 and 11) with and without hydrogen atoms. For pristine CNTs the unit cell length is 4.2Å with 4n carbon atoms. For CNTs with H, the unit

Self-Consistent Kohn-Sham Equations

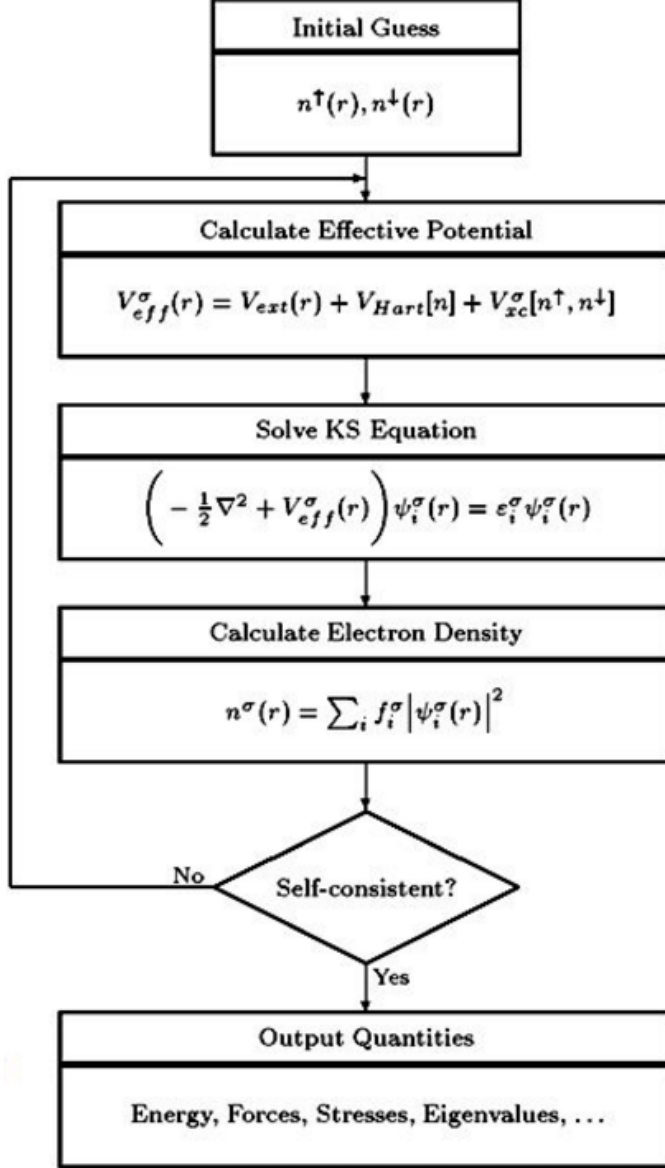


Figure 2.4: Schematic algorithm to solve self-consistently the Kohn-Sham equations. The σ index indicates the spin degree of freedom, which is not discussed in this work. Figure reproduced from ref. [9]

cell was replicated 4, 6, 8 and 10 times for (10, 0) CNT and just 4 times for (8,0) and (11,0) tubes, so in our supercells the CNT length is about $4.2 \times N_{cells} \text{\AA}$ and there are $4nN_{cells}$ carbon atoms. One hydrogen atom was placed over a carbon atom and then this structure was relaxed allowing the supercell size to change in the direction parallel to the tube axis. For each case the ratio between hydrogen atoms to carbon atoms is 1 : $4nN_{cells}$

and the defect concentration is $1/0.42N_{cells}$ defects per nanometer. The lattice constants perpendicular to the tube axis were chosen to make the distance of the tube and its periodic images at least 12 Å as shown in Fig. 2.5.

DFT calculations were done using a normconserving pseudopotential (C.pz-vbc.UPF) with a cutoff of 60 Ry for scf calculation and a gaussian smearing of 1 mRy using the Quantum Espresso package [146, 147]. K point grids were one dimensional and had $24/N_{cells}$ points. Due to zone folding, supercells with bigger lengths need less k points sampling.

We also studied the (6,5) CNT, for which the cell length is about 40 Å, with 364 carbon atoms. Its length is close to the length of the case where we replicated 10 unit cells of the (n, 0) tube ($\approx 42\text{\AA}$), so we used 3 k points for its grid sampling.

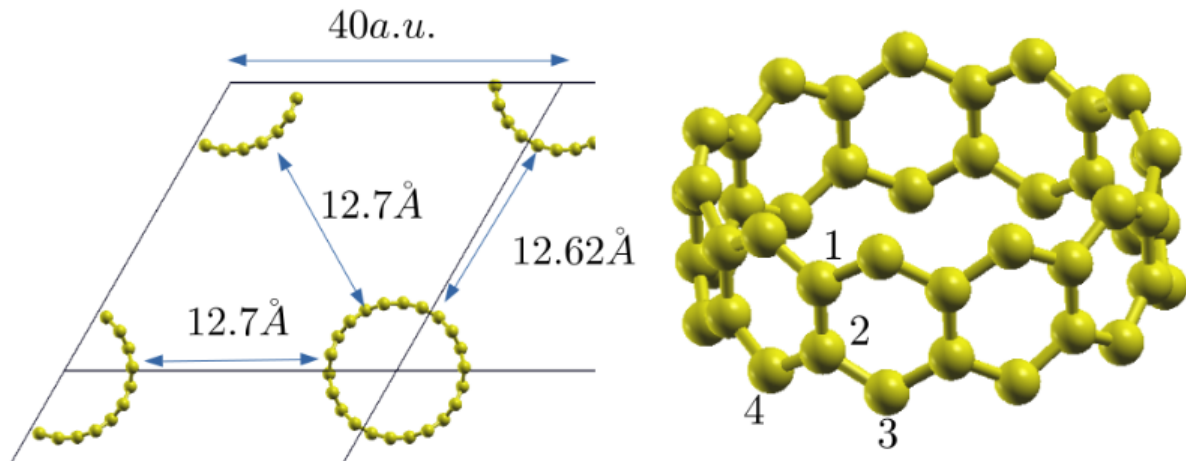


Figure 2.5: Supercell size

2.3 Many Body Perturbation Theory

As explained in the above section, DFT is an exact theory and depends on the quality of the chosen exchange correlation potential. Extensive benchmarks studies show that recent E_{xc} functionals [155–158] have good performance to reproduce several solid properties such as lattice constants, cohesive energies and etc, justifying its large use by the scientific community [159].

Despite that, it is known that DFT underestimates electronic bandgaps of semiconductors [160, 161] as the bandgap itself is an excited state property and DFT is a ground state theory, even if one uses the exact correlation exchange functional, it still will underestimate the electronic gap.

On the top of our DFT results, we performed GW calculations to include many body and dynamical effects and then we solved the Bethe-Salpeter equation (BSE) to obtain the excitonic wavefunctions and the absorption spectra. In the following section the theoretical frameworks is presented and in the end we show our convergence studies and the parameters used in our calculations.

The electronic problem is given by the following hamiltonian in the second quantization

$$H = \int d\mathbf{x} \psi^\dagger(\mathbf{x}) h(\mathbf{x}) \psi(\mathbf{x}) + \int d\mathbf{x} d\mathbf{x}' \psi^\dagger(\mathbf{x}) \psi^\dagger(\mathbf{x}') v(\mathbf{r}, \mathbf{r}') \psi(\mathbf{x}') \psi(\mathbf{x}) + E_{ion-ion} \quad (2.43)$$

where $h(\mathbf{x})$ is the one body hamiltonian, $v(\mathbf{r}, \mathbf{r}')$ is the coulomb potential, $\psi(\mathbf{x}) = \sum_k a_k \phi_k(\mathbf{x})$ ($\psi(\mathbf{x}) = \sum_k a_k^\dagger \phi_k(\mathbf{x})$) is the field operator, a_k (a_k^\dagger) is the annihilation (creation) operator and $\mathbf{x} = (\mathbf{r}, \sigma)$ includes both position and spin.

The one body Green function is given by [10, 160, 162–170]

$$G(\mathbf{x}, t, \mathbf{x}', t') = -i \langle N | T[\psi_H(\mathbf{x}, t) \psi_H^\dagger(\mathbf{x}', t')] | N \rangle \quad (2.44)$$

where $\psi_H(\mathbf{x}, t) = \sum_k a_k \phi(\mathbf{x}, t)$ is the field operator in the Heisenberg picture, T is the time ordering operator and $|N\rangle$ is the fundamental state with N particles. For $t > t'$ it is the probability that a hole created in (\mathbf{x}, t) will propagate to (\mathbf{x}', t') and for $t < t'$ it is the probability that an electron created (\mathbf{x}', t') will propagate to (\mathbf{x}, t) .

Using the completeness relation $I = \sum_s |N \pm 1\rangle \langle N \pm 1|$ and going to the energy domain the (Lehmann) spectral representation is given by

$$G(\mathbf{x}, \mathbf{x}', \epsilon) = \sum_s \left[\frac{f_s(\mathbf{x}) f_s^*(\mathbf{x}')}{\epsilon - \epsilon_s - \mu + i\delta} + \frac{f_s(\mathbf{x}) f_s^*(\mathbf{x}')}{\epsilon + \epsilon_s - \mu - i\delta} \right] \quad (2.45)$$

where $f_s(\mathbf{x}) = \langle N|\psi(\mathbf{x})|N+1, s\rangle$.

The Heisenberg equation of motion for the field operator is given by

$$i\frac{\partial\psi(\mathbf{x})}{\partial t} = [\psi(\mathbf{x}), H] \quad (2.46)$$

then we obtain the following equation for G (for detailed steps see references [160, 163])

$$[\epsilon_s - h(\mathbf{x}) - V_H(\mathbf{r})]G(\mathbf{x}, \mathbf{x}', \epsilon) - \int d\mathbf{x}'' \Sigma(\mathbf{x}, \mathbf{x}'', \epsilon)G(\mathbf{x}'', \mathbf{x}', \epsilon) = \delta(\mathbf{x} - \mathbf{x}') \quad (2.47)$$

where $V_H(\mathbf{r})$ is the Hartree potential and $\Sigma(\mathbf{x}, \mathbf{x}'', \epsilon)$ is the self-energy. If we set $\Sigma = 0$ in the above equation, the corresponding Green function would be G_0

$$[\epsilon_s - h(\mathbf{x}) - V_H(\mathbf{r})]G_0(\mathbf{x}, \mathbf{x}', \epsilon) = \delta(\mathbf{x} - \mathbf{x}') \quad (2.48)$$

and G and G_0 are related by the Dyson equation

$$G = G_0 + G_0\Sigma G \quad (2.49)$$

Introducing the notation $G(\mathbf{x}, \mathbf{x}') = G(1, 2)$, where $1 \equiv (\mathbf{x}_1, t_1)$, $G_0(1, 2)$ is the direct propagation from 1 to 2 without exchange-correlation effects, then Σ contains those interactions in the propagation from 1 to 2.

The self-energy Σ obeys the following set of coupled equations, known as Hedin's equations,

$$\begin{aligned} \Sigma(1, 2) &= i \int G(1, 4)W(1^+, 3)\Gamma(4, 2; 3)d(3, 4) \\ W(1, 2) &= v(1, 2) + \int W(1, 3)P(3, 4)v(4, 2)d(3, 4) \\ P(1, 2) &= -i \int G(2, 3)G(4, 2)\Gamma(3, 4; 1)d(3, 4) \\ \Gamma(1, 2; 3) &= \delta(1, 2)\delta(1, 3) + \int \frac{\delta\Sigma(1, 2)}{\delta G(4, 5)}G(4, 6)G(7, 5)\Gamma(6, 7; 3)d(4, 5, 6, 7) \end{aligned} \quad (2.50)$$

where W is the screened Coulomb potential, P is polarizability and Γ the vertex function.

2.3.1 GW approximation

In the GW approximation, the vertex is approximated by $\Gamma(1, 2; 3) = \delta(1, 2)\delta(1, 3)$, then Hedin's equations become [162, 171]

$$\begin{aligned}\Sigma(1, 2) &= iG(1, 2)W(1^+, 2) \\ W(1, 2) &= v(1, 2) + \int W(1, 3)P(3, 4)v(4, 2)d(3, 4) \\ P(1, 2) &= -iG(1, 2)G(2, 1) \\ \Gamma(1, 2; 3) &= \delta(1, 2)\delta(1, 3)\end{aligned}\tag{2.51}$$

The approximation is called GW approximation because the self energy is given by iGW . The Hedin equations can be solved selfconsistently but in general just one step is made to evaluate the self energy, which is called G_0W_0 .

In our work we used the BerkeleyGW code [171–173] to calculate the self energy. Next we discuss how is this calculation is done. First it is necessary to perform DFT (or other mean field method) calculations, and from that we have a set of eigenvectors $|n\mathbf{k}\rangle$ and eigenvalues $E_{n\mathbf{k}}$. In the code workflow, then the dielectric matrix is constructed.

The static polarizability matrix element is given by

$$\chi_{\mathbf{GG}'}(\mathbf{q}; 0) = \sum_n^{\text{occ}} \sum_{n'}^{\text{emp}} \sum_{\mathbf{k}} \frac{M_{nn'}(\mathbf{k}, \mathbf{q}, \mathbf{G}) M_{nn'}^*(\mathbf{k}, \mathbf{q}, \mathbf{G}')}{E_{n\mathbf{k}+\mathbf{q}} - E_{n'\mathbf{k}}}\tag{2.52}$$

where

$$M_{nn'}(\mathbf{k}, \mathbf{q}, \mathbf{G}) = \langle n\mathbf{k} + \mathbf{q} | e^{i(\mathbf{q} + \mathbf{G}) \cdot \mathbf{r}} | n'\mathbf{k} \rangle,\tag{2.53}$$

$\langle n\mathbf{k} |$ and $E_{n\mathbf{k}}$ are the Bloch eigenvectors and Bloch eigenenergies calculated at DFT level, respectively. Sums are performed over occupied and unoccupied states and a $\mathbf{G} \times \mathbf{G}$ matrix is built, where \mathbf{G} and \mathbf{G}' are the reciprocal lattice vectors. The convergence parameters are: the number of empty bands included in the summation, the grid density of \mathbf{k} points

and the amount of \mathbf{G} vectors in the polarizability matrix, given by a cutoff energy where $\hbar^2|G|^2/2m_e < E_{cut}$.

In Fig. 2.6 we show the convergence of two different matrix elements $\chi_{00}(\mathbf{q})$ and $\chi_{\mathbf{G}_m \mathbf{G}_m}(\mathbf{q})$ (\mathbf{G}_m is the highest \mathbf{G} vector) as a function of empty conduction bands included in summation of equation (2.52) for different energy cutoffs to construct the χ matrix. This calculation was done for pristine CNT(11,0) and $\mathbf{q} = 0.001(2\pi/L)$ ($2\pi/L$ is the first Brillouin Zone length).

The dielectric matrix is given by

$$\epsilon_{\mathbf{GG}'}(\mathbf{q}; 0) = \delta_{\mathbf{GG}'} - v(\mathbf{q} + \mathbf{G})\chi_{\mathbf{GG}'}(\mathbf{q}; 0) \quad (2.54)$$

where $v(\mathbf{q}) = 4\pi/e|\mathbf{q}|^2$ is the bare Coulomb potential (unescreened) evaluated in the reciprocal space.

For low dimensional systems, special attention must be given to the k point sampling of the dielectric function. For 3D systems the screening is almost uniform, although for 1D and 2D systems the dielectric function varies very quickly in real space. Particularly for 1D and 2D systems, the dielectric function in the reciprocal (real) space goes to unity at both small and large q (large and small distances) [68]. In Fig. 2.7 we show how the k point sampling is important to capture quick variations of ϵ_{00}^{-1} when $q \rightarrow 0$.

The screened potential is given by

$$W_{\mathbf{GG}'}(\mathbf{q}; 0) = \epsilon_{\mathbf{GG}'}^{-1}(\mathbf{q}; 0)v(\mathbf{q} + \mathbf{G}') \quad (2.55)$$

The quasi particle energies are given by

$$E_{nk}^{QP} = E_{nk}^{MF} + \langle \psi_{nk} | \Sigma(E) - \Sigma^{MF}(E) | \psi_{nk} \rangle \quad (2.56)$$

where $\Sigma^{MF}(E)$ is the mean field selfenergy given by $\Sigma^{MF}(E) = V_{xc}$, the exchange correlation potential in DFT calculations.

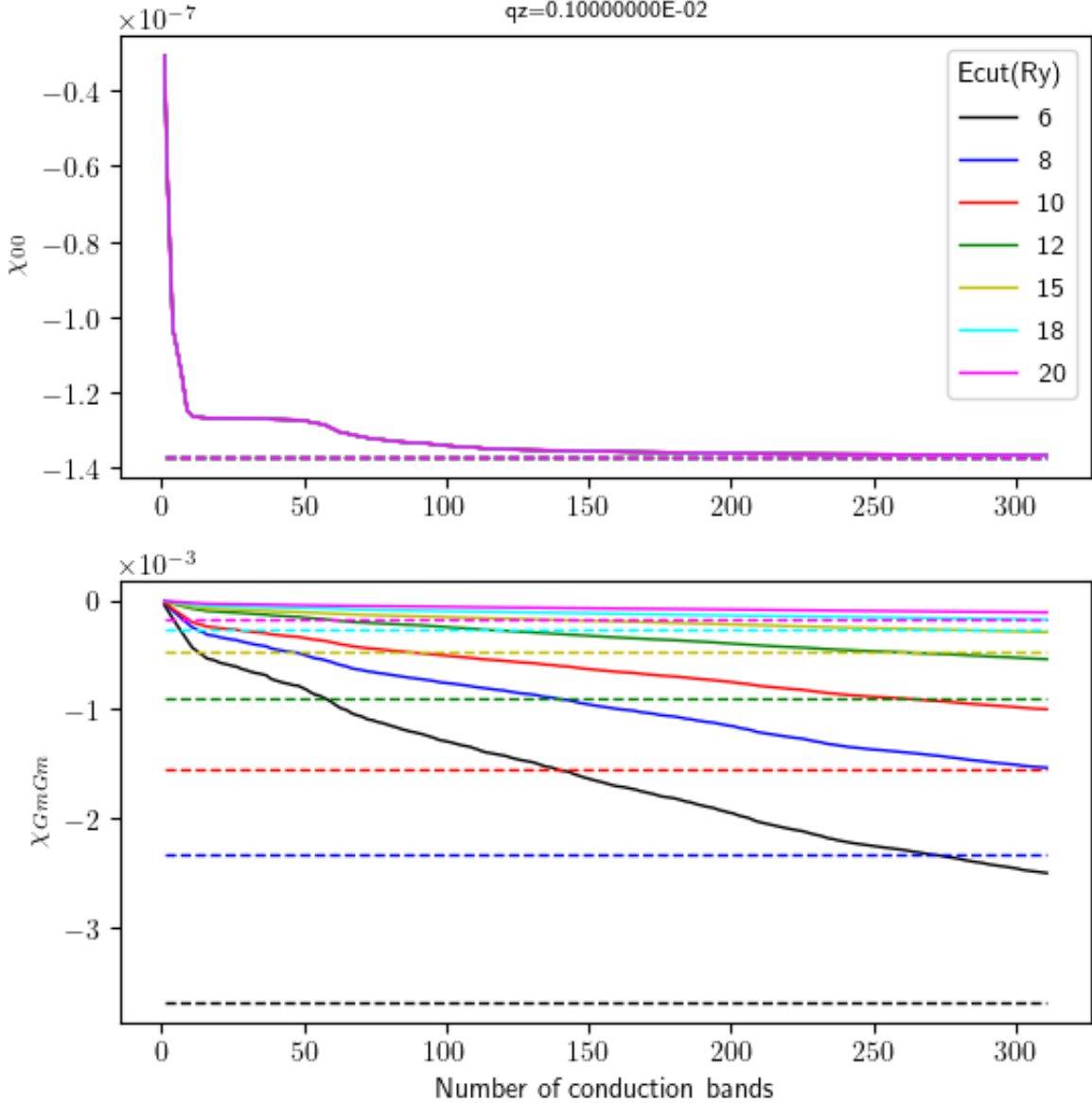


Figure 2.6: Convergence of χ_{00} and χ_{GmGm} as a function of the energy cutoff for the construction of χ matrix. \mathbf{G}_m is the last vector used in the matrix evaluation. That is why χ_{GmGm} is not well converged as χ_{00} . In those calculations we used 12 k points in our grid.

Until now, we worked in the static cases, where $\omega = 0$. To include dynamical effects, we use the Generalized Plasmon Pole (GPP) method [171, 173]. The selfenergy is given by $\Sigma = \Sigma_{SX} + \Sigma_{CH}$, where Σ_{SX} is the screened exchange interaction and Σ_{CH} is the Coulomb hole term, which describes the charge reorganization due to screening. Those

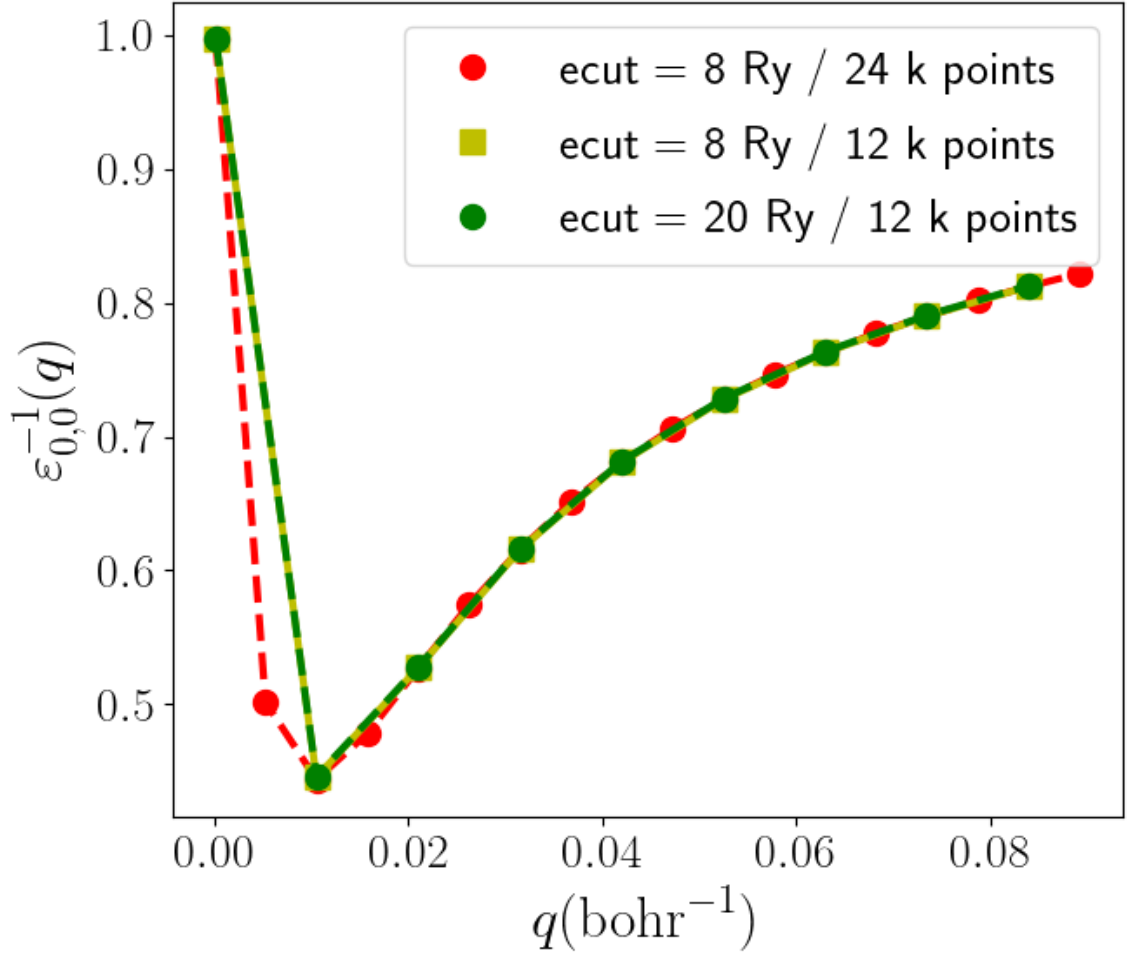


Figure 2.7: ε_{00}^{-1} for CNT(11,0) with different k point samplings. In those calculations we used 400 empty conduction bands in the summations.

terms are given by

$$\langle n\mathbf{k} | \Sigma_{SX}(E) | n'\mathbf{k}' \rangle = - \sum_{n''}^{occ} \sum_{\mathbf{q}\mathbf{G}\mathbf{G}'} M_{n''n}^*(\mathbf{k}, -\mathbf{q}, -\mathbf{G}) M_{n''n'}(\mathbf{k}, -\mathbf{q}, -\mathbf{G}') \times \left[\delta_{\mathbf{G}\mathbf{G}'} + \frac{\Omega_{\mathbf{G}\mathbf{G}'}^2(\mathbf{q})}{(E - E_{n''\mathbf{k}-\mathbf{q}})^2 - \tilde{\omega}_{\mathbf{G}\mathbf{G}'}^2} \right] \quad (2.57)$$

and

$$\begin{aligned} \langle n\mathbf{k} | \Sigma_{CH}(E) | n'\mathbf{k}' \rangle = & -\frac{1}{2} \sum_{n''} \sum_{qGG'} M_{n''n}^*(\mathbf{k}, -\mathbf{q}, -\mathbf{G}) M_{n''n'}(\mathbf{k}, -\mathbf{q}, -\mathbf{G}'') \\ & \times \frac{\Omega_{GG'}^2(\mathbf{q})}{\tilde{\omega}_{GG'}(\mathbf{q}) [E - E_{n''\mathbf{k}-\mathbf{q}} - \tilde{\omega}_{GG'}(\mathbf{q})]} v(\mathbf{q} + \mathbf{G}'') \end{aligned} \quad (2.58)$$

where the auxiliary quantities are given by

$$\Omega_{GG'}^2(\mathbf{q}) = \omega_P^2 \frac{(\mathbf{q} + \mathbf{G}) \cdot (\mathbf{q} + \mathbf{G}')}{|\mathbf{q} + \mathbf{G}|^2} \frac{\rho(\mathbf{G} - \mathbf{G}')}{\rho(0)} \quad (2.59)$$

$$\tilde{\omega}_{GG'}^2(\mathbf{q}) = \frac{\Omega_{GG'}^2(\mathbf{q})}{\delta_{GG'} - \epsilon_{GG'}^{-1}(\mathbf{q}; 0)}, \quad (2.60)$$

$\rho(\mathbf{q})$ is the charge density in the reciprocal space and $\omega_P^2 = 4\pi\rho(0)e^2/m$ is the plasma frequency.

In Fig. 2.8 we show that GW has a better performance than DFT in reproducing experimental values of gaps of semiconductor materials. DFT results always underestimates the bandgap and we also observe this in our results for CNTs (see Fig. 3.1).

In our convergence studies for pristine CNT(11,0) we see that the bandgap depends on the number of empty conduction bands included in summations and the number of k points as shown in Figs 2.9 and 2.10. Those parameters must be converged very carefully as pointed out in ref. [174].

2.3.2 Bethe-Salpeter Equation

The Bethe-Salpeter Equation (BSE) describes the motion of the two particle Green function [163, 166, 172].

The Bethe-Salpeter equation is given by

$$L(12; 1'2') = L_0(12; 1'2') + \int d(3456)L_0(14; 1'3)K(35; 46)L(62; 52) \quad (2.61)$$

where $L(12; 1'2')$ is the electron-hole correlation function given by

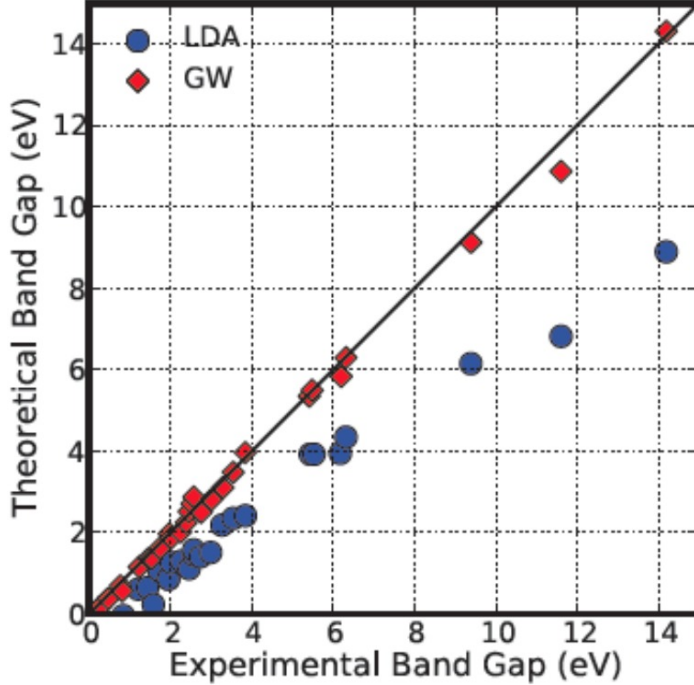


Figure 2.8: Theoretical band gap calculated at DFT (using LDA exchange correlation functional) and GW level versus experimental bandgap for several semiconductors. The perfect agreement is on the diagonal line. Data from [10]

$$L(12; 1'2') = -G_2(12; 1'2') + G_1(11')G_1(22') \quad (2.62)$$

and G_2 (G_1) is the two-body (one body) Green's function. K is the two-particle interaction kernel and that in the GW approximation is given by

$$\begin{aligned} K(34'; 3'4) &= \frac{\delta[V_H(3)\delta(3, 3') + \Sigma(3, 3')]}{\delta G(4, 4')} \\ &= -i\delta(3, 3')\delta(4^+, 4')v(3, 4) + i\delta(3, 4)\delta(3', 4')W(3^+, 3') \end{aligned} \quad (2.63)$$

The first (second) term in eq. (2.63) is the called direct (exchange) term that depends on the bare (screened) Coulomb potential.

In the case of $t_1, t'_1 > t_2, t'_2$ (the temporal coordinates in $L(12; 1'2')$) the exciton wavefunction is given by

$$|N, S\rangle = \sum_{v, \text{holes}} \sum_{c, \text{el}} A_{cv}^S a_v^\dagger b_c^\dagger |N, 0\rangle = \sum_{v, \text{holes}} \sum_{c, \text{el}} A_{cv}^S \psi_c(\mathbf{r}_e) \psi_v(\mathbf{r}_h) \quad (2.64)$$

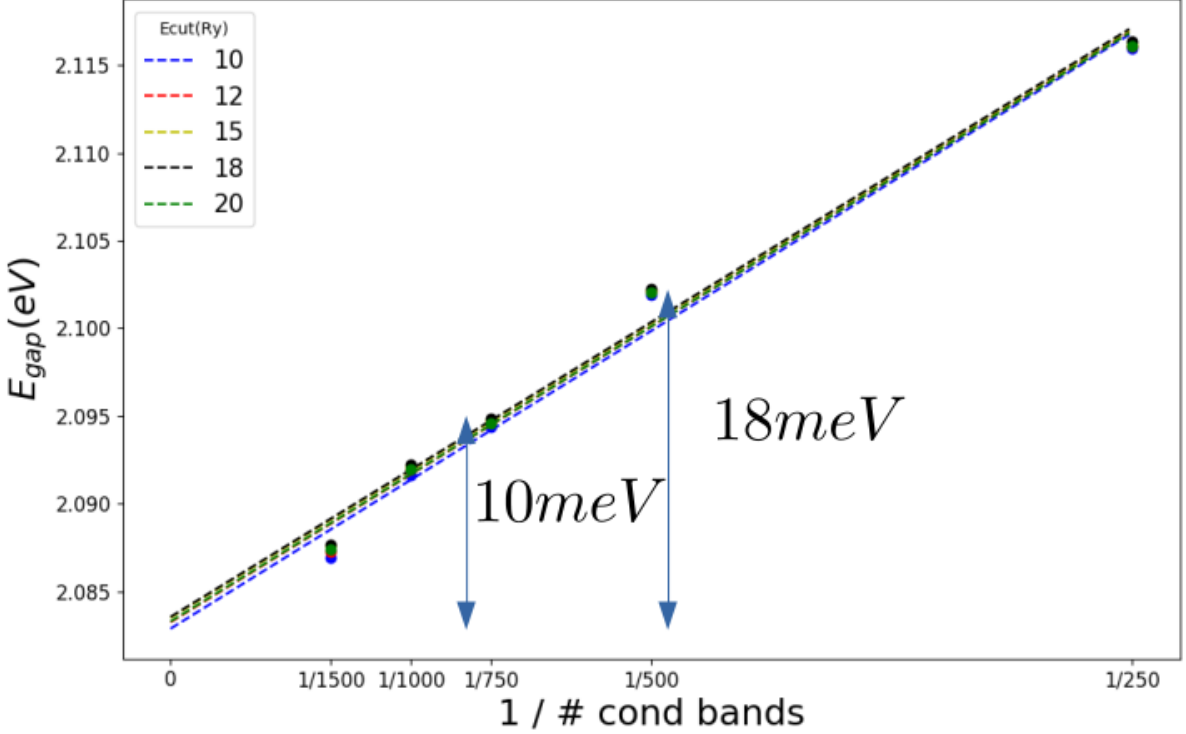


Figure 2.9: GW gap as a function of the number of conduction bands for different cutoff energies in epsilon. In those calculations 12 k points were used in grids.

where a_v^\dagger (b_c^\dagger) creates a hole (electron) in the valence (conduction) band, A_{cv}^S are coefficients to be determined and \mathbf{r}_e (\mathbf{r}_h) is the electron (hole) position vector.

The BSE becomes

$$(E_c - E_v)A_{cv}^S + \sum_{cv,c'v'} K_{cv,c'v'}(\Omega_S)A_{cv}^S = \Omega_S A_{cv}^S \quad (2.65)$$

and the kernel $K = K_d + K_X$, is given by

$$\langle vc|K_d|v'c'\rangle = \int d\mathbf{r} d\mathbf{r}' \psi_c^*(\mathbf{r}) \psi_{c'}(\mathbf{r}) W(\mathbf{r}, \mathbf{r}') \psi_{v'}^*(\mathbf{r}') \psi_v(\mathbf{r}') \quad (2.66)$$

and

$$\langle vc|K_X|v'c'\rangle = \int d\mathbf{r} d\mathbf{r}' \psi_c^*(\mathbf{r}) \psi_v(\mathbf{r}) v(\mathbf{r}, \mathbf{r}') \psi_{v'}^*(\mathbf{r}') \psi_{c'}(\mathbf{r}') \quad (2.67)$$

and in equation (2.65) Ω_S is the necessary energy to create an exciton. In the above

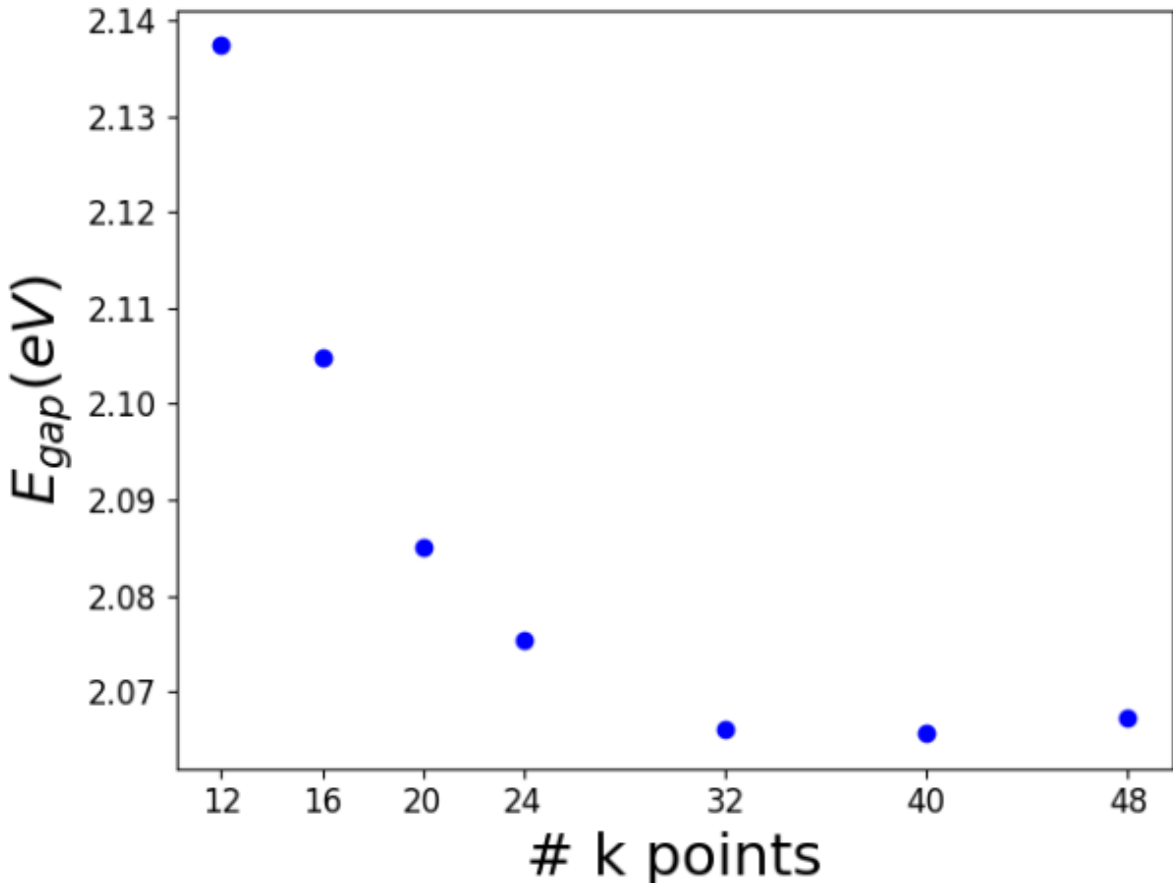


Figure 2.10: GW gap as function of the number of k points included in calculations. In those calculations 300 empty conduction bands were included and a cutoff of 10 Ry was used to construct the dielectric matrix.

equations summations in k are implicit for excitons with center of mass momentum equal to zero, then $k_c = k_v$, where k_c (k_v) is the crystal momentum for the conduction (valence) band.

The optical absorption is obtained from the imaginary part of the macroscopic dielectric constant, which is given by

$$\varepsilon_2(\omega) = \frac{16\pi^2 e^2}{\omega^2} \sum_s |\langle N, 0 | \hat{\mathbf{e}} \cdot \mathbf{v} | N, S \rangle|^2 \delta(\Omega_S - \hbar\omega) \quad (2.68)$$

where $\hat{\mathbf{e}}$ is the direction of the incident radiation polarization and

$$\langle N, 0 | \hat{e} \cdot \mathbf{v} | N, S \rangle = \sum_{cv} A_{cv}^S \langle c | \hat{e} \cdot \mathbf{v} | v \rangle \quad (2.69)$$

For systems where the excitonic effects can be neglected the optical absorption is given by

$$\varepsilon_2(\omega) = \frac{16\pi^2 e^2}{\omega^2} \sum_{c,v} |\langle c | \hat{e} \cdot \mathbf{v} | v \rangle|^2 \delta(E_c - E_v - \hbar\omega) \quad (2.70)$$

where $E_{c(v)}$ can be the quasi particle energies or mean-field energies, and $k_c = k_v$ as we just consider direct transitions. In Fig. 2.11 we evaluated the optical absorption including excitonic effects and not including them by using GW and DFT bandstructures. In the particular case of CNTs the absolute value of GW corrections are close to the absolute value of excitonic binding energies, that is why the first peaks positions calculated at BSE level and at DFT level are close to each other, as shown in the Fig. 2.11.

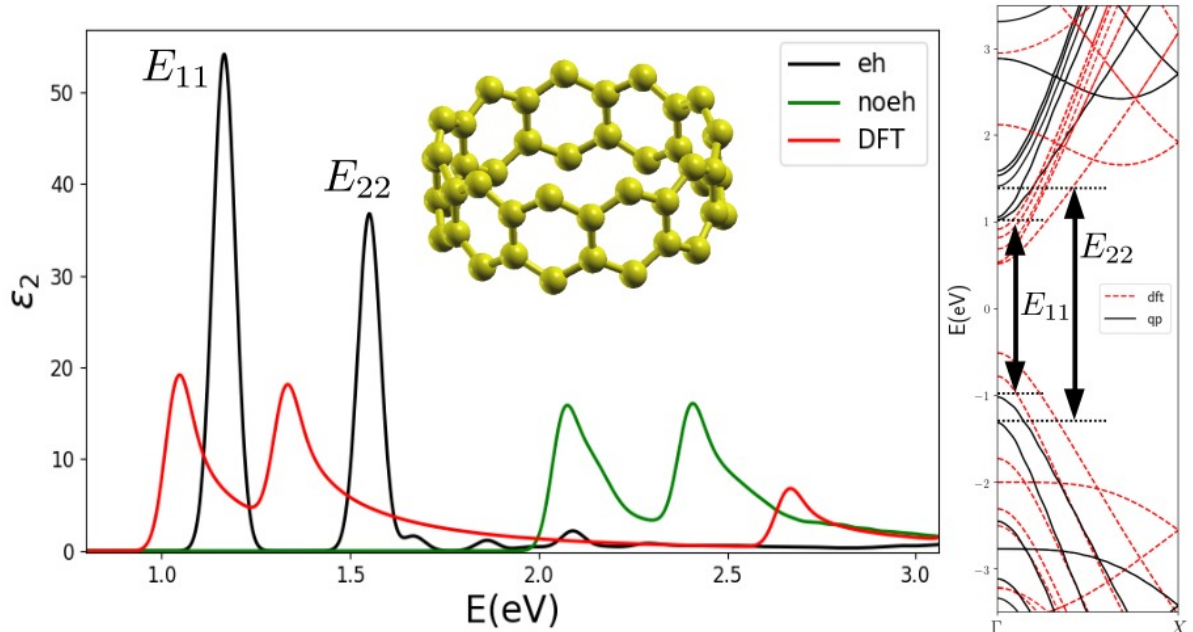


Figure 2.11: Left: Example of absorption spectra evaluated at three different levels: with electron-hole interaction (in black) and without it using GW (green) and DFT (red) results. Right: Bandstructures at DFT (red lines) and GW (black lines) levels. Note that the GW bands gap is greater than the DFT gap. The bands that give rise to the E_{11} and E_{22} absorption peaks are indicated. Those results are for CNT(11,0).

In our convergence studies we observed an important dependence of the E_{11} and E_{22} absorption peaks, although the difference $E_{22} - E_{11}$ and binding energies for both excitons are less dependent on convergence parameters, which means that E_{11} and E_{22} peaks are approximately rigidly translated when changing the convergence parameters.

2.3.3 Computational details

For the evaluation of the dielectric matrix elements we used a cutoff of 8 Ry and we included 500 conduction bands in the case of CNTs bonded to H and in the case of pristine CNTs we used a cutoff of 10 Ry and 1000 conduction bands. For both GW and BSE calculations we used $24/N_{cells}$ k points for coarse grids and $4 \times 24/N_{cells}$ k points for fine grids. To construct the kernel and to solve BSE we used 9 (15) conduction and valence bands for fine (coarse) grid.

For CNT bonded to a single H atom it is not possible to apply perturbative methods, as this is an open shell system [175]. Most theoretical works avoid this problem by studying CNTs bonded to two hydrogen atoms, one hydrogen atom and one functional group or two functional groups [131, 133, 135]. To overcome this problem, we added (removed) one electron in our calculations, so the impurity band was totally full (empty). In summary, we evaluated at DFT level the bandstructure and optical absorption for cases with $q=0, \pm 1$ (in reduced units) and other GW/BSE results were done only for $q=\pm 1$. The main consequence is that our CNTs are doped in two ways: by the covalent defect (chemical doping) and by the net charge (electrostatic doping). The electrical doping changes the impurity level position and consequently the excitons energies, so this procedure supports future developments of optical devices by using chemical doping and electrical doping.

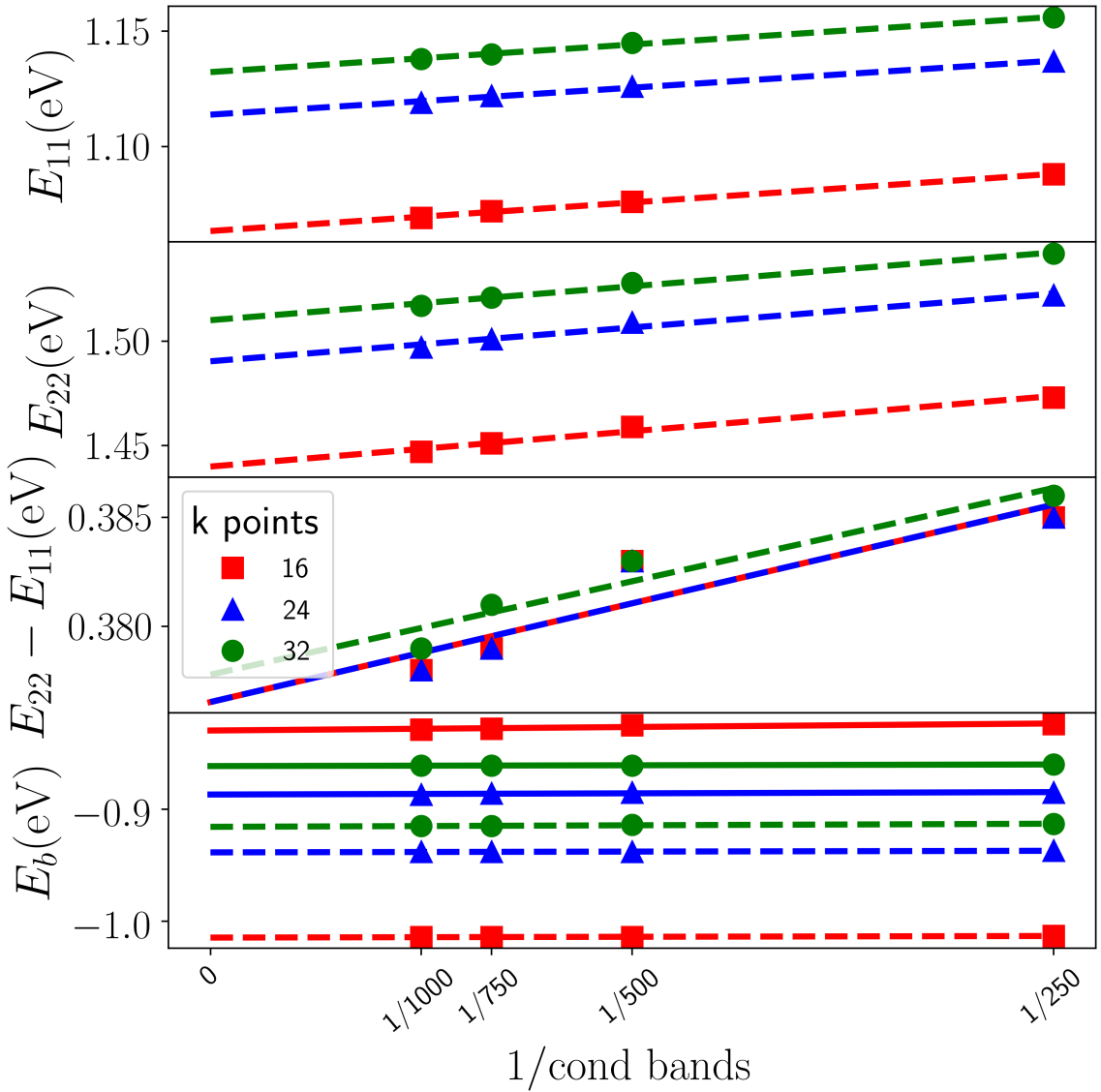


Figure 2.12: Convergence of E_{11} (a) and E_{22} (b) absorption peaks for NTC (11,0) with respect to the number of K points in coarse grid and number of bands for epsilon and sigma. The number of K points in the fine grid is eight times the number of K points in the coarse grid. $E_{22} - E_{11}$ difference (c) and binding energy (d) for those two excitons.

Chapter 3

Results and Discussions

3.1 Pristine Carbon Nanotubes

For semiconductor CNTs, the GW bandgaps are higher than LDA bandgaps as shown in Fig. 3.1 due to the inclusion of many-body effects. For the armchair CNTs the minimum gap is located at the Γ point and for the (6,5) chiral tube the minimum gap is slightly displaced from Γ .

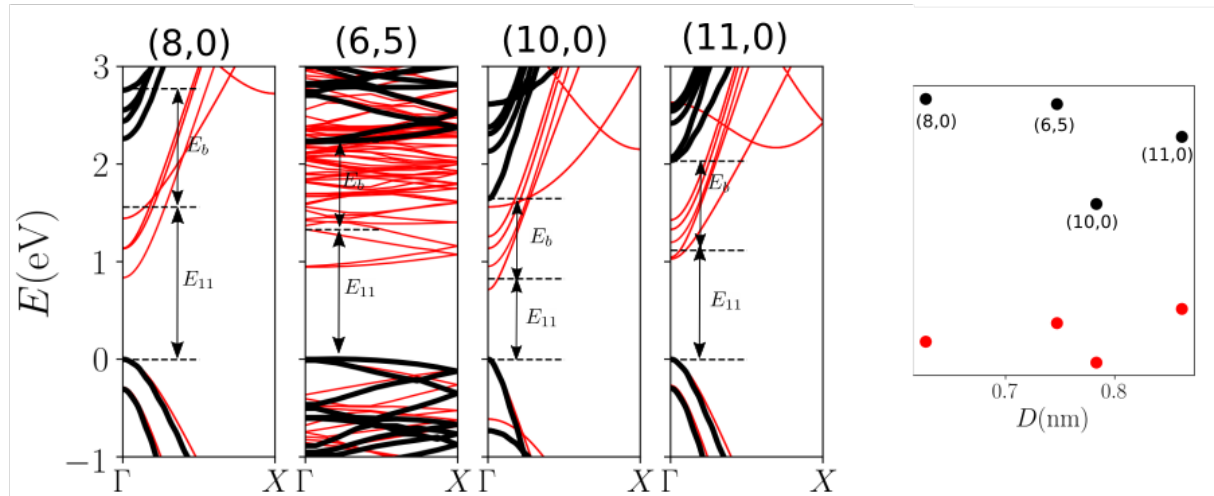


Figure 3.1: Left: bandstructure from of (8,0), (6,5), (10,0) and (11,0) pure CNTs at DFT (red lines) and GW levels (black lines). The E_{11} exciton energy and its binding energy are also indicated for each case. Right: Gap at Γ point at DFT and GW levels as a function of the tube diameter (in ascending order: (8,0), (6,5), (10,0) and (11,0)).

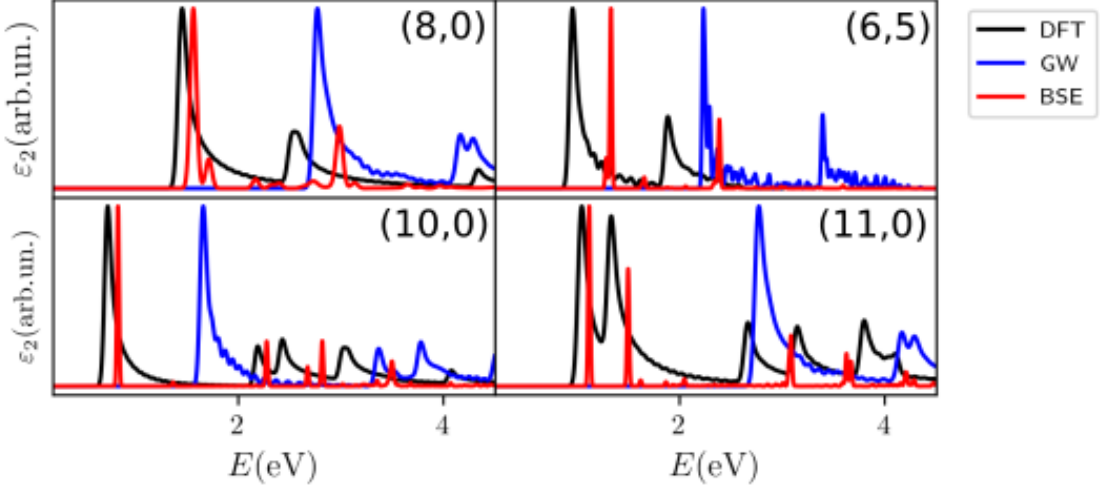


Figure 3.2: Absorption spectra for pure CNTs for different chiralities (indicated in the figure) evaluated at DFT, GW and BSE levels.

In Fig. 3.2 we show the absorption spectra evaluated at three different levels: at DFT and GW (including many body effects) levels and not including excitonic effects and at BSE level including excitonic effects. The GW absorption spectra shape is very similar to the DFT spectra, except by the peaks positions. This is expected, as the main change in the band structure from DFT to GW (in the CNTs specific case) is the energy gap as shown in Fig. 3.1.

Interestingly, the first E_{11} peak at DFT and BSE levels are close to each other due to a partial cancellation of effects: the many body corrections blueshifts the spectra and the electron-hole interaction (excitonic effects) redshifts it (not in the same magnitude), although at BSE level the peaks are sharper than the DFT case.

The exciton binding energy is defined by the difference between the exciton energy and the respective GW bandgap ¹

¹The GW bandgap is the difference $E_{c,\mathbf{k}_0} - E_{v,\mathbf{k}_0}$ (in the case of direct gap) where c and v are the bands that compose the exciton. In our calculations the excitons we study are approximately composed by one conduction and one valence bands.

$$E_b = E_{ex} - E_g \quad (3.1)$$

The E_{11} exciton energy and its binding energy in our calculations are indicated in Fig. 3.1. For CNTs the binding energies are much higher than usual semiconductors, due to the poor screening of 1D materials [68, 176]. In table 3.1 we summarize some results for some excitonic properties of the E_{11} exciton in pristine CNTs. The calculated E_{11} emission energy is close to experimental and theoretical values, except in the case for the (10,0) CNT. The binding energy is also close to previous reported values (with maximum differences about 200 meV).

We calculate the exciton size by two times the standard deviation (σ) of the electronic density using the following equation

$$\sigma = \sqrt{\int_{-\infty}^{\infty} \rho_{1D}(z_e - z_h)(z_e - z_h)^2 dz_e} \quad (3.2)$$

where ρ_{1D} is the one dimensional electronic density ($\rho_{1D}(x, y, z) = \int dx dy \rho(x, y, z)$) and z_e (z_h) is the z coordinate of the electron (hole). The hole position is kept fixed above one given carbon atom. In the Fig. 3.3 we show an example of the exciton wavefunction. The exciton sizes are about a few nanometers and the higher is the exciton binding energy less spread is the excitonic wavefunction, as expected. This trend is also chirality dependent as the exciton sizes for the (11,0) and (6,5) tubes are about the same, although the (11,0) CNT shows higher binding energy [85, 141].

The overall agreement between our results and previous experimental and theoretical is good, as shown in Table 3.1.

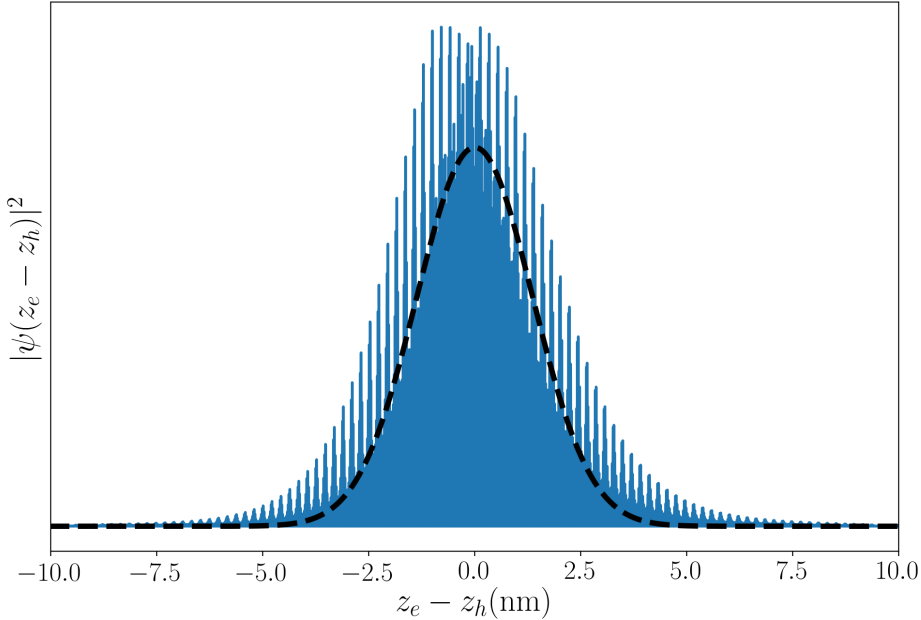


Figure 3.3: Example of exciton wavefunction as a function of the distance between the electron and the hole for the pristine (10,0) CNT. The dashed black curve is given by $e^{-(z_e-z_h)^2/\sigma^2}$ where σ is given by eq. 3.2.

3.2 Band Structure of Covalently Doped Carbon Nanotubes

We performed calculations of H doped CNTs (CNT-H) for (8,0), (10,0) and (11,0) CNTs as explained in section 2.2.2.

At both DFT and GW levels we observe a split of the double degenerate valence (conduction) bands [133,177] and the emergence of an impurity band in the middle of the bandgap, as seen in other theoretical works [130,138]. For CNT(10,0) the first valence (conduction) band splits in two bands (see Fig. 3.4), where one of them is close to the original double degenerated band, which we call v_1 (c_1) and the other one splits by Δ_v (Δ_c), which we call $v_{1'}$ ($c_{1'}$) as indicated in Fig. 3.4.

We observed variations of about 20meV (40meV) in the main gap at DFT (GW) level in relation to the pristine CNT main gap at the Γ point (transition v_1 to c_1) by varying the number of unit cells and in our TB calculations no substantial variation was observed.

(n,m)		E_{11} (eV)	E_b (eV)	Size (nm)
(8,0)	This work	1.565	1.208	2.0
	Exp	1.598 [80]		
	Theo	1.55 [100]	0.99 [100, 141]	
(10,0)	This work	0.831	0.816	3.9
	Exp	1.073 [80]		
	Theo	1.05 [126]	0.76 [141]	
(11,0)	This work	1.121	0.915	2.5
		1.19 [77]		
	Theo	0.923 [80]		
		1.191 [75]		
		1.17 [121]		
		1.21 [77]	0.76 [141]	
		1.062 [95]	0.860 [95]	
	Theo	1.2 [121]		
		1.332	0.902	
(6,5)	This work	1.272 [40]		2.5 (2.0 ± 0.7) [63]
		1.270 [80]		
		1.24 [94]		
		1.265 [116]		
		1.283 [75]		
	Theo	1.25 [121]		

Table 3.1: Exciton properties of pristine CNTs

Other theoretical works argue that the defect inclusion reduces locally the electronic bandgap [128], although in our results and other theoretical calculations [130, 133, 138] no substantial variations were observed.

For CNT(10, 0), by varying its supercell size to include 4, 6, 8 and 10 unit cells (in each unit there are 40 carbon atoms), we observed that the Δ_v and Δ_c splits decrease as the supercell size increases (defect concentration decreases) and there is a trend that those splits extrapolate to zero when the supercell size goes to infinity (see Figs. 3.5 and 3.6). On the other hand, the mean value of the impurity band converges to a constant value and its width goes to zero as shown in Fig. 3.6. This observation is confirmed with our TB calculations as indicated in figure 3.7. In ref. [7] splits of LUMO and HOMO levels of about 105-326 meV were observed in DFT calculations for 4nm long

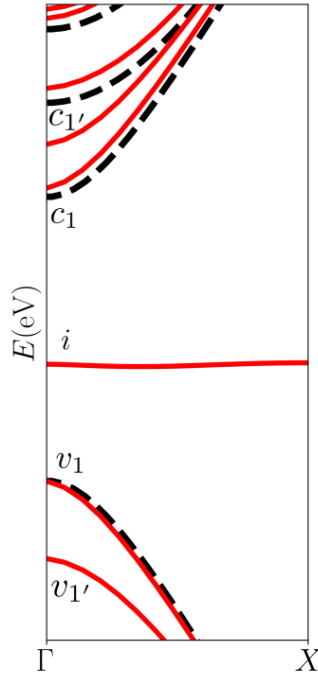


Figure 3.4: Band structure of pristine (black dashed lines) and CNT(10,0)-H (red solid line) calculated at DFT level. The double degenerate valence (conduction) band of pristine CNT splits in the v_1 and $v_{1'}$ (c_1 and $c_{1'}$) of the functionalized CNT and an impurity band i emerges in the middle of the bandgap.

(6,5) CNTs functionalized with benzene ². In ref. [130] splits of 8 meV (2 meV) in the valence (conduction) band were observed in (6,5) CNTs functionalized with acacPd(IV)-4-carboxylatephenyl. In refs [133,138] different defects also split degenerate valence and conduction bands in CNT(8,0). Those theoretical works shows a good agreement with our results for CNT functionalized with hydrogen atoms.

In our calculations with net charge $q = +1$ ($q = -1$), as the supercell size ranges from 1.7-4.2 nm, the hole (electron) doping varies from 0.60 to 0.24 holes (electrons) per nanometer. At both DFT and GW levels, we do not observe substantial variations in the main gap, although both the splits and the impurity state show relevant variations with the doping level. Other *ab initio* studies for pristine CNTs shows that doping changes the electronic bandgap and particularly hole doping decreases it about 0.8 eV for a doping of

²In ref. [7] the calculations were performed for finite CNTs (without periodic boundary conditions). Each CNT end was functionalized with hydrogen atoms.

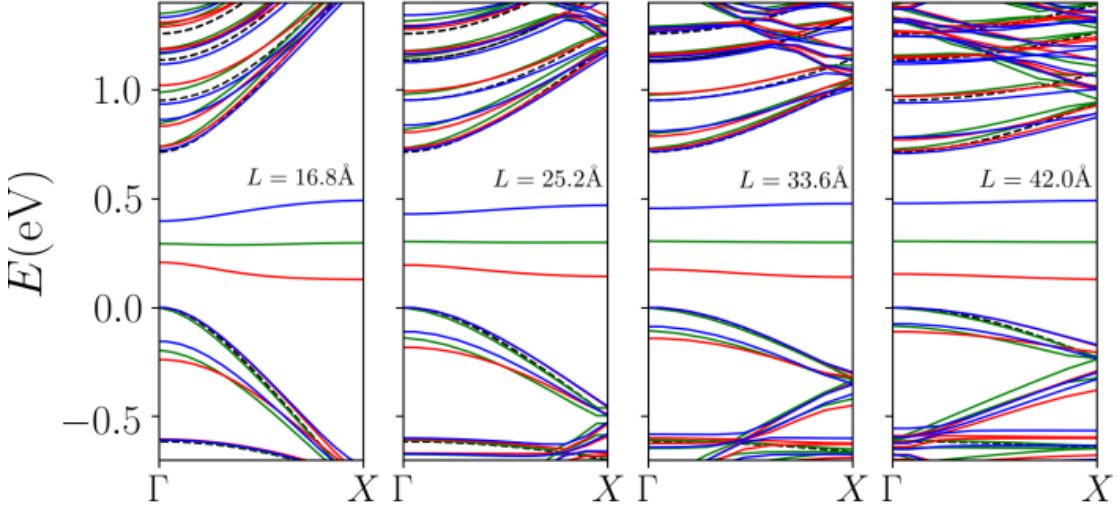


Figure 3.5: Bandstructure at DFT level of CNT(10,0)-H with different supercell sizes (indicated in the figure) and different net charges. Red lines, blue lines and green lines are $q = 1$, $q = -1$ and $q = 0$ cases respectively.

0.6 holes/nm, although the first absorption peak changes only by about 0.1 eV [91, 92]. Experimentally, a band gap reduction of 0.54 eV was measured at a doping density of 0.7 electrons/nm [93] and the intensity of the E_{11} absorption peak decreased when voltage was applied to the tube [90, 94]. In our case, the doping changes the impurity level of CNT-H, but for pristine CNTs the doping changes the occupation of the valence (conduction) band for positive (negative) doping.

We also performed calculation for CNT(8,0)-H and CNT(11,0)-H with four unit cells and net charges $q = 0, \pm 1$ (0.6 holes/electrons per nm). Results are summarized in Fig. 3.8. The splits tend to be smaller for larger diameters, as shown in Fig. 3.8.

In sections 3.4 and 3.5 we will look at two relevant excitons: E_{11} and E_- . The E_{11} exciton is the same of pristine CNT and is composed by the c_1 and v_1 bands and the E_- exciton is composed by the $v_{1'}$ and i (i and $c_{1'}$) bands for calculations with $q = 1$ ($q = -1$). For the CNT(10,0)-H the important bands are c_1 , $c_{1'}$, v_1 , $v_{1'}$ and i , and now we analyze them at the Γ point.

For the E_- exciton the conduction (valence) band is the impurity band for $q = 1$ ($q =$

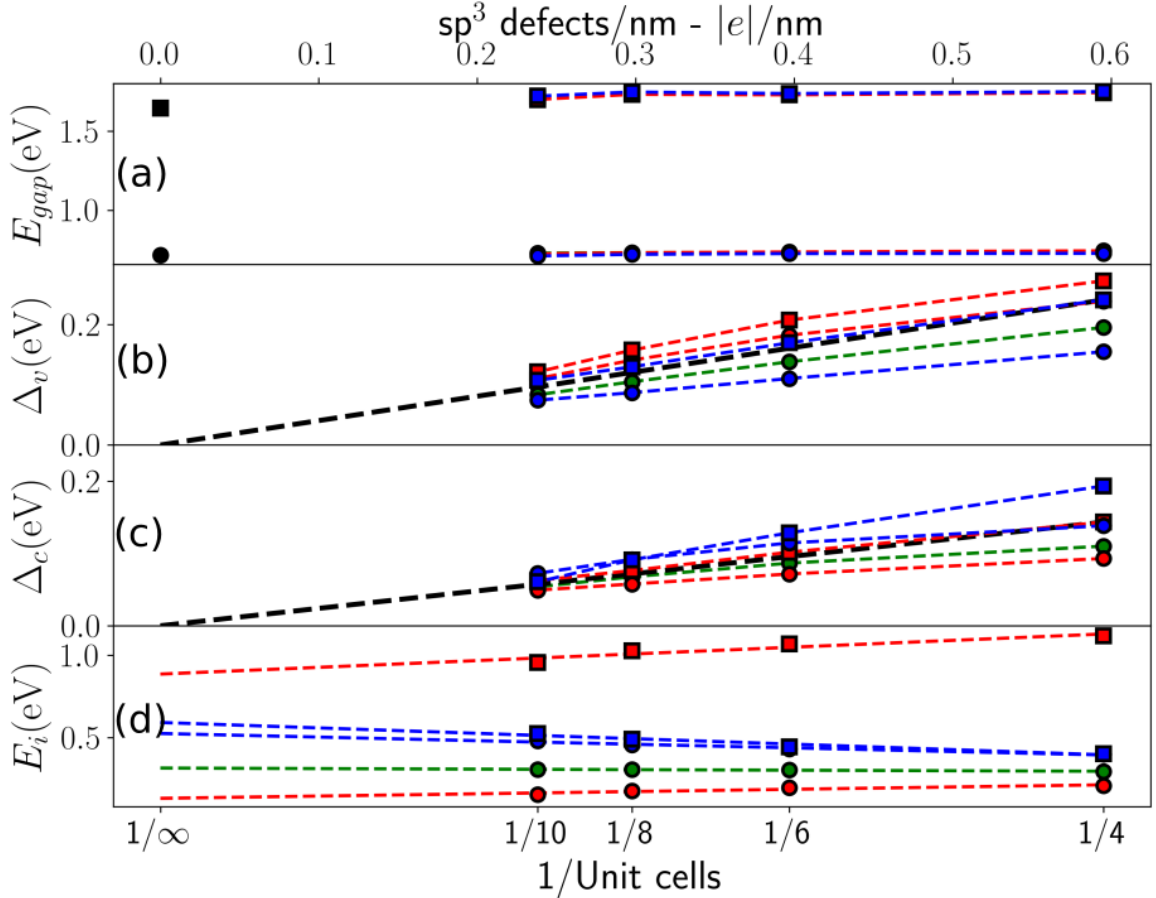


Figure 3.6: Main gap (a), splits of the first two valence bands (b), splits of the first two conduction bands (c) and impurity level (d) as function of the number of unit cells included in calculations (lower label) or the linear concentration of defects (upper label). Square (circle) symbols correspond to calculations at GW (DFT) level and red, blue and green symbols are calculations with $q = +1$, $q = -1$ and $q = 0$ respectively.

-1) systems. The impurity wavefunction is itself localized around the impurity, what agrees with other theoretical works [130]. According to our plots of the electronic density for the impurity band ($\rho_i(\mathbf{r}) = \psi_i(\mathbf{r})\psi_i^*(\mathbf{r})$) can be written approximately as $\rho_i(\mathbf{r}) \approx e^{-z^2/\sigma_z^2}e^{-\theta^2/\sigma_\theta^2}f(z, \theta)$, where $f(z, \theta)$ is a periodic function in both z and θ coordinates. In Fig. 3.9 we show plots of the $\rho_i(\mathbf{r})$ over the tube surface, showing that it is localized around the impurity. Using the effective mass approximation the exciton wave function is given by

$$\Psi_{ex}(r_e, r_h) = F(r_e - r_h)\psi_c(r_e)\psi_v(r_h),$$

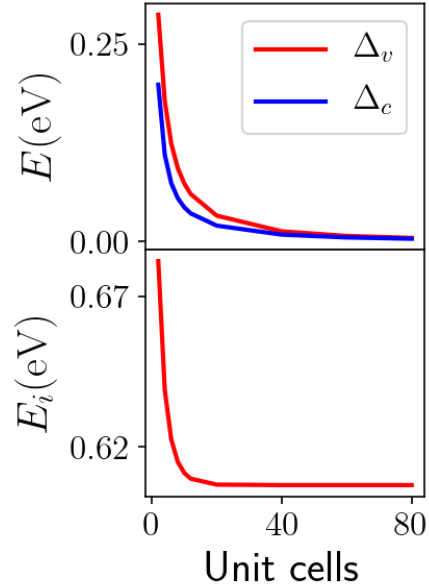


Figure 3.7: TB dependence of the splits of the valence (conduction) band and the impurity state as a function of the unit cells included in the calculation for CNT(10,0)-H. TB parameters used for the calculation are the ones in the first row of table 3.2.

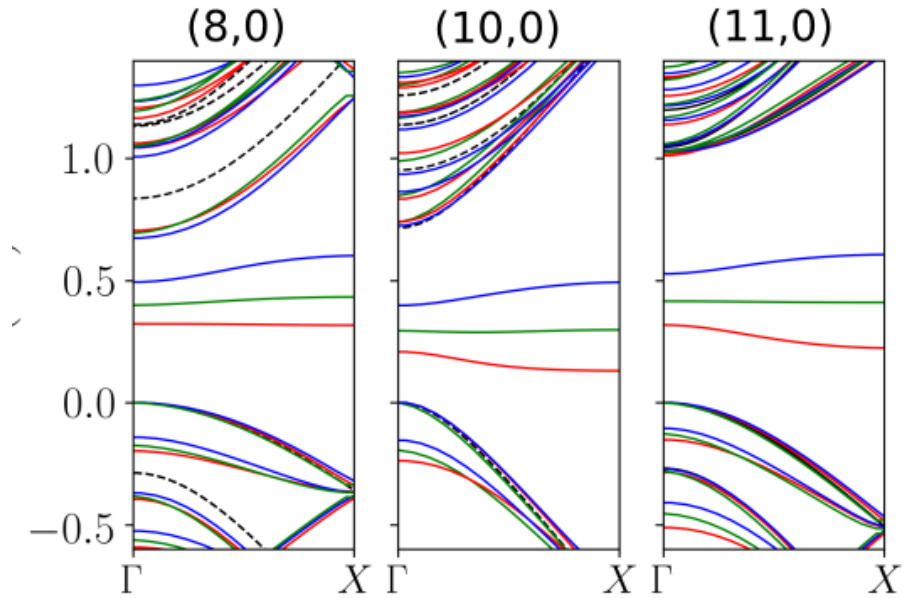


Figure 3.8: DFT bandstructures for (8,0), (10,0) and (11,0) CNTs with four unit cells (defect concentration equals to 0.6 defect/nm). Red lines, blue lines and green lines correspond to net charges of $q = 1$, $q = -1$ and $q = 0$ respectively.

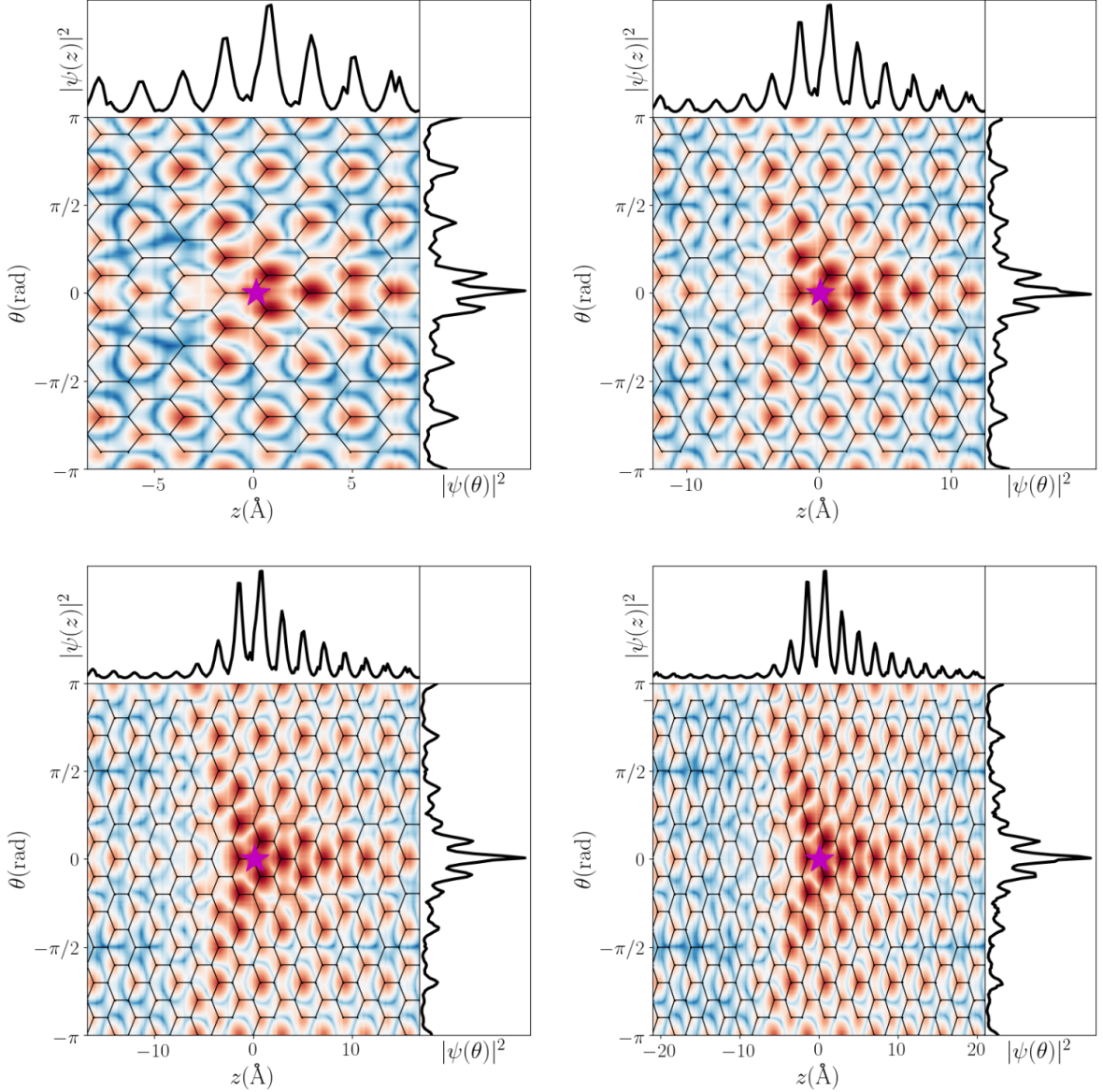


Figure 3.9: Logarithm of the electronic density in polar coordinates for the impurity state in calculations with 4 (a), 6 (b), 8 (c) and 10 (d) unit cells of CNT(10,0)-H. The atomic positions are presented as well. The linear electronic density in the axial and radial directions are also presented and were calculated by $|\psi(z)|^2 = \int r dr d\theta |\psi(z, \theta, r)|^2$ and $|\psi(\theta)|^2 = \int r dr dz |\psi(z, \theta, r)|^2$. The hydrogen atom is represented by the pink star at the origin.

where $F(r)$ is the envelope function. If $\psi_c(r_e)$ or $\psi_v(r_h)$ is localized, then so is the exciton wavefunction. We can conclude that the exciton composed by the impurity band is localized around the defect. In Appendix A we calculated analytically an excitonic wave

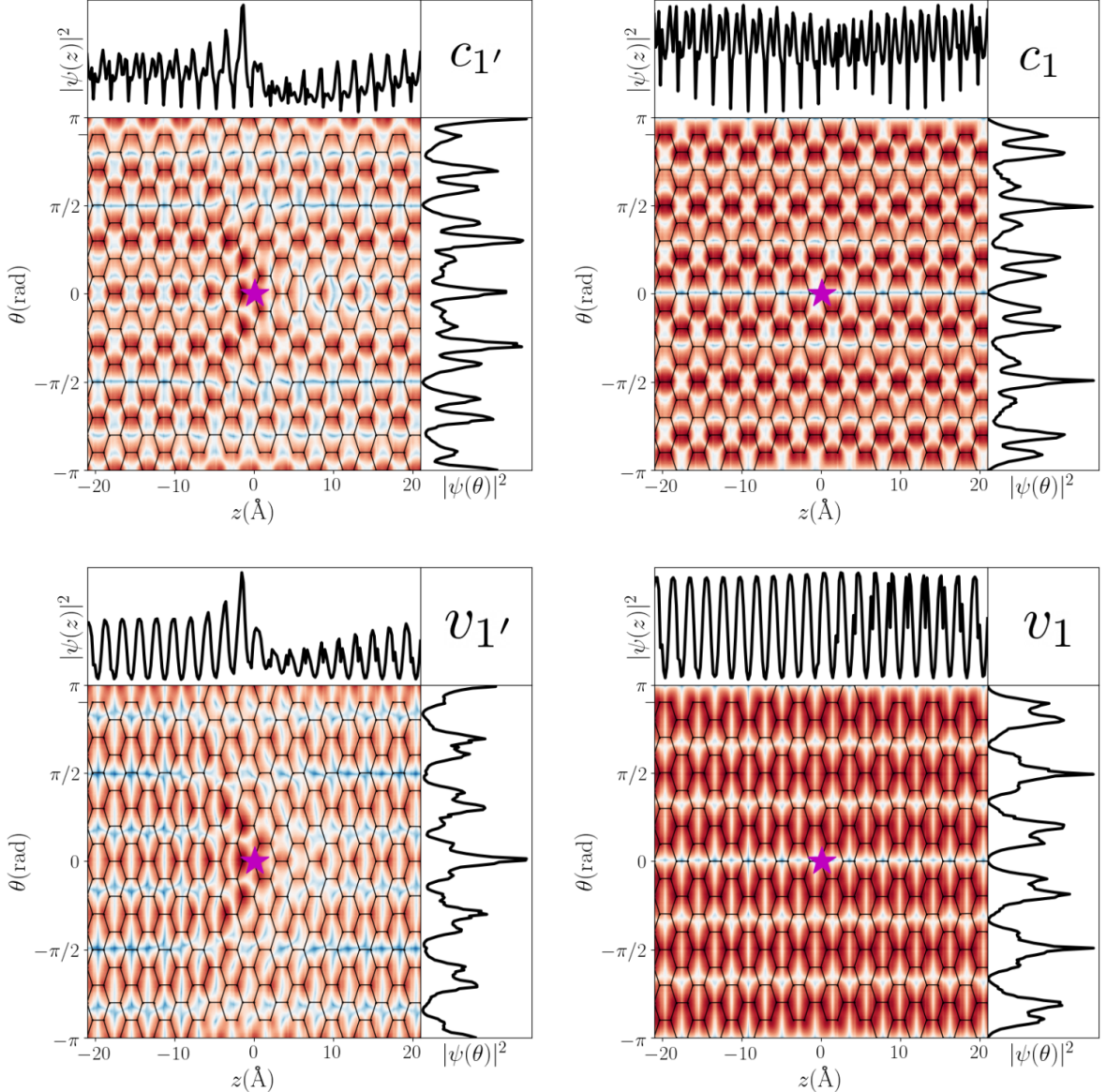


Figure 3.10: Electronic density in polar coordinates for the c_1 , $c_{1'}$, $v_{1'}$ and v_1 bands states in calculations with 10 unit cells of CNT(10,0)-H. The atomic positions are presented as well. The linear electronic density in the axial and radial directions are also presented and were calculated by $|\psi(z)|^2 = \int r dr d\theta |\psi(z, \theta, r)|^2$ and $|\psi(\theta)|^2 = \int r dr dz |\psi(z, \theta, r)|^2$. The hydrogen atom is represented by the pink star at origin.

function composed of a localized impurity wave function.

For CNT(10,0)-H we also observed strong perturbations around the hydrogen atom for the $c_{1'}$ and $v_{1'}$ eigenvectors and c_1 and v_1 are less perturbed (see Fig. 3.10). It is interesting to note that in the angular coordinate, the c_1 and v_1 ($c_{1'}$ and $v_{1'}$) wavefunctions show a

node (maximum) for the electronic density for $\theta = 0$, which is the angular coordinate of the hydrogen atom. The impurity state also shows a maximum for $\theta = 0$ which agrees with the coupling of the impurity state with $v_{1'} (c_{1'})$ for the case $q = 1$ ($q = -1$) and the uncoupling between the impurity state and v_1 or c_1 .

We evaluate the localization of the defect-state wavefunction by analyzing the z -projected electronic density $\rho(z) = \int dx dy \psi(x, y, z) \psi^*(x, y, z)$ in Fig. 3.11 for various supercell sizes (this particular figure shows only the $q = 0$ case). In a more quantitative way, we also estimate the localization length by calculating the standard deviation σ in a supercell, using the following equation

$$\sigma = \sqrt{\int_{-L/2}^{L/2} \rho(z)(z - \bar{z})^2 dz} \quad (3.3)$$

where we make sure to place the supercell origin at the defect position in order to avoid spurious periodic supercell effects in the integration. The localization length is given by $\delta = 2\sigma$. In Fig. 3.12 we show the localization lengths δ as a function of the supercell size and for $q = 0, \pm 1$. In our largest supercell size ($L \approx 4.2\text{nm}$) the localization length does not converge as expected, so we fit our data with the expression $\delta(L) = \delta_0(1 - \exp(-L/L_c))$, where δ_0 is the converged localization length and L_c is the length where $\delta \approx 0.63\delta_0$. By looking at the fits in Fig. 3.12 the localization length converges for supercell sizes about 8 nm (twice our largest value) and it converges to 1.7 nm, 2.0 nm and 2.6 nm for $q = 0$, $q = -1$ and $q = 1$ cases, respectively.

3.3 Impurity Level

As we will discuss in sections 3.4 and 3.5, the redshifted absorption peak is related to optical transitions involving the impurity state, therefore the exciton emission energy is determined by it. In that sense, from an application point of view, we propose that electrostatic doping may be used to control the exciton energy. In other words, the

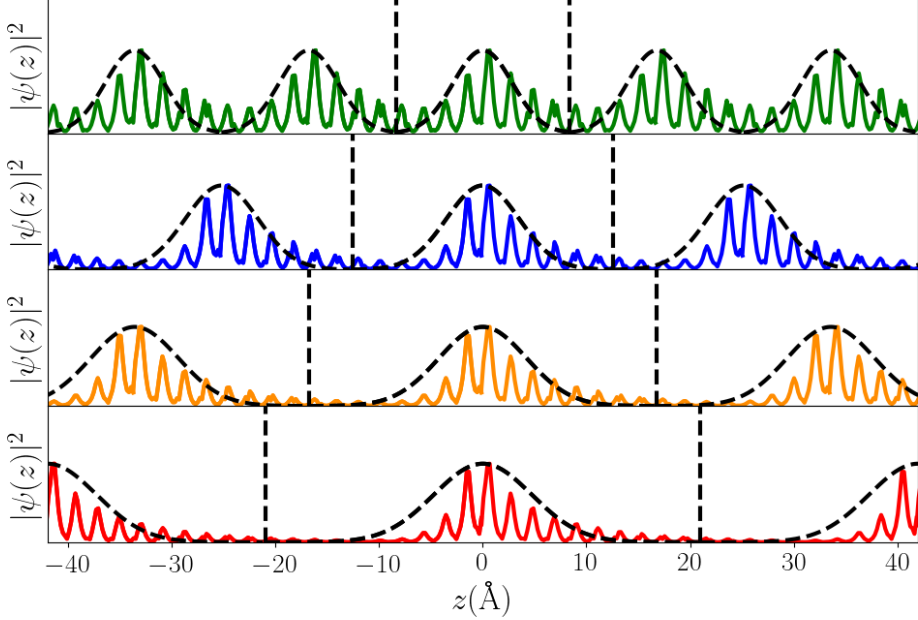


Figure 3.11: Linear electronic density along the z direction for the impurity band for calculations with $L = 4$ (a), 6 (b), 8 (c) and 10 (d) unit cells. Black dashed lines are gaussian functions $e^{-(z/\sigma)^2}$, where σ is the standard deviation given by eq. 3.3. Those results are calculations at DFT level with $q = 0$.

chemical doping breaks the CNT symmetry (see section 3.5) and creates impurity states and the electrostatic doping tunes the impurity state level. To validate this point, we performed DFT calculations for the CNT(10,0)-H changing the defects concentration and electron (hole) doping and these results are shown in Fig. 3.13. Interestingly, by changing the defect concentration and the doping in our calculations, we observed variations of about 0.5 eV in the impurity level and 0.1 (0.2) eV for the split of the valence (conduction) band.

We also modified our TB model to include hydrogen atoms. In order to reproduce our DFT results for the splits and the impurity level, we included a first neighbor hopping t_{HC} , between the hydrogen atom and the neighboring carbon atom and on-site energies E_{0H} for the hydrogen atom.

To obtain the best parameters t_{HC} and E_{0H} , we performed TB calculations by changing these parameters and we compared with our DFT results for the CNT(10,0)-H in the case

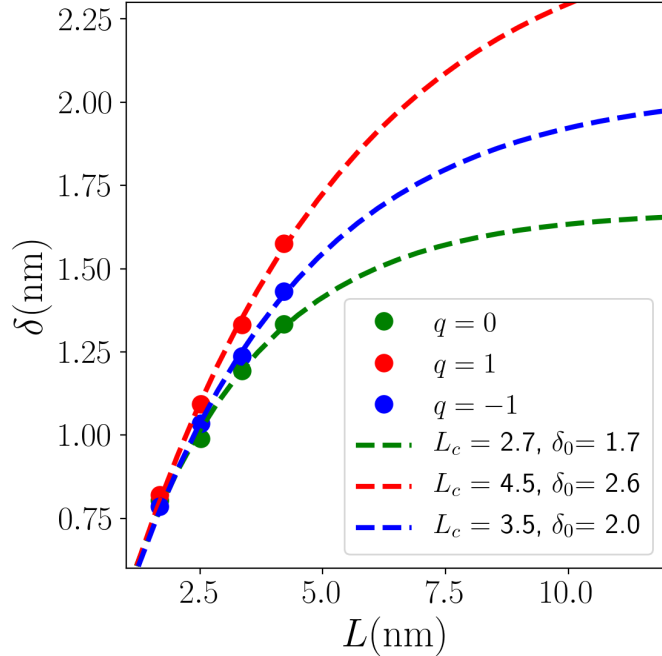


Figure 3.12: Localization length of the impurity state calculated at DFT level. Green, red and blue symbols correspond to $q = 0$, $q = 1$ and $q = -1$, respectively. This data was fitted with the expression $\delta(L) = \delta_0(1 - \exp(-L/L_c))$ (dashed lines) in each case. The fitted parameters are shown in the legend of the figure and their unit is nanometers.

we have four unit cells (0.6 defects per nm) and doping $q = 0, \pm 1$ (0.6 holes/electrons per nm). The results are summarized in Fig. 3.14, where the splits and impurity level are scaled by the main gap and t_{HC} and E_{0H} are scaled by $t_{CC} = 4.681\text{eV}$, the carbon-carbon hopping reported in table 2.1. The optimal parameters are reported in table 3.2.

	t_{HC} (eV)	E_{0H} (eV)
$q = 0$	1.535	-0.197
$q = 1$	0.868	-0.385
$q = -1$	2.682	0.122

Table 3.2: Optimal TB parameters that reproduce DFT results for CNT(10,0)-H with four unit cells and net charges $q = 0, \pm 1$. The hopping between carbon atoms is still $t_{CC} = 4.681\text{eV}$ and on-site energies for carbon atoms are zero.

In our calculations we use periodic boundary conditions and one hydrogen atom per supercell with N_{cells} unit cells. Therefore, the simulated system is an infinite CNT with H atoms distant from each other by the distance $N_{cells}L$ ($L \approx 4.2\text{\AA}$) and all of them

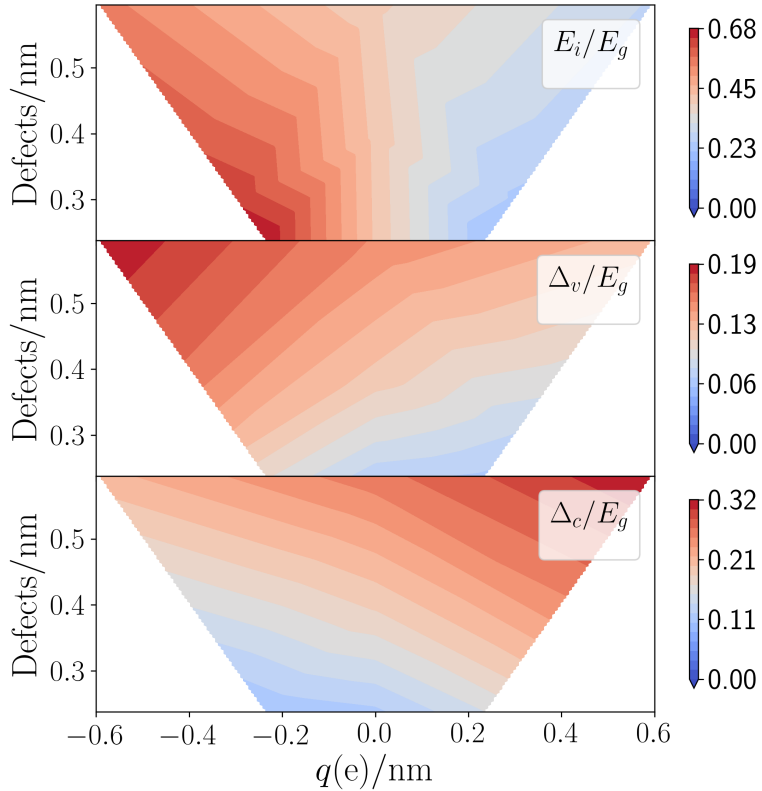


Figure 3.13: Impurity state and split of the conduction and valence bands calculated at DFT level for different quantities of defect concentration and doping. The doping was calculated until the maximum (minimum) value to make the impurity band totally full (empty).

pointing in the same direction. This situation is not what is expected experimentally, so to study more realistic cases we performed TB calculation of CNT(10,0) bonded to randomly arranged H atoms over the tube surface for different concentrations of defects.

In calculations with one single defect, we observed one impurity state in the middle of the bandgap. Differently from that, in the case with N_H H atoms bound to the tube we observed N_H bands in the middle of the bandgap. We also observed that different samples with the same concentration of defects presented different distribution of the impurity bands on the gap as shown in Fig. 3.15.

Therefore, we performed 100 calculations (each one for a different random sample) for different defects concentrations (ranging from 0.2 to 23.8 H atoms per nm) and from this

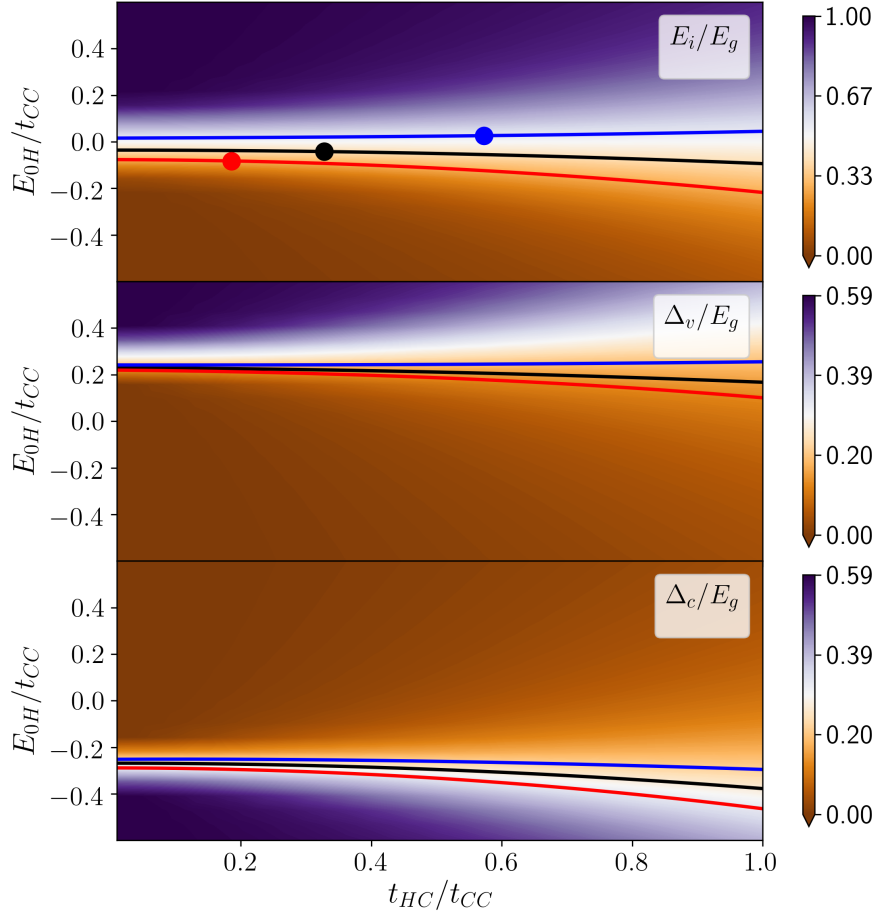


Figure 3.14: Impurity level E_i and splits Δ_v and Δ_c varying the parameters t_{HC} and E_{0H} (see text) calculated at TB level for the CNT(10,0)-H with four unit cells. Black, red and blue solid lines are level curves where the difference between TB results and DFT results for CNT(10,0)-H with $q = 0$, $q = +1$ and $q = -1$, respectively, are less than 10^{-3} . In the first panel dots are the best TB parameters to reproduce the DFT impurity level and are listed in table 3.2

data we did some statistical analysis of the impurity levels considering all samples. Those calculations were performed for (10,0) CNT, which has approximately 95 carbon atoms per nm, then in the calculations with the largest defect concentration of 23.8 H atoms per nm the H to C atoms ratio is 1:4 and the supercell included 20 unit cells (its length is 8.4 nm and it contains 800 carbon atoms).

We observed that both the mean value and the dispersion of the impurity levels increase with the defect concentration, as shown in Figs. 3.16 and 3.17. The valence and

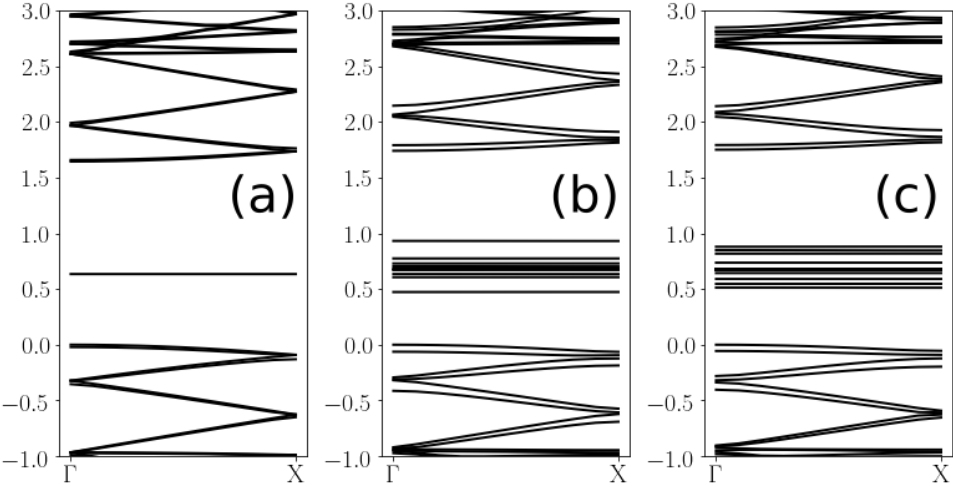


Figure 3.15: TB band structure of CNT(10,0) bonded to 1 H (a) or 10 H (b and c) atoms. (b) and (c) are calculations done with the same concentration of defects but are different random samples. Those calculations were done with 20 unit cells in the supercell (supercell length is 8.4 nm and it contains 800 carbon atoms).

conduction band splits also increase with the defect concentration, as shown in Fig. 3.17. In the ordered defects case the splits increase linearly and for the random defect case those splits converge to constant values below 0.1 eV. By looking at the Density of States (DOS) in Fig. 3.16 we observed a high intensity peak in the middle of the bandgap.

3.4 Optical Properties of Covalently Doped Carbon Nanotubes

Following the results of the previous section, we calculated the optical absorption of CNT-H. In Fig. 3.19 we show results evaluated at DFT and BSE levels for CNT(10,0)-H.

We observed a variety of new peaks in agreement with experimental and theoretical works [7, 42]. In the optical absorption for CNT with charge +1 (-1) we observed new redshifted peaks at BSE level, which we call E_- and those peaks are related to transitions from the $v_{1'}$ band to the impurity band (from the impurity band to the $c_{1'}$ band) that are redshifted with respect to the peaks associated to the transition $v_1 \rightarrow c_1$ (E_{11}). In section 3.5 we discuss those results from a Group Theory point of view.

At the BSE level the E_{11} peaks are blueshifted with respect to the pristine case by

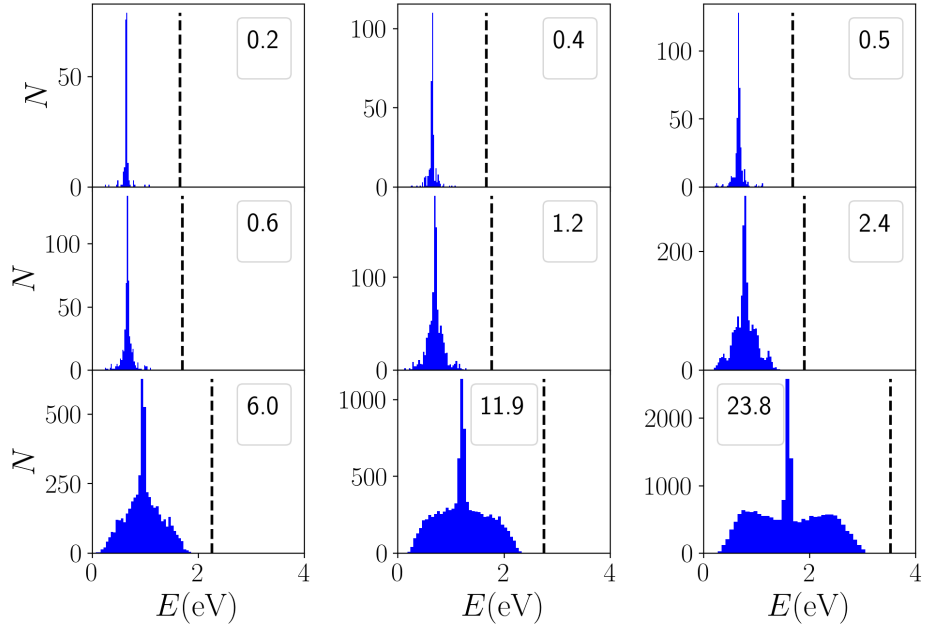


Figure 3.16: Distribution of impurity levels considering all 100 calculations for several defect concentrations, indicated in each subpanel which units are defect/nm. Black dashed lines represent the bottom of the conduction band and the top of the valence band is set to zero.

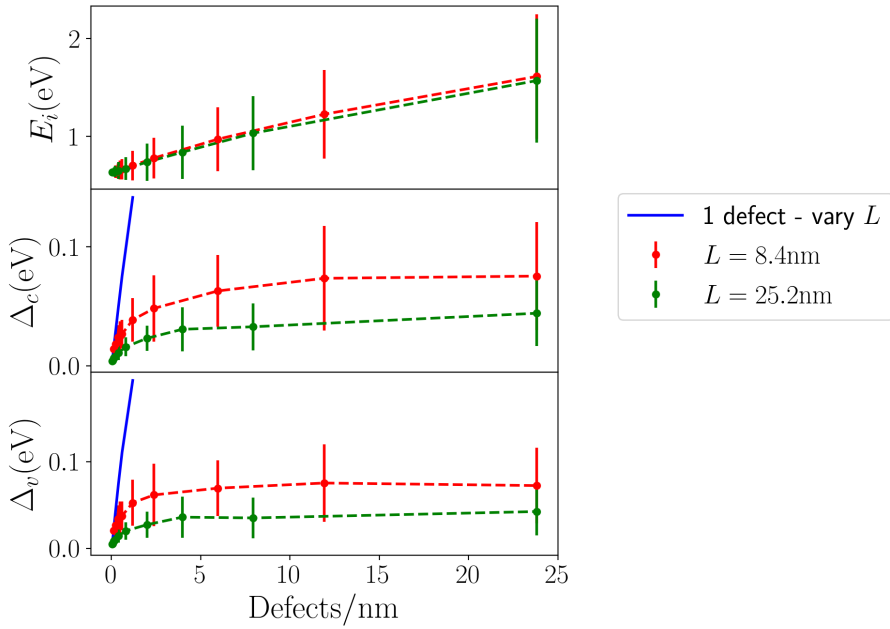


Figure 3.17: Impurity level (upper panel), split of the conduction band (middle panel) and split of the valence band (lower panel) as a function of the defect concentration.

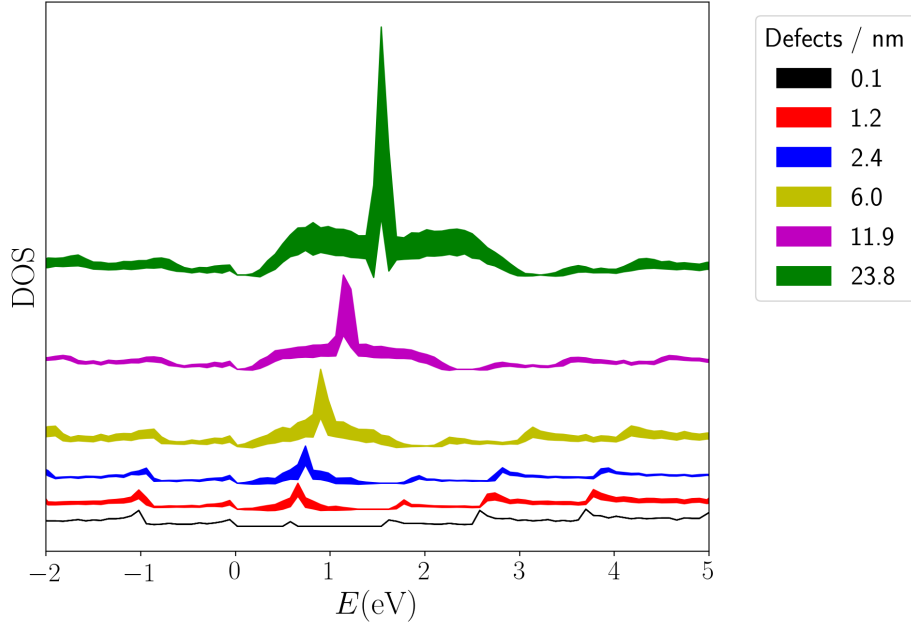


Figure 3.18: Mean DOS for several defect concentrations. The linewidth in each case is twice the standard deviation of the samples.

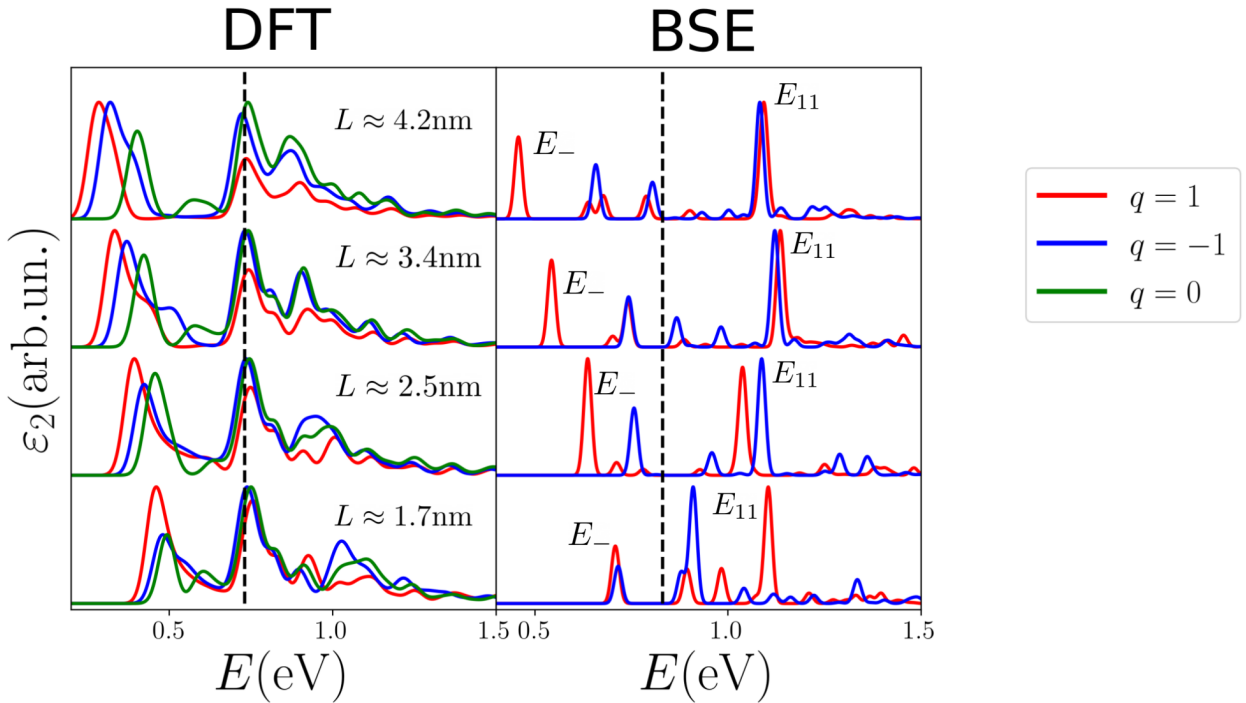


Figure 3.19: Absorption spectra at DFT (left) and BSE (right) levels for CNT(10,0)-H with charge $q = 0$ (green curves), $q = 1$ (red curves) and $q = -1$ (blue curves) for different supercell sizes. Black dashed lines are results for E_{11} in pristine CNT ($q = 0$) for reference.

about 300 meV. In experimental works the inclusion of defects changes the intensity of the original E_{11} peak but does not change its position [7, 42]. These blueshifts are roughly 0.2 eV. Typically, BSE calculations have uncertainties in the order of 0.1 eV (in comparison to experimental values). We believe that those blueshifts are due to the convergence parameters of our calculations as those *ab initio* calculations are very challenging, but they do not affect the main conclusions of this work. Based in our convergence studies (section 2.3.3), the E_{11} and E_{22} energies are very sensitive to the convergence parameters, although the $E_{11} - E_{22}$ difference and the binding energy for pristine CNTs are less affected by these parameters (see Fig. 2.12). For this reason, whenever possible, we will focus our analysis on the difference between E_- and the corresponding E_{11} peak.

Interestingly, we observe similar trends in DFT calculations: redshifted peaks related to transitions to (from) the impurity for $q = +1$ ($q = -1$) systems. We also observe a two-peak structure near the E_{11} transition, corresponding to a split of the $v_1 \rightarrow c_1$ and $v_{1'} \rightarrow c_{1'}$ transitions. These splits are related to the valence and conduction band degeneracy breaking discussed in the previous sections. At the BSE optical spectra, such $v_{1'} \rightarrow c_{1'}$ transitions appear to have very small intensities and the oscillator strength seems to shift to the $v_1 \rightarrow c_1$ transition.

As the E_{11} energy at the BSE level varies with the supercell size (much more than for DFT results) we analyzed the energy differences $\Delta E = E - E_{11}$ in Fig 3.20, by shifting the spectra and placing the E_{11} peak at origin of the energy axis in each case. The redshifts are about 0.2-0.6 (0.2-0.4) eV for systems with net charge $q = +1$ ($q = -1$). Nagatsu et. al [140] fitted experimental data for redshifts due to hydrogen absorption in several CNT chiralities and diameters and obtained an expression $\Delta E = 68/d^2$ [meV] (d is the tube diameter), so for (10,0)CNT-H the redshift is expected to be (110 ± 10) meV³. In this experiment the CNTs were functionalized after exposed to atomic hydrogen gas and information about the defect concentration over the tube surface is not available [140].

³The error of 10 meV is due to the data dispersion in ref. [140]

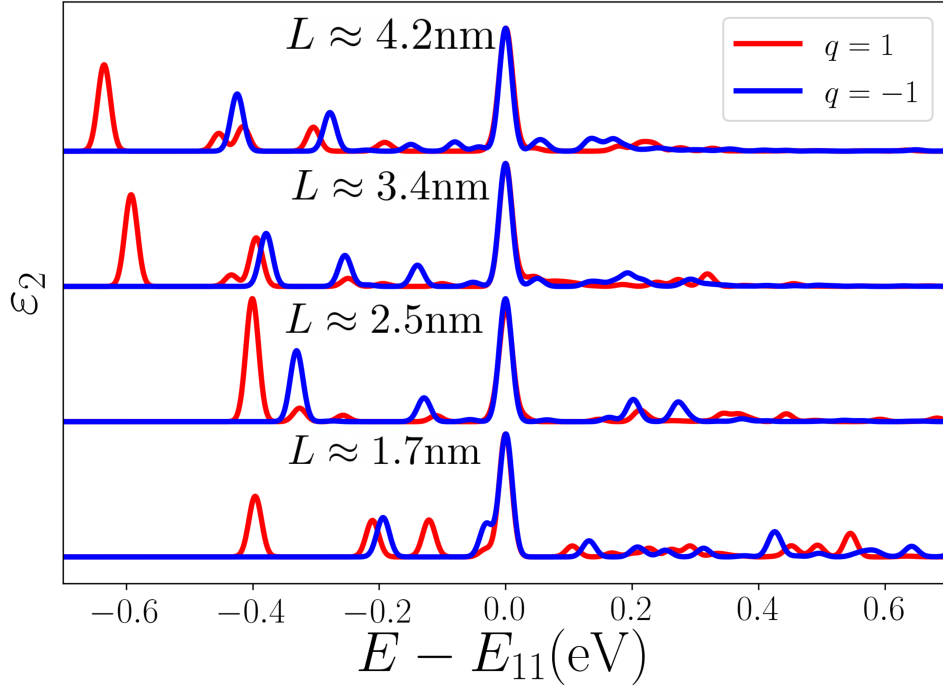


Figure 3.20: Redshifts in the absorption spectra taking the E_{11} transition energy as reference and at BSE level for CNT(10,0)-H with charge $q = +1$ (red lines) and $q = -1$ (blue lines). Supercell sizes are indicated in the figure.

However, this is an important piece of information for comparing theory with experiment. In Figs. 3.21 (g) and (h), we show our calculation of the redshift as a function of defect concentration. For both charge states, there is a monotonic increase of the redshift as the defect concentration decreases (larger supercells), at both BSE (squares) and DFT (circles). The smallest calculated redshifts are about 0.25 eV. Therefore, to provide a quantitative agreement with experiment [140], the defect concentration in the experiments would have to be larger 0.6 defect/nm (our largest calculated value, corresponding to 4 unit cells).

In ref. [126] experimental results for CNT(10,0) functionalized with 4-methoxybenzene and 4-bromobenzene show a redshift of about 120 meV (information about the defect concentration was not available). Time Dependent DFT (TDDFT) calculations for finite 12 nm length CNT(10,0) functionalized with 4-bromobenzene found redshifts from 20 to

270 meV, depending on the defects configurations [126]⁴. In ref. [121] PL measurements for CNT(11,0) functionalized with 4-methoxybenzene at 4K were done for 13 different samples and in just two cases the E_{11} is visible. The E_- peaks are in the range 0.95-0.98 eV, which corresponds to redshifts equal to 220-190 meV [121].

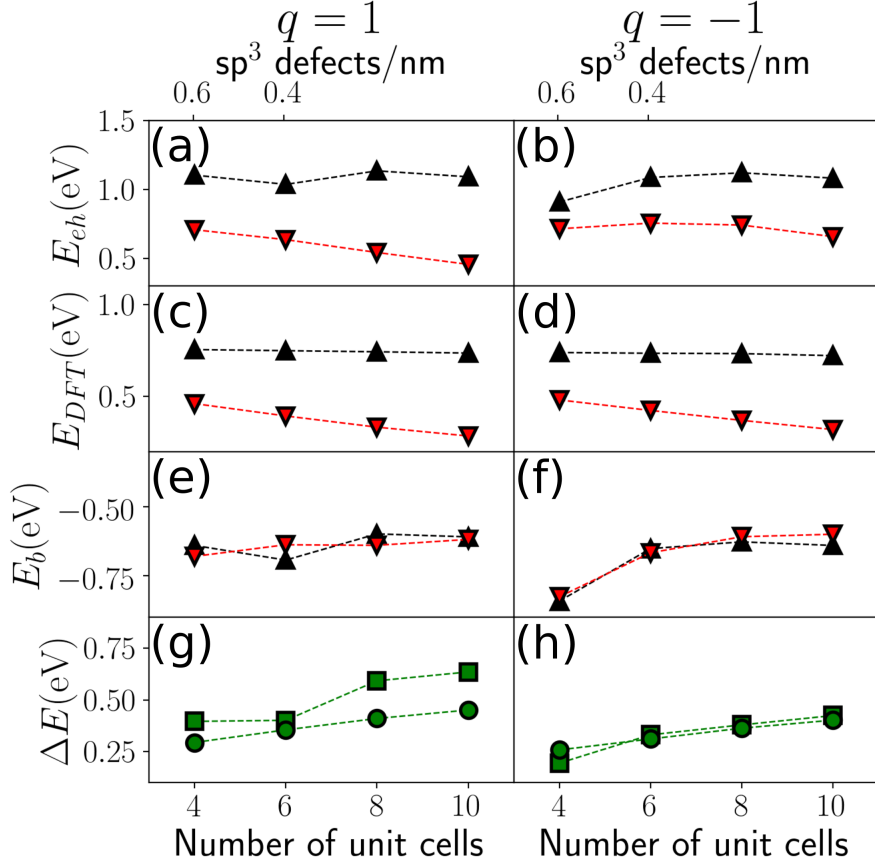


Figure 3.21: (a-d): Peak positions for E_{11} (black symbols) and E_- (red symbols) excitons calculated with BSE (a and b) and at DFT level (c and d). (e-f): Binding energies for E_{11} (black symbols) and E_- excitons (red symbols). (g-h) Redshifts ($|E_- - E_{11}|$) calculated using BSE (squares) and DFT (circles) results. Left (right) panels are results for $q = 1$ ($q = -1$).

In the other panels of Fig. 3.21 we summarize the concentration (or supercell size)

⁴In those calculations two defects are bound to the CNT: one hydrogen atom and the desired functional group. The configurations may be ortho, meta or para. This is done to avoid calculations with open shells.

dependence of the E_{11} and E_- peaks. Panels (a) and (b) show, for both charge states, the BSE optical transition energies (at the peaks) for E_{11} black (upper triangles) and E_- (red lower triangles). The same quantities are shown in panels (c) and (d), at the DFT level. In DFT, it is clear that E_{11} energies are independent of defect concentration, but E_- increases with defect concentration. In panels (e) and (f), we show that excitons binding energies are roughly independent on defect concentration for both E_{11} (red) and E_- (black), except perhaps for the case of 4 unit cells and negative charge state. In all cases, E_{11} and E_- have roughly the same binding energies. Finally, as we commented above, we show in panels (g) and (h) that, as the concentration of defects increases, the redshift, both at DFT and BSE levels, decreases.

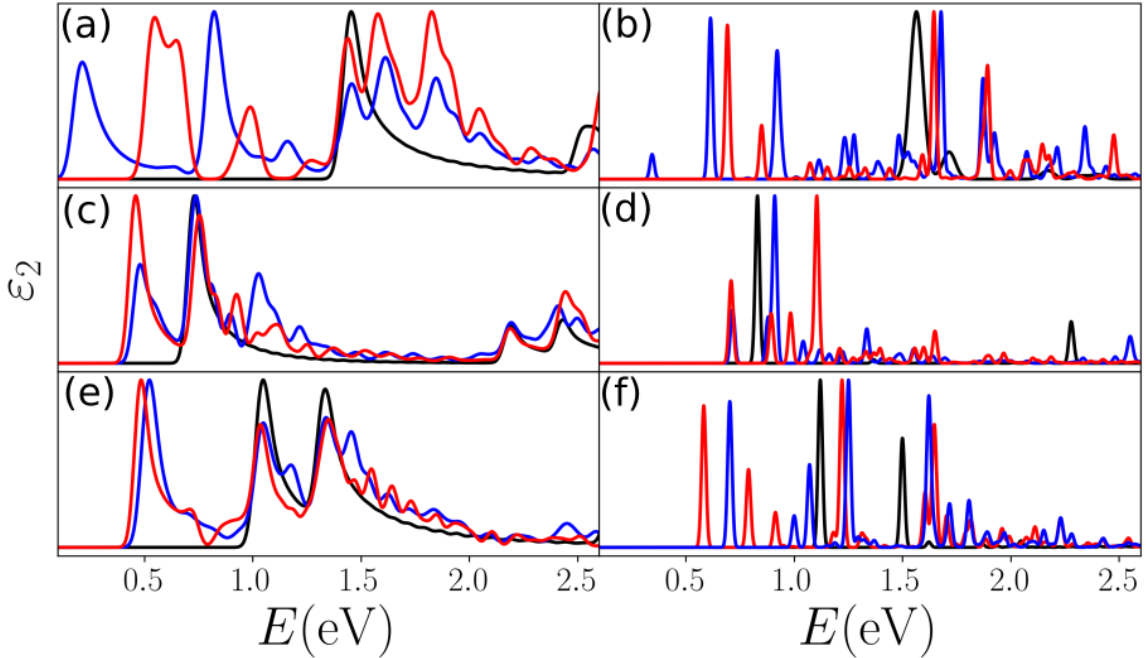


Figure 3.22: Absorption spectra for (8,0) (a and b), (10, 0) (c and d) and (11, 0) (e and f) without defect (black lines) and with hydrogen atoms (0.6 H atoms per nm) and with charge $q = 1$ (red curves) and $q = -1$ (blue curves). DFT results are in the left and BSE results are in the right.

In Figs. 3.22, 3.23 and 3.24 we search for the diameter dependence of exciton properties by analyzing the results for (8,0), (10,0) and (11,0) tubes, using the same defect

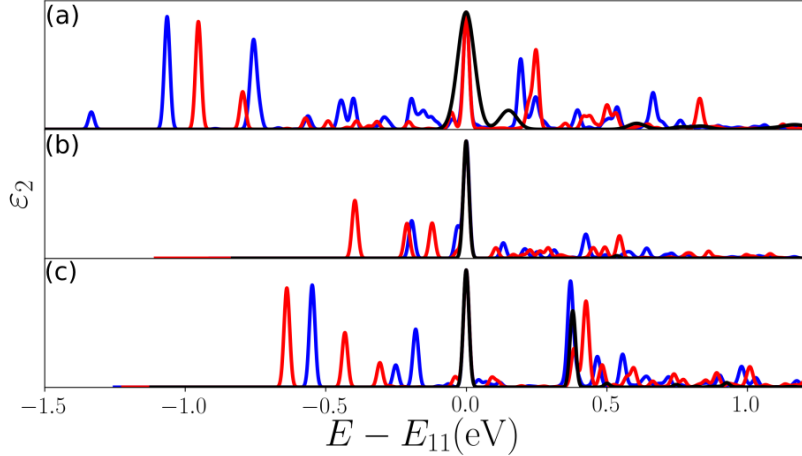


Figure 3.23: Redshifts in the absorption spectra of (8,0) (a), (10, 0) (b) and (11, 0) (c) without defect (black lines) and with hydrogen atoms (0.6 H atoms per nm) and with charge $q = 1$ (red curves) and $q = -1$ (blue curves) at BSE level.

concentration of 0.6 hydrogen atoms per nm (4 unit cells). Figure 3.22 shows the absorption spectra for all 3 CNTs and in both charge states, both in DFT (left panels) and in BSE (right panels). Again, using the E_{11} optical transition in each case as an energy reference, Fig. 3.23 displays the E_- redshifts for all CNTs considered. The highest redshift occurs for the (8,0) tube, which is about 1.0 eV, then decreasing to 0.4 eV for the (10,0) tube and increasing again to 0.7 eV for the (11,0) tube. This result is in contrast with Ref. [140], redshifts of 173 and 92 meV are expected for the (8,0) and (11,0) CNT-H tubes, respectively. However, it is not expected that these scaling laws work well for small-diameter tubes such as the (8,0). Moreover, the (10,0) and the (11,0) tubes belong to different semiconductor CNT families, also making it harder to compare the results between them. It is then fair to say that the proper diameter dependence of the redshift cannot be extracted from the limited set of CNTs calculated in our work. Finally, Fig. 3.24 summarizes our calculated diameter dependence for the transition energies (both in DFT and BSE), exciton binding energies and redshifts.

Finally, we discuss the intensity ratio between the first impurity-related peak (I_-) and the peak associated with the $v_1 \rightarrow c_1$ (I_{11}) transition. Fig 3.25 shows our results

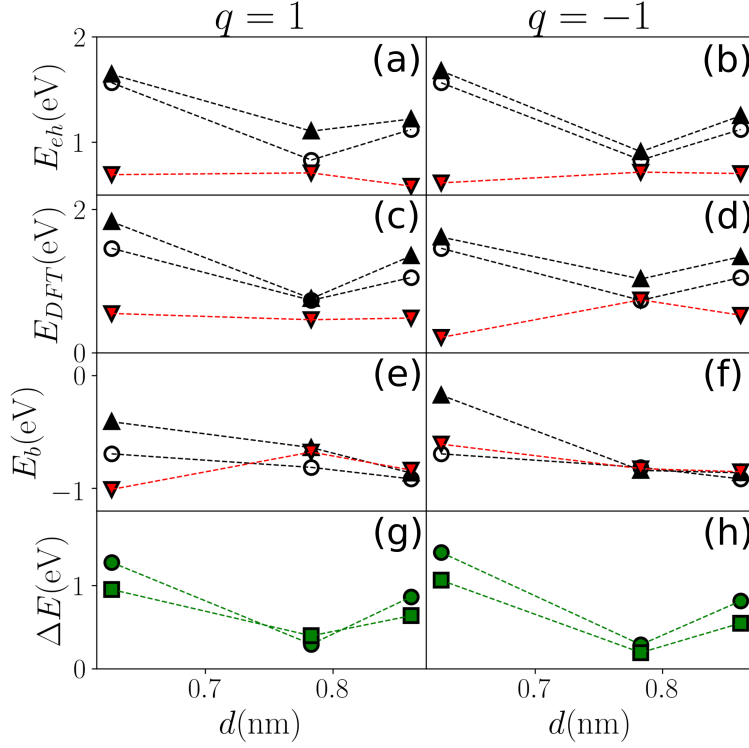


Figure 3.24: Results for (8,0), (10,0) and (11,0) CNTs. (a-d): Peak positions for E_{11} (black symbols) and E_- (red symbols) excitons calculated with BSE (a and b) and at DFT level (c and d). (e-f): Binding energies for E_{11} (black symbols) and E_- excitons (red symbols). (g-h) Redshifts ($|E_- - E_{11}|$) calculated using BSE (squares) and DFT (circles) results. Left (right) panels are results for $q = 1$ ($q = -1$) and black empty circles are results for the E_{11} peaks in pristine CNTs (see table 3.1).

for the intensity ratio in the case of a (10,0) CNT. Apparently, there is a non-monotonic behavior, with a peak for a concentration of $\approx 4 \times 10^{-3}$ of defects per carbon atom, which corresponds to a mean distance between consecutive defects of about 2.5 nm. A similar non-monotonic behavior in the I_- intensity was also seen in Ref. [7] for CNT(6,5) bound to 4-nitrobenzenediazonium tetrafluoroborate. Other experimental data in the supplemental material of Ref. [7] show similar optimal concentrations values for other tubes chirality and defects bound to the CNT.

Experimentally, the ratio I_-/I_{11} is influenced by the exciton population (including decays from dark to bright excitons and vice versa) and electron-phonon interactions [174], so a direct comparison between theory and experiment is not so simple in this case. Our

ab initio results just take in account the dipole moment and eigenvalues of excitons as shown in eq. (2.68). Our explanation for an optimal concentration value for which the E_- intensity is maximized, is that the impurity state has a localization length δ and for low concentration of defects, defects do not interfere with each other. As the defect concentration increases, more localized points of the CNT emit E_- photons, then its peak intensity increases. When the mean distance between defects l is close to the localization size δ (the defect concentration increases), defect states start to interfere with each other and the ratio I_-/I_{11} decreases.

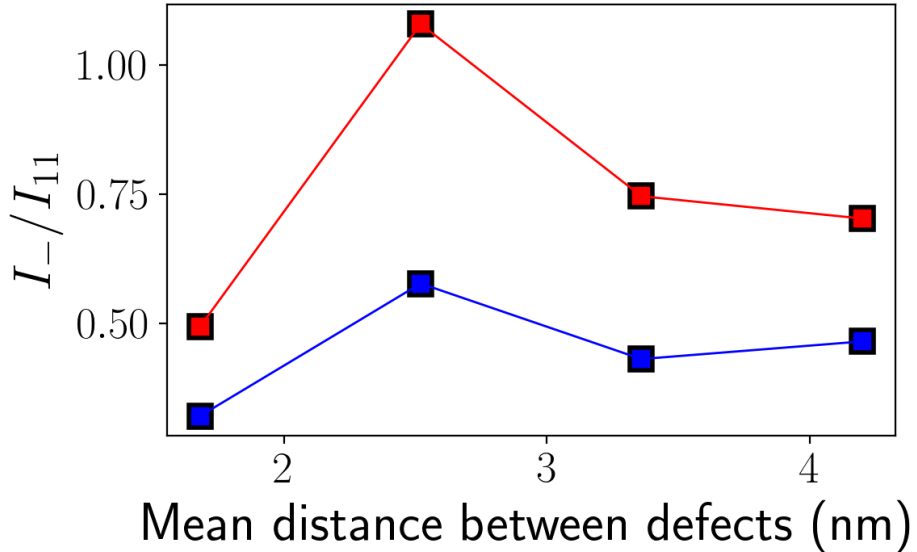


Figure 3.25: Ratio between the intensities of the first redshifted peak and the E_{11} peak calculated using BSE. Red (blue) symbols are calculations for CNT(10,0) bonded to H with net charge $q = 1$ ($q = -1$).

Finally, we analyze the effects of positional disorder on the optical spectra using the TB method. The results are shown in Fig. 3.26, where we plot the optical absorption for various H concentrations. Although these calculations obviously miss the excitonic effects, several interesting effects are seen. First of all, for concentrations smaller than 1 defect/nm, impurity-related optical transitions are not so visible, but a small shoulder appears to the higher-energy side of the main E_{11} transition. We attribute this shoulder

to the symmetry-breaking induced by the defects, which lifts the double-degeneracy of valence and conduction bands. For larger concentrations, a peak at nearly half the E_{11} energy appears. This peak is related to transitions to/from the defect state and increases in intensity as the defect concentration increases. We also notice a gradual blueshift of E_{11} transitions, likely induced by quantum confinement effects of the valence and conduction band edge states.

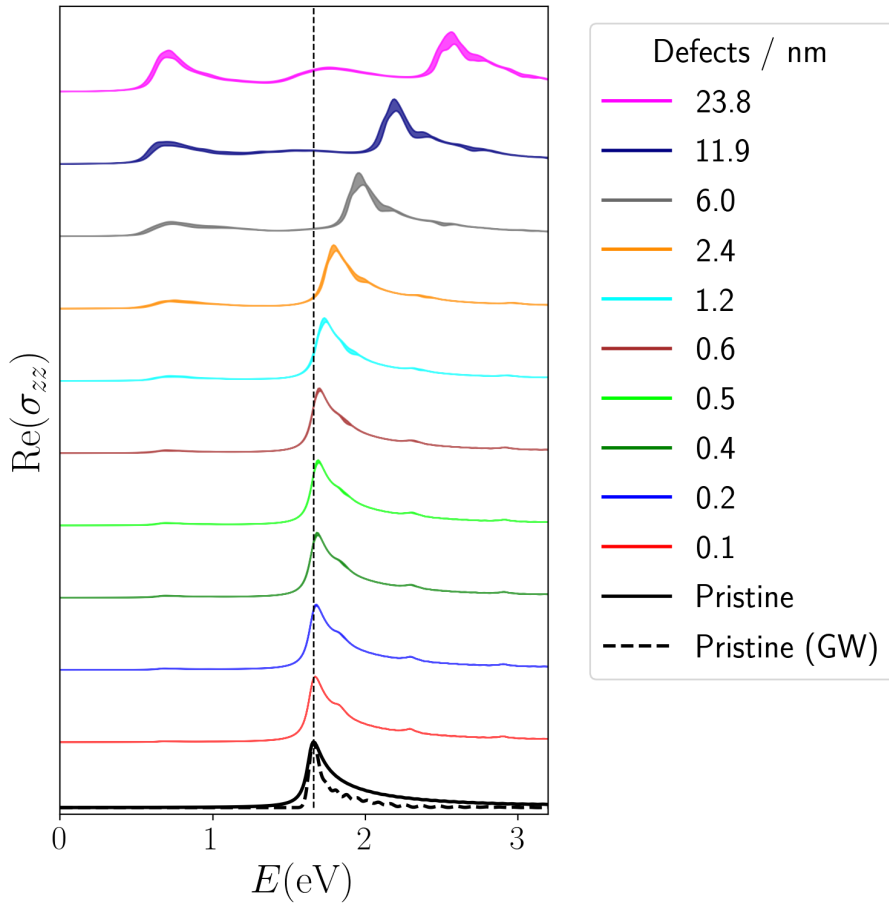


Figure 3.26: Absorption spectra calculated at TB level (except the black dashed line, which was calculated at GW level without e-h interaction) for several defects concentrations. In each curve, the linewidth is twice the standard deviation of the samples. The sample size for each case is 20.

3.5 Exciton Symmetries and Selection Rules

In the literature, the redshifted peak is often associated to dark excitons that become bright due to the symmetry breaking caused by the defects [7]. In this section we investigate this possibility.

In Fig. 3.27 we plot the all eigenvalues of the BSE identifying which are bright or dark excitons. For pristine CNT(10,0) the two degenerated valence and conduction bands give rise to four excitons, one is bright, and the other three are dark excitons, as predicted by group theory [3, 59] (see explanation in section 1.3). Those four states are located at about 0.8 eV and other higher-energy dark excitons appear near 1.2 eV. For CNT(10,0)-H, several degeneracies are broken and we observed a much richer set of dark and brighter excitons (see Fig. 3.27), for all cases of charge doping and defect concentration.

The same trend is observed for CNT(11,0)-H and for CNT(8,0)-H, as shown in Fig. 3.28. In particular, for pristine CNT(8,0), we see an anomalous behavior associated to small-diameter CNTs: The E_{11} exciton energy is 1.56eV and we observed dark excitons with energy close to 1.2eV, as this bright exciton is composed by the first valence band and the fourth conduction band, differently from large-diameter tubes such as the (10,0) and (11,0) CNTs where the first exciton is composed by the first conduction and first valence bands. For CNT(8,0)-H we also observe deeper transitions with energy 0.8 eV smaller than the lowest dark exciton of CNT(8,0).

As one can see, several bright excitons can be seen with energy lower than E_{11} . To determine whether these excitons correspond to brightening of originally dark excitons associated to $v_1 \rightarrow c_1$ transitions, we analyzed the valence-conduction band compositions of all low-energy exciton states in our calculations. Each exciton is composed of a linear combination of several transitions. We say that an exciton is composed by a transition $v_i \rightarrow c_j$ if this transition corresponds to 50% or more of the exciton composition. We consider an exciton bright if its dipole moment intensity is 5% or more of the dipole

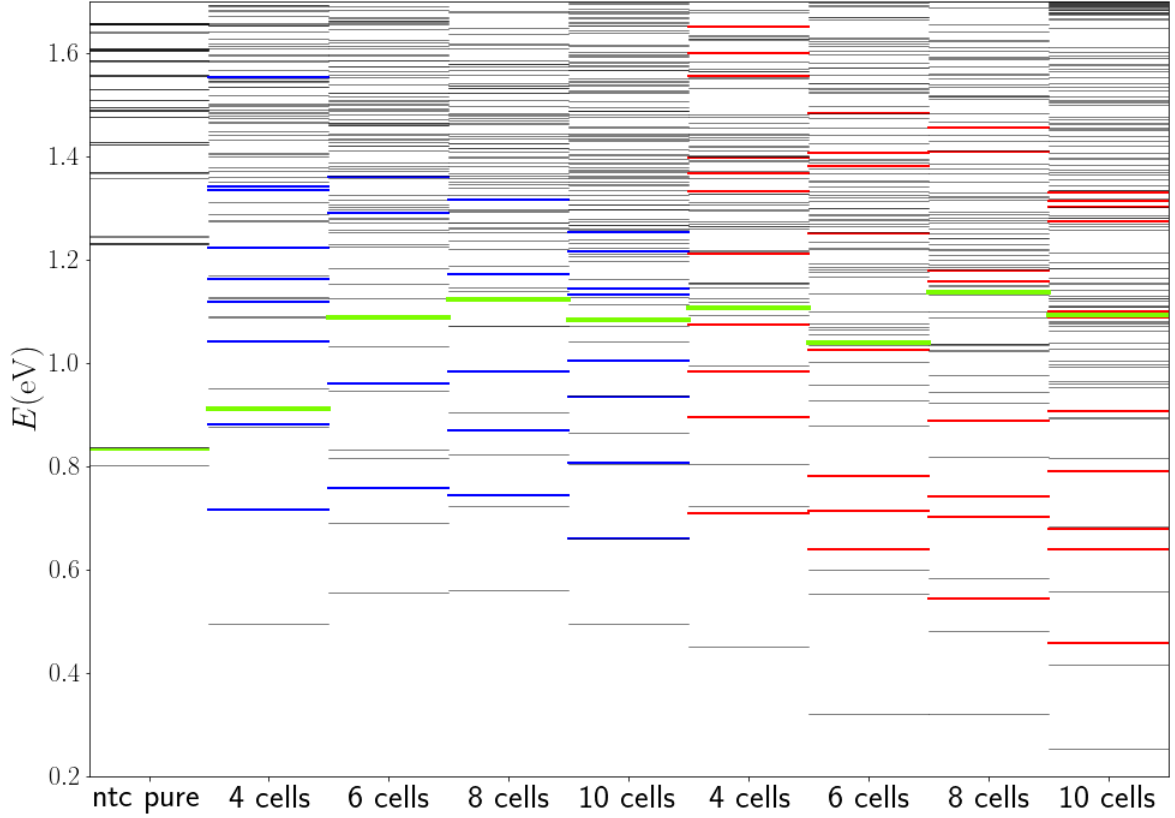


Figure 3.27: Dark (black lines) and bright excitons (colored lines) for CNT bonded with hydrogen atom for different number of unit cells included in calculations. Green lines are the E_{11} excitons for each case and blue (red) lines are bright excitons for calculations with $q = -1$ ($q = 1$). Calculations were done for pristine CNT and supercells with 4, 6, 8 and 10 unit cells (indicated in the figure).

moment intensity of the highest absorption peak.

We focus our analysis on the CNT(10,0)-H. Our results are shown in Fig. 3.29 (for $q = 1$) and Fig. 3.30 (for $q = -1$). The four large panels in each figure correspond to different defect concentrations (or supercell sizes). Each large panel is composed of upper and lower smaller panels. The upper panels show the optical absorption and the lower panel show the main component of the excitonic transitions. We focus specifically on the $v_1 \rightarrow c_1$ transitions (which include $1 \rightarrow 1$, $1' \rightarrow 1$, $1 \rightarrow 1'$, and $1' \rightarrow 1'$, all related to the E_{11} exciton in pristine CNT(10,0)), and on the impurity-related $v_{1'} \rightarrow i$ ($i \rightarrow c_{1'}$) transition, observed for calculations with charge $q = 1$ ($q = -1$), where the

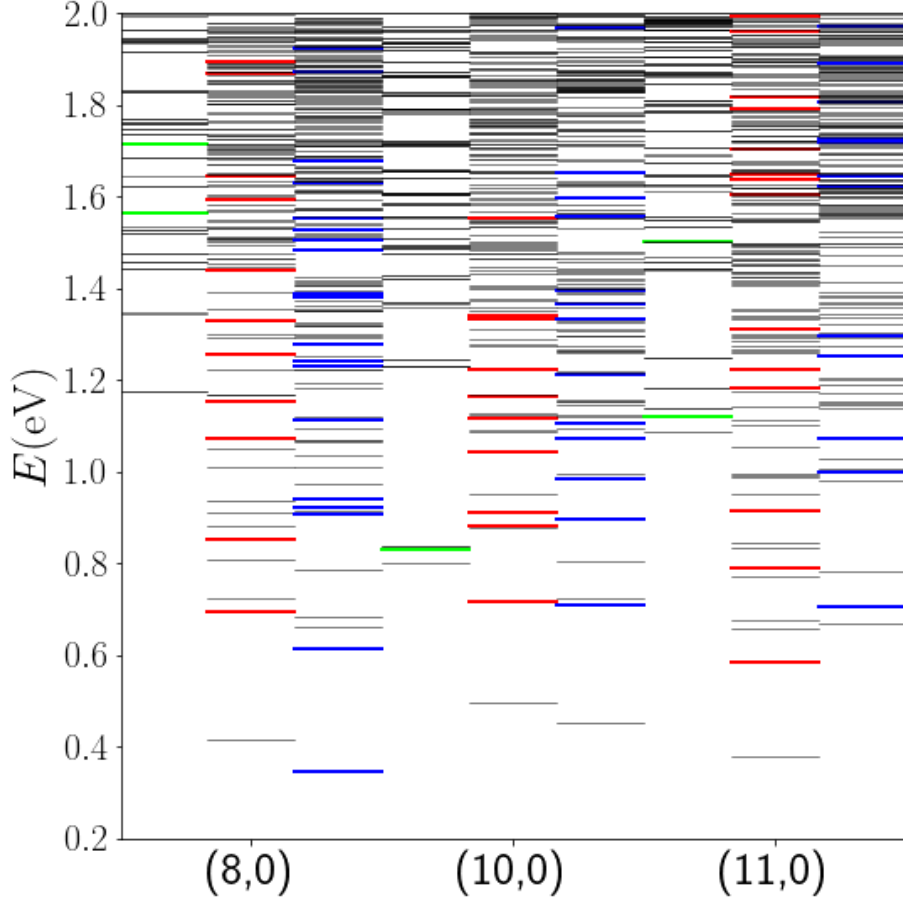


Figure 3.28: Dark (black lines) and bright excitons for CNT bonded with hydrogen atom for different diameters. Green, red and blue lines are bright excitons for the cases of pristine tube, CNT-H with $q = 1$ and CNT-H with $q = -1$, respectively.

impurity band is completely empty (full). Our results show unequivocally that not only the lowest-energy redshifted E_- peak but all the bright exciton peaks below E_{11} are mainly composed of optical transitions involving the defect state. Therefore, they do not correspond to brightening of previously dark exciton states. As a matter of fact, these would be the $v_{1'} \rightarrow c_{1'}$ excitons, which have actually much smaller intensities than the E_{11} peak and they generally have energies larger than E_{11} in all cases considered.

These results can be understood in more detail by performing a group-theory analysis of exciton states. Pristine CNT($n, 0$) belongs to the D_{2nh} point group symmetry and its valence (conduction) band belongs to the $E_{\bar{\mu}g}$ ($E_{\bar{\mu}u}$) representations, which are two-

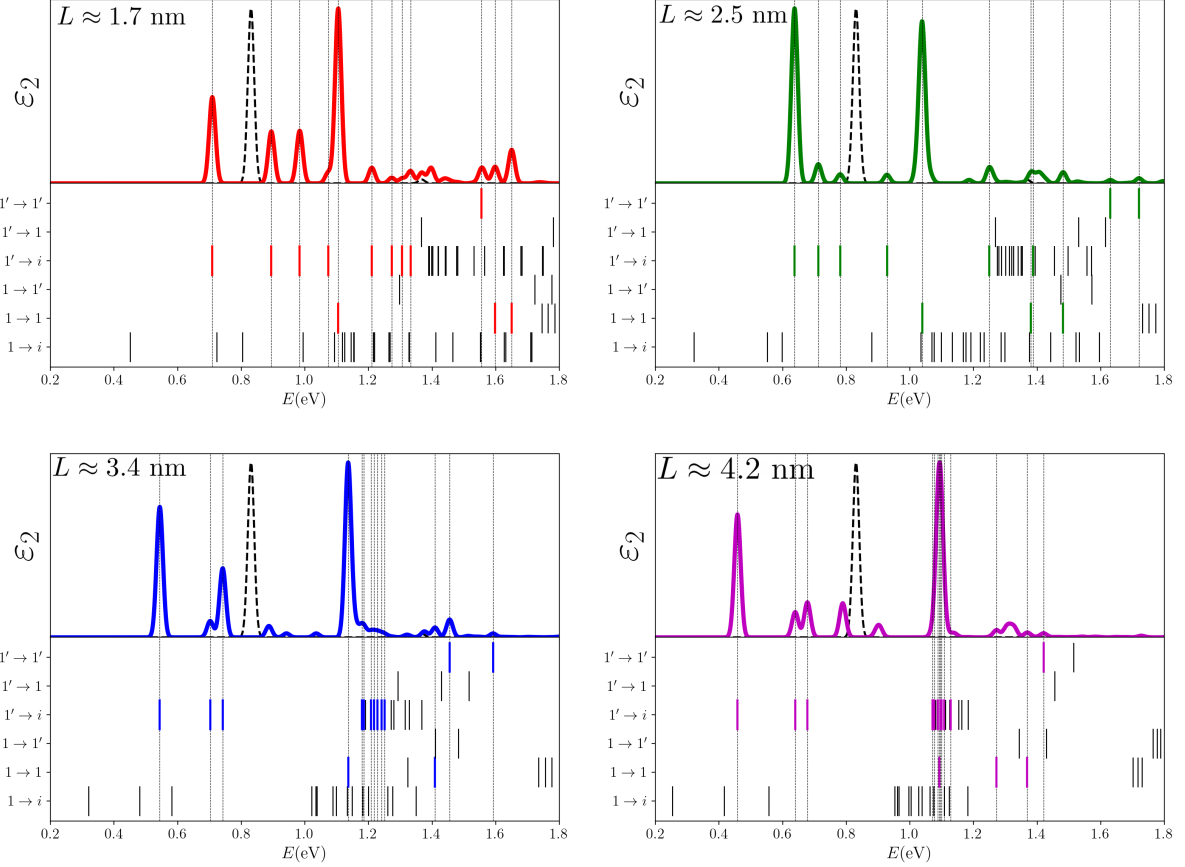


Figure 3.29: Optical absorption at BSE level (upper panel) and exciton composition (lower panel) for different number of unit cells for CNT(10,0)-H with $q = 1$. In the lower panels the bright (dark) excitons are colored (dark) vertical lines. Bright excitons are associated to absorption peaks by vertical dashed lines. In the upper panel black dashed line is the optical absorption of pristine CNT(10,0).

dimensional and the envelope function $F_\nu(r)$ belongs to A_{1g} (A_{2u}) for $\nu = \text{even number}$ ($\nu = \text{odd number}$), as explained in section 1.3.3. Evaluating the direct product with the valence band, the conduction band and envelope function representations, we get

$$\begin{aligned} E_{\tilde{\mu}g} \otimes E_{\tilde{\mu}u} \otimes A_{1g} &= A_{1u} + A_{2u} + E_{\tilde{\mu}'u} (\nu = \text{even}) \\ E_{\tilde{\mu}g} \otimes E_{\tilde{\mu}u} \otimes A_{2u} &= A_{2g} + A_{1g} + E_{\tilde{\mu}'g} (\nu = \text{odd}) \end{aligned} \quad (3.4)$$

which means that for CNT(10,0) the $E_{\tilde{\mu}'g}$ and $E_{\tilde{\mu}'u}$ bands give rise to four excitons: two non degenerate and two degenerate. Bright excitons (A_{2u}) appear for $\nu = \text{even}$ and the other cases are dark excitons.

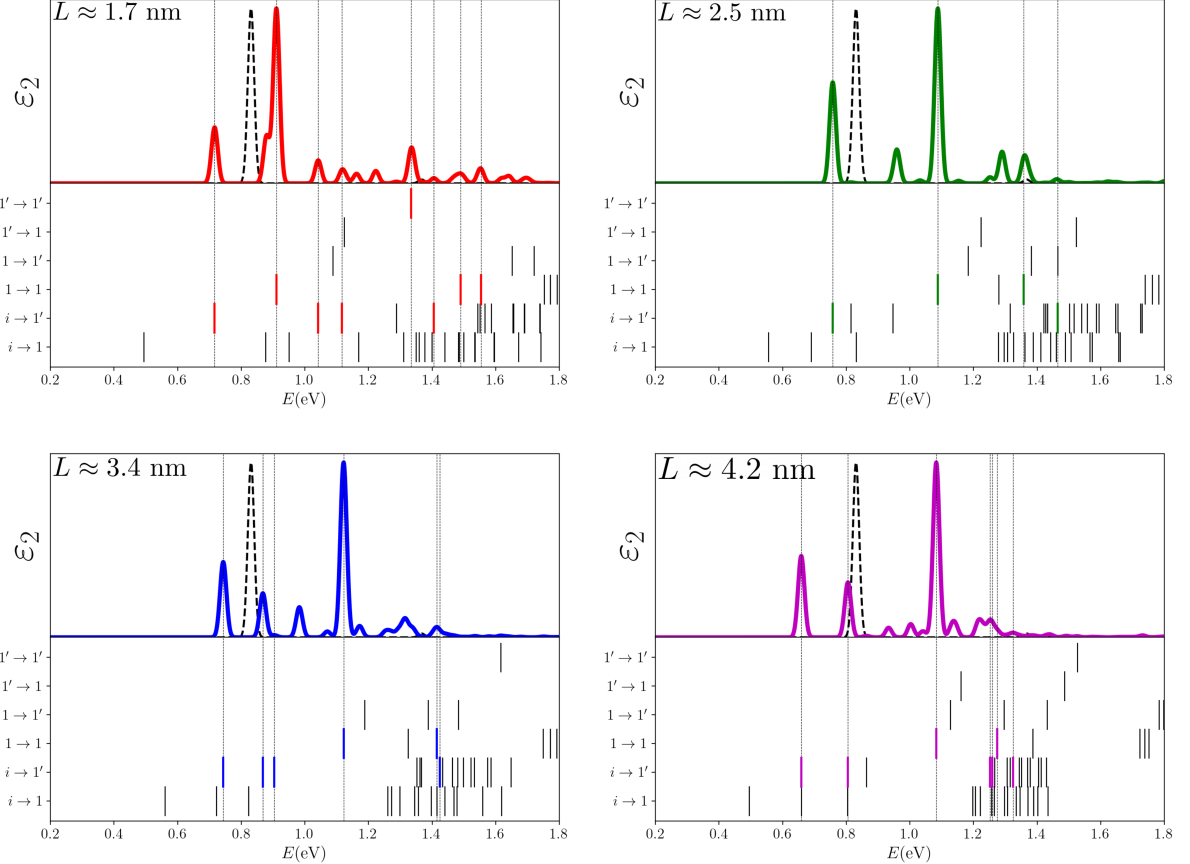


Figure 3.30: Optical absorption at BSE level (upper panel) and exciton composition (lower panel) for different number of unit cells for CNT(10,0)-H with $q=-1$. In the lower panels the bright (dark) excitons are colored (dark) vertical lines. Bright excitons are associated to absorption peaks by vertical dashed lines. In the upper panel black dashed line is the optical absorption of pristine CNT(10,0).

The introduction of the hydrogen atom breaks the CNT symmetry, changing the point group from D_{2nh} to C_s , in which the symmetries are the identity and horizontal plane reflection (a plane that contains the nanotube axis and the hydrogen atom) operations. To analyze the effect of the symmetry breaking, the compatibility relations in table 3.3 are necessary.

By using the compatibility relations, the direct product from eq. 3.4 becomes

$$(A' + A'') \otimes (A' + A'') \otimes A' = 2A' + 2A'' (\nu = \text{even or odd}) \quad (3.5)$$

D_{2nh}	C_s
$E_{\tilde{\mu}u}$	$A' + A''$
$E_{\tilde{\mu}g}$	$A' + A''$
$A_{1g}, B_{2g}, A_{2u}, B_{1u}$	A'
$A_{2g}, B_{1g}, A_{1u}, B_{2u}$	A''

Table 3.3: Compatibility relations

where the representation of the envelope function F_ν is A' for both ν even or odd.

The A' (A'') excitons are bright (dark) excitons, where the A' exciton comes from the direct product between equal representations ($A' \otimes A'$ and $A'' \otimes A''$) and the A'' exciton comes from different representations ($A' \otimes A''$). This group theory analysis agrees with our *ab initio* results: the A' excitons corresponds to $v_1 \rightarrow c_1$ (bright, high intensity) and $v_{1'} \rightarrow c_{1'}$ (bright, low intensity) transitions and A'' excitons corresponds to $v_1 \rightarrow c_1$ and $v_1 \rightarrow c_{1'}$ dark excitons.

By looking at the electronic density of those wavevectors ($\rho = |\psi|^2$), we observed that for v_1 , $v_{1'}$, c_1 and $c_{1'}$ (see Fig. ??) the electronic density has 6 nodes in the angular direction. For v_1 and c_1 ($v_{1'}$ and $c_{1'}$) bands there is a maximum (node) at $\theta = 0$. In other words, v_1 and c_1 states transform like A' (even under the horizontal reflexion), whereas $v_{1'}$ and $c_{1'}$ transform like A'' (odd under reflexion). So, we concluded that v_1 and c_1 ($v_{1'}$ and $c_{1'}$) wavefunctions are in phase and v_1 and $c_{1'}$ ($v_{1'}$ and c_1) wavefunctions are out of phase, with respect the oscillations around the CNT circumference. The dipole moment parallel to the tube axis is proportional to $\langle \psi_c | v_z | \psi_v \rangle$ and if we write the eigenfunctions as $|\psi_{c(v)}\rangle = Z_{c(v)}(z)\Theta_{c(v)}(\theta)$, the dipole moment is given by

$$\langle \psi_c | v_z | \psi_v \rangle = \int dz Z_c^* v_z Z_v \int d\theta \Theta_c^* \Theta_v \quad (3.6)$$

then if Θ_c and Θ_v are out of phase the integral in θ will be zero and the corresponding exciton is dark.

Now, by looking at the impurity state, our *ab initio* results show that the impurity state is also even under reflexion (A' symmetry) and therefore it couples with the v_1 (c_1)

band for $q = 1$ ($q = -1$) and does not couple with $v_{1'}$ or $c_{1'}$.

Another consequence of the symmetry breaking of is that the quasi-angular momentum $\tilde{\mu}$ do not have influence on selection rules anymore. As $\tilde{\mu}$ is not a good quantum number anymore, new excitons may arise for transitions between bands of different $\tilde{\mu}$ indices.

For light polarization perpendicular to the tube axis, excitons are composed by bands where $\delta\mu = \mu - \mu' = \pm 1$ [3, 59] in pristine CNTs. The introduction of the H defect also changes selection rules following the above explanation, although our BSE results for light polarization perpendicular to the tube axis show peaks with much smaller intensities.

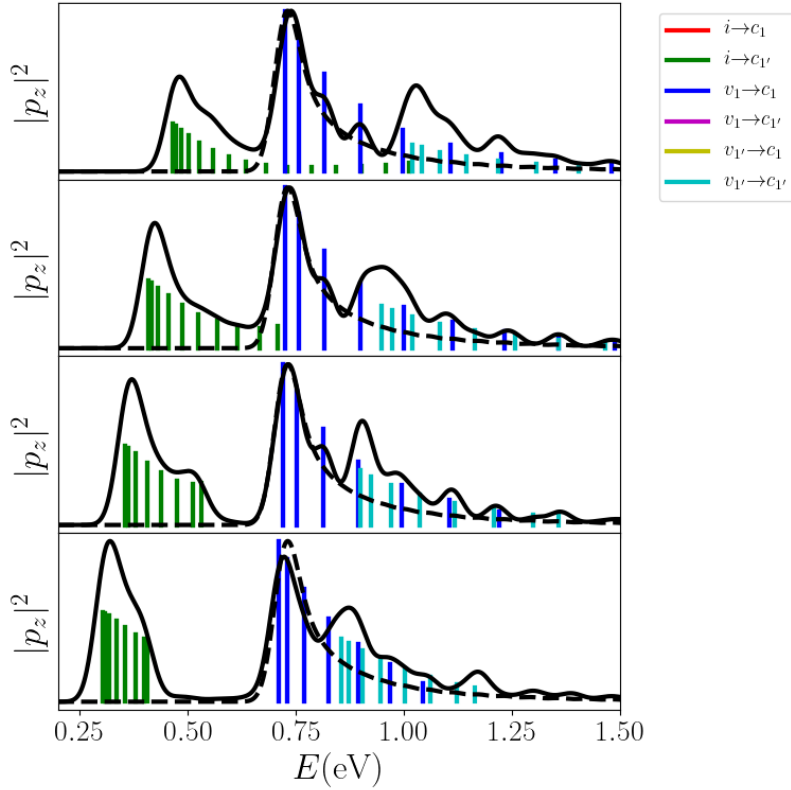


Figure 3.31: Absolute value of dipole transition matrix elements for different transitions evaluated at DFT level for negatively charged ($q = -1$) CNT(10,0)-H for several tube lengths. Black (continuous) dashed lines are optical absorptions evaluated at DFT level for CNT(10,0)-H (pristine CNT(10,0)). From the top to the bottom the unit cell length is: 1.7nm, 2.5nm, 3.4nm and 4.2nm.

Symmetry aspects and selection rules can also be used to analyse the optical spectra at the DFT level. We now focus on the CNT(10,0)-H system. Fig. 3.31 show the optical

spectra at the DFT level with $q = -1$ (where the impurity band is totally filled), for several defect concentrations. Notice that we observe the same symmetry combinations that compose bright excitons at BSE level calculations with $q = -1$ (Fig. 3.30). Similar trends are observed for DFT with $q = 1$ (not shown). At DFT level the transition $v_1 \rightarrow c_1$ (in blue) has energy equal to the CNT bandgap and the transitions $i \rightarrow c_{1'}$ (in green) are redshifted with respect to the $v_1 \rightarrow c_1$ transition. The transition $v_{1'} \rightarrow c_{1'}$ is blueshifted with respect to the $v_1 \rightarrow c_1$, similar to what happens in the BSE case. As the number of unit cells increase, the $v_{1'} \rightarrow c_{1'}$ peak gets closer to the $v_1 \rightarrow c_1$ peak as the splits Δ_v and Δ_c are proportional to N_{cells}^{-1} .

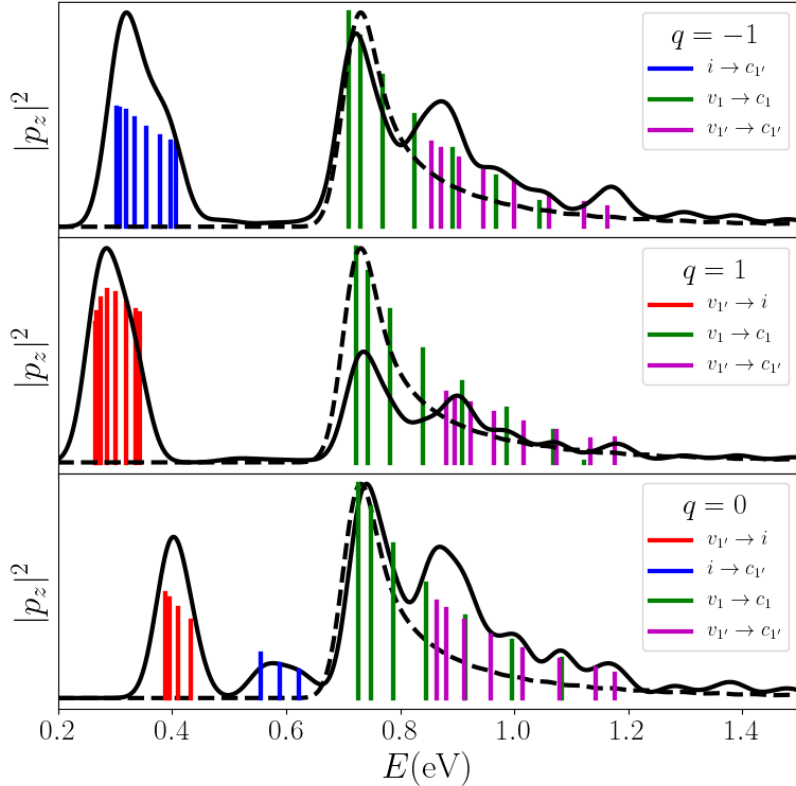


Figure 3.32: Absolute value of dipole transition matrix elements for different transitions evaluated at DFT level for CNT(10,0)-H with unit cell length 4.2 nm with $q = 0, \pm 1$ (indicated in each panel).. Black (continuous) dashed lines are optical absorptions evaluated at DFT level for CNT(10,0)-H (pristine CNT(10,0))

In Fig. 3.32 we show the same analysis for various charge states, using our largest

supercell size (4.2 nm). For $q = -1$ ($q = 1$) the redshifted peaks are transitions $i \rightarrow c_1'$ ($v_1' \rightarrow i$) and in the specific case of $q = 0$ we see both transitions as the impurity band is half filled ⁵.

Those transitions are easily explained if one applies group theory neglecting excitonic effects. In this case, the direct product to be considered involves just the valence and conduction bands (does not include the envelope function) [3,59]. The results are the same as in eq. 3.5 as the envelope function belongs to the totally symmetric representation. This may be a very useful approach when studying systems that are very computationally demanding for GW/BSE calculations but possible to study at DFT, TB or other electronic structure methods.

We now go back to the symmetry analysis of the excitonic states and consider the (8,0) and (11,0) CNTs. For CNT(8,0) the analysis is more complicated, as this is a relatively small-diameter CNT and some of its features do not follow the same trends of larger diameter tubes. For the pristine tube (left panel of Fig. 3.33), the first and second valence bands are double degenerated, the first conduction band is non degenerate and the second, third and fourth conduction bands are each one double degenerate. The E_{11} transition couples the v_1 and v_1' with c_4 and c_4' bands and the E_{22} absorption peak, which is blueshifted about 100meV with respect to E_{11} , couples the v_2 and v_2' with c_3 and c_3' bands. This band inversions with respect to larger diameter CNTs results primarily from trigonal warping effects in the graphene band structure.

For CNT(8,0)-H with $q = +1$ (middle panel of Fig. 3.33), first we observe many peaks with the transition from v_1' to the impurity state i in a non-Rydberg series. We also observe less intense peaks, including transitions from v_2' to i . We still observe the E_{11} peak, now composed just by the v_1 and c_4 bands and the E_{22} peak, now composed by v_2 and c_3 bands. Other transitions that were not present in pristine CNT(8,0) are now

⁵It is important to note that we can only study the $q = 0$ case at DFT level because Many Perturbation Methods are not easily applicable to open shell systems [175]

present in CNT(8,0)-H, such as $v_{2'}$ to c_1 , $v_{1'}$ to c_2 , $v_{1'}$ to c_1 and v_1 to $c_{2'}$.

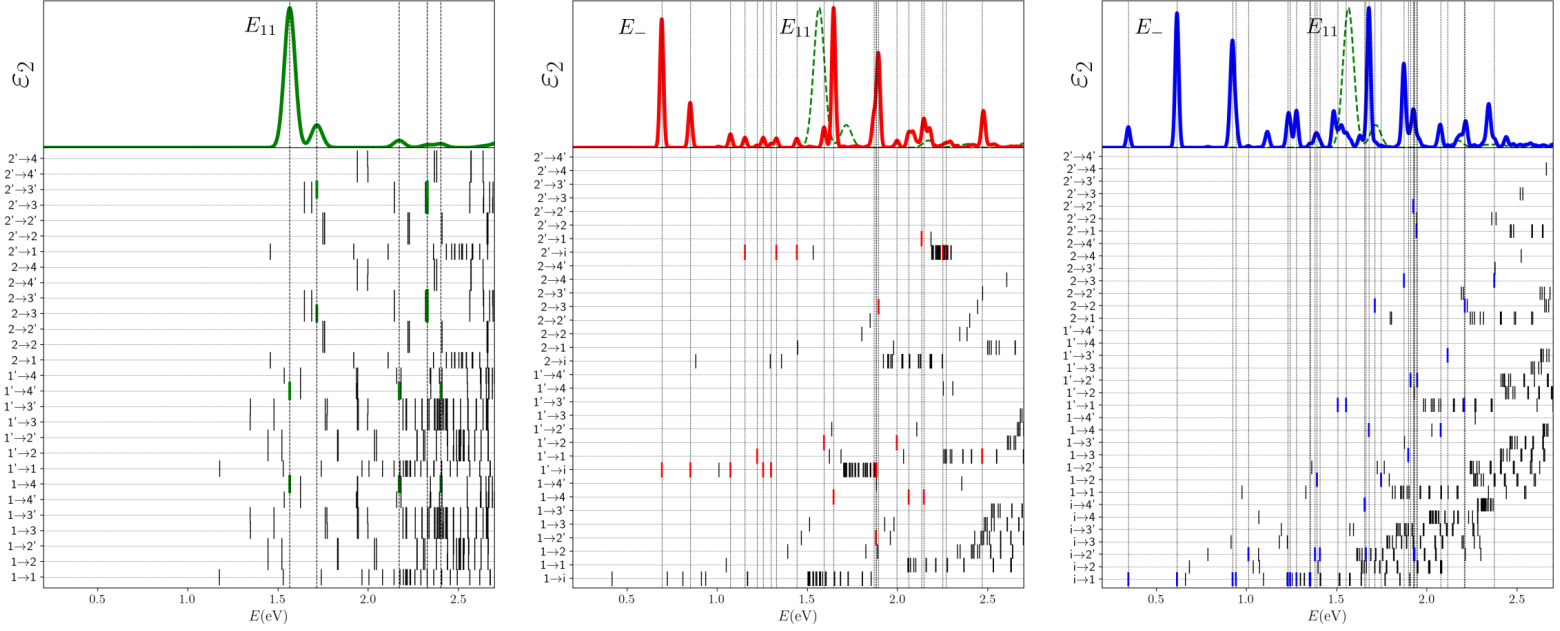
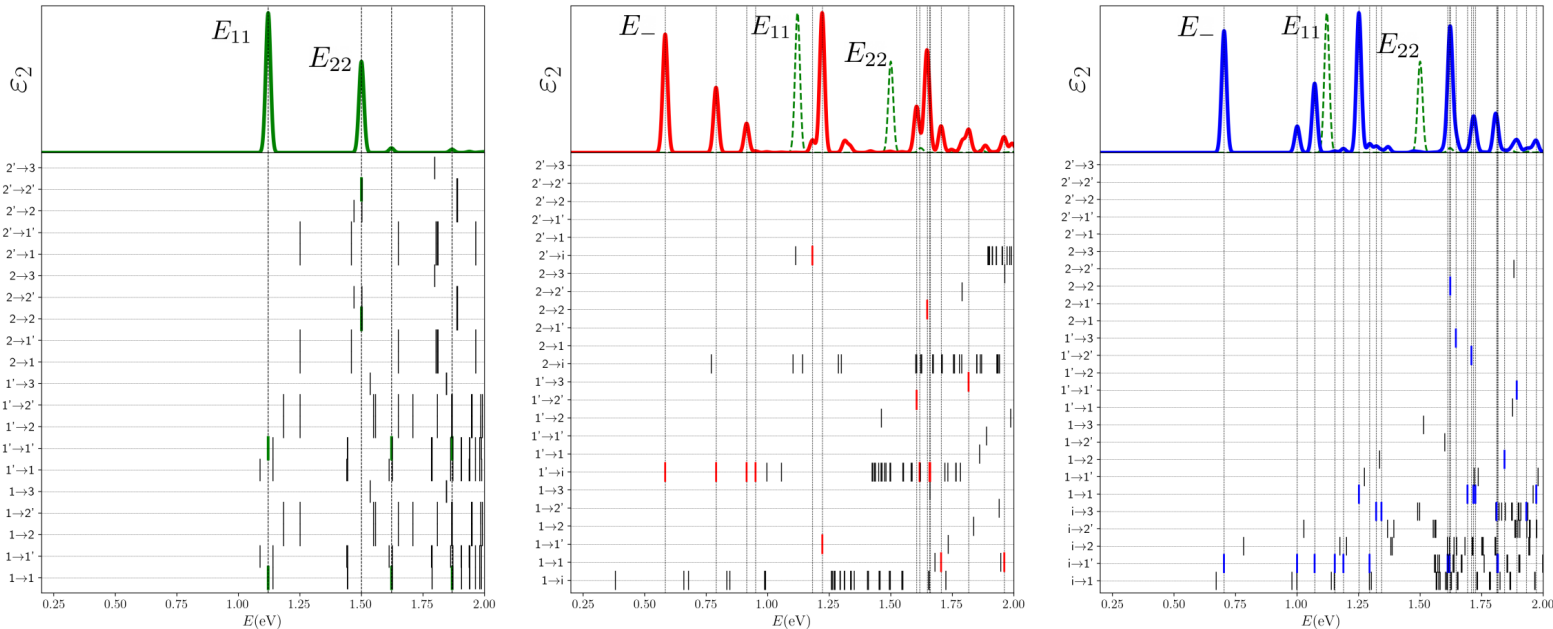


Figure 3.33: Optical absorption at BSE level (upper panel) and exciton composition (lower panel) for pristine CNT(8,0) (left) and CNT(8,0)-H with $q = 1$ (middle) and $q = -1$ (right), where the concentration of defects is 0.6 defect/nm. In the lower panels the bright (dark) excitons are colored (dark) vertical lines. Bright excitons are associated to absorption peaks by vertical dashed lines. In the upper panels (b) and (c) green dashed line is the optical absorption of pristine CNT(8,0).

Finally, the results for CNT(8,0)-H with $q = -1$ are shown in the right panel of Fig. 3.33. The first two peaks involve the transition i to c_1 , with the first peak being less intense than the second one. The transition from i to $c_{2'}$ is also present. The E_{11} and E_{22} peaks are present as in case of CNT(8,0)-H $q = 1$. Other transitions that are not present in the pristine CNT(8,0) are now present for the defective case and they are summarized in Table 3.4.

We now address the CNT(11,0). As other larger-diameter tubes, the first and second valence (conduction) bands are double degenerate and the third conduction band is non-degenerate. Therefore, the E_{11} (E_{22}) exciton couples v_1 and $v_{1'}$ (v_2 and $v_{2'}$) with c_1 and $c_{1'}$ (c_2 and $c_{2'}$) in the pristine case, as shown in the left panel of Fig. 3.34. For CNT(11,0)-H with $q = \pm 1$ (middle panel) the E_{11} (E_{22}) peak is composed of the v_1 and c_1 (v_2 and c_2)

CNT(8,0)	CNT(8,0)-H ($q = +1$)	CNT(8,0)-H ($q = -1$)
$(v_1, v_{1'}, c_4, c_{4'}) (E_{11})$	$(v_1, c_4) (E_{11})$	$(v_1, c_4) (E_{11})$
$(v_2, v_{2'}, c_3, c_{3'}) (E_{22})$	$(v_2, c_3) (E_{22})$	$(v_2, c_3) (E_{22})$
	$(v_{1'}, i) (E_-)$	$(i, c_1) (E_-)$
	$(v_{2'}, i)$	$(i, c_{2'})$
	$(v_{1'}, c_1)$	$(v_{1'}, c_1)$
	$(v_{1'}, c_2)$	$(v_{2'}, c_{2'})$
	$(v_{2'}, c_1)$	$(v_{2'}, c_1)$
	$(v_1, c_{2'})$	(v_1, c_2)

Table 3.4: Bright exciton compositions for CNT(8,0) and CNT(8,0)-H ($q = \pm 1$)Figure 3.34: Optical absorption at BSE level (upper panel) and exciton composition (lower panel) for pristine CNT(11,0) (left) and CNT(11,0)-H with $q = 1$ (middle) and $q = -1$ (right), where the concentration of defects is 0.6 defect/nm. In the lower panels the bright (dark) excitons are colored (dark) vertical lines. Bright excitons are associated to absorption peaks by vertical dashed lines. In the upper panels (b) e (c) green dashed line is the optical absorption of pristine CNT(11,0).

bands. For $q = 1$ ($q = -1$, left panel) the E_- peak is the transition from $v_{1'}$ to i (i to $c_{1'}$). Other transitions are listed in Table 3.5.

In summary, the presence of the defect breaks the zigzag CNT symmetry from D_{2nh} to C_s and $\tilde{\mu}$ is not a good quantum number anymore. Double degenerate bands become two non-degenerate bands that we call c_a and $c_{a'}$ (v_a and $v_{a'}$) and E_- peaks are related

CNT(11,0)	CNT(11,0)-H ($q = +1$)	CNT(11,0)-H ($q = -1$)
$(v_1, v_{1'}, c_1, c_{1'}) (E_{11})$	$(v_1, c_{1'}) (E_{11})$	$(v_1, c_1) (E_{11})$
$(v_2, v_{2'}, c_2, c_{2'}) (E_{22})$	$(v_2, c_2) (E_{22})$	$(v_2, c_2) (E_{22})$
	$(v_{1'}, i) (E_-)$	$(i, c_{1'}) (E_-)$
	$(v_{2'}, i)$	(i, c_3)
	$(v_{1'}, c_{1'})$	$(v_{1'}, c_{1'})$
	$(v_{1'}, c_{2'})$	$(v_{1'}, c_{2'})$
	$(v_{1'}, c_3)$	$(v_{1'}, c_3)$
	$(v_{2'}, c_{1'})$	$(v_{2'}, c_{1'})$
		$(v_{2'}, c_{2'})$

Table 3.5: Bright exciton compositions for CNT(11,0) and CNT(11,0)-H ($q=\pm 1$)

to the coupling between the impurity state i and $c_{a'}$ ($v_{a'}$) states. In the C_s point group there is only two possible representations, A' and A'' , and equal representations couple with each other. The previous 1 bright and 3 dark excitons become 2 dark (coupling c_a with $v_{a'}$ and $c_{a'}$ with v_a) and 2 bright excitons (coupling c_a with v_a and $c_{a'}$ with $v_{a'}$). The impurity gives rise to new bright (coupling the impurity band with $v_{a'}$ and $c_{a'}$) and dark (coupling the impurity band with v_a and c_a) excitons, and to those cases we attribute the redshifted peaks observed experimentally.

Another variable to be explored is the spatial arrangement of defects on the tube surface. For example, in the ref. [133], CNT(8,0) bonded to two hydrogen atoms was studied and in this case the impurity states did not lie in the middle of the band gap, but resonant within the conduction and valence bands. The second hydrogen atom was bonded in the ortho position (see Fig. 3.35) and the line connecting the carbon atoms bonded to those hydrogen atoms is parallel to the tube axis, so the point group in this case is C_{2v} (the same of water molecule), which has four representations: A_1 , A_2 , B_1 and B_2 . For this symmetry the representations $E_{\tilde{\mu}g}$ and $E_{\tilde{\mu}u}$ both reduce to $B_1 + B_2$ if $\tilde{\mu}$ is odd or $A_1 + A_2$ if $\tilde{\mu}$ is even and the envelope function goes to A_1 independently of $\tilde{\mu}$. Bright excitons just appear in the couplings of bands of same representation (A_1 with A_1 , A_2 with A_2 and so on), then in this case there are less possible transitions. If the second hydrogen is in a meta positions and, the line connecting the carbon atoms bonded

to those hydrogen atoms is not parallel to the tube axis then the point group is C_s , with lower symmetry than C_{2v} . In table 3.6 we show the possible point groups for different possible geometries for CNT-2H.

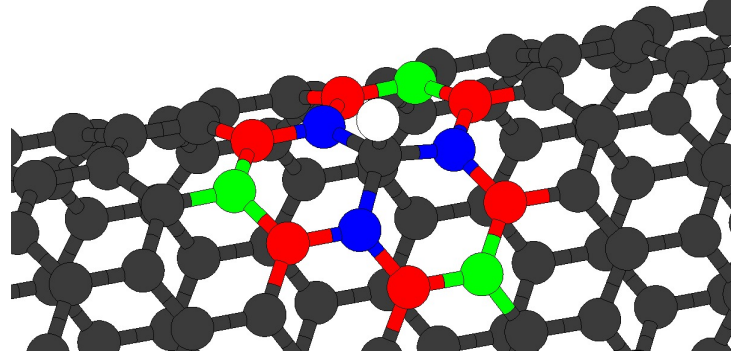


Figure 3.35: Example of possible sites where a second hydrogen atom can be bound. Blue, red and green positions corresponds to orto, meta and para positions respectively. The blue atom on the right and green atom on the left correspond to the C_{2v} point group symmetry and other configurations correspond to C_s point group.

Other defect distributions have different symmetries. Ordered patterns of hydrogenated CNTs are energetically favorable [49,178] (instead of random distributions) which leads to more symmetric configurations.

Geometry	Point Group
ortho $\parallel z$	C_{2v}
ortho not $\parallel z$	C_s
meta	C_s
para $\parallel z$	C_{2v}
para not $\parallel z$	C_s

Table 3.6: Point groups for different geometries of zigzag CNTs bonded to two hydrogen atoms. Configurations can be seen in Fig. 3.35.

3.6 Binding Energy

In this section we analyze the binding energies of the E_{11} and E_- excitons for NTC(10,0)-H with different defect concentrations. The binding energy of an exciton is given by $E_b = E_{gap} - E_x$ where E_x is the exciton energy and E_{gap} is the QP gap between the

bands that generate this exciton. In our calculations the lowest E_{11} and E_- excitons are composed by 95 % or more by two bands.

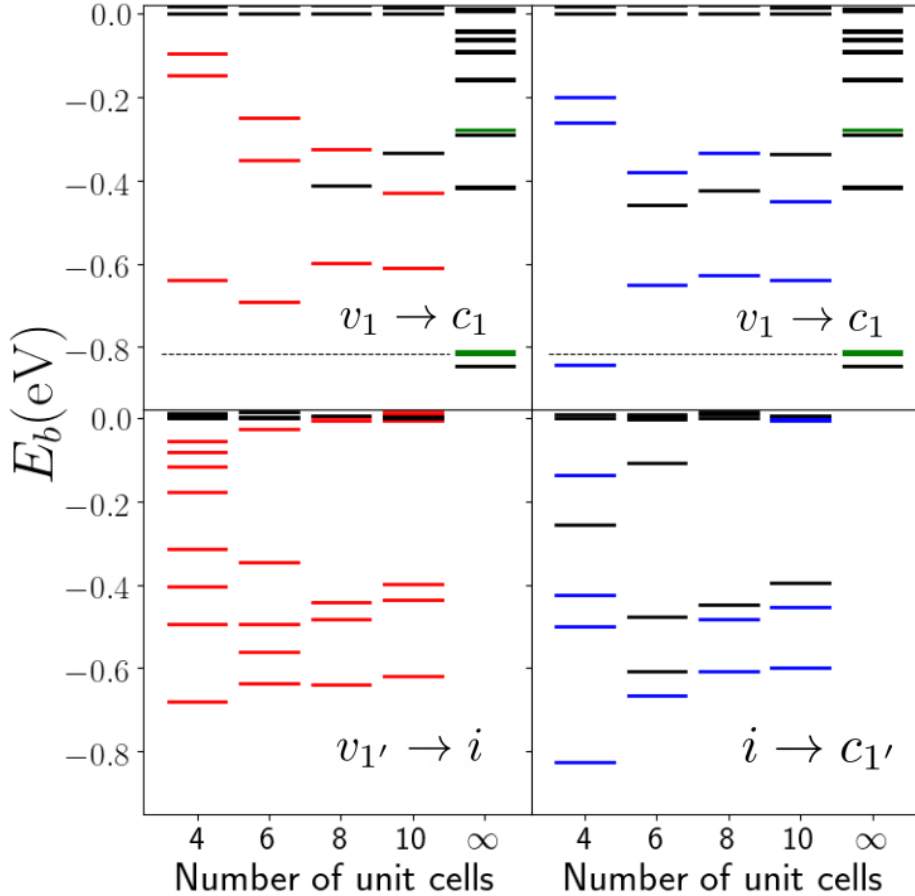


Figure 3.36: Binding energy of different types of excitons in CNT(10,0)-H by varying the number of unit cells in calculations and for $q = 1$ in red (left panels) and for $q = -1$ in blue (right panels). Upper panels are the E_{11} excitons ($v_1 \rightarrow c_1$ transition) and lower panels are the E_- excitons ($v_{1'} \rightarrow i$ transition for $q = 1$ and $i \rightarrow c_{1'}$ transition for $q = -1$). The case for infinity number of unit cells corresponds to pristine CNT(10,0) and black dashed lines is the binding energy for pure CNT(10,0) E_{11} exciton.

We focus on bound excitons, as shown in Fig. 3.36. We observe that the series of binding energies depends on the defect concentration. In general, for higher concentrations we observed higher binding energies, specially for $q = -1$ cases. The binding energies for E_{11} and E_- excitons are similar and for higher concentrations more transitions involving the impurity band appear. For the E_{11} exciton we also show the binding energies for the

pure CNT. The lowest E_{11} exciton is less bound in CNT-H than in the pure CNT case for most defect concentrations, except for four unit cells with charge $q = -1$.

From the effective mass theory (assuming homogeneous screening) those excitons should follow a Rydberg series and the corresponding energies should be [179]

$$E_n = \frac{E_0}{\left(n + \frac{D-3}{2}\right)^2} \quad (3.7)$$

where $D = 1, 2$ or 3 for 1D, 2D and 3D systems respectively. For 1D systems there is a divergence in the equation (3.7) when $n = 1$. So, we propose to fit our data with the following equation

$$E_n = \frac{A}{(n + B)^2} \quad (3.8)$$

where B plays the role of the dimensional parameter.

Comparing the equations 3.7 and 3.8, we should get $B = (1 - 3)/2 = -1$ for 1D systems. In our fits we still observe a behavior $\propto n^{-2}$ and B assumes values 0 to 5 (3 to 10) for the E_- (E_{11}) exciton, as the ground state has a finite binding energy. For low dimensional systems non-Rydberg series are observed [6] as the dielectric screening is not local [68, 180]. In Fig. 3.37 we show that our calculated data show binding energies less intense than what is expected by fits using eq. 3.7. The main reason for that is the non local screening in low dimensional systems [6, 68].

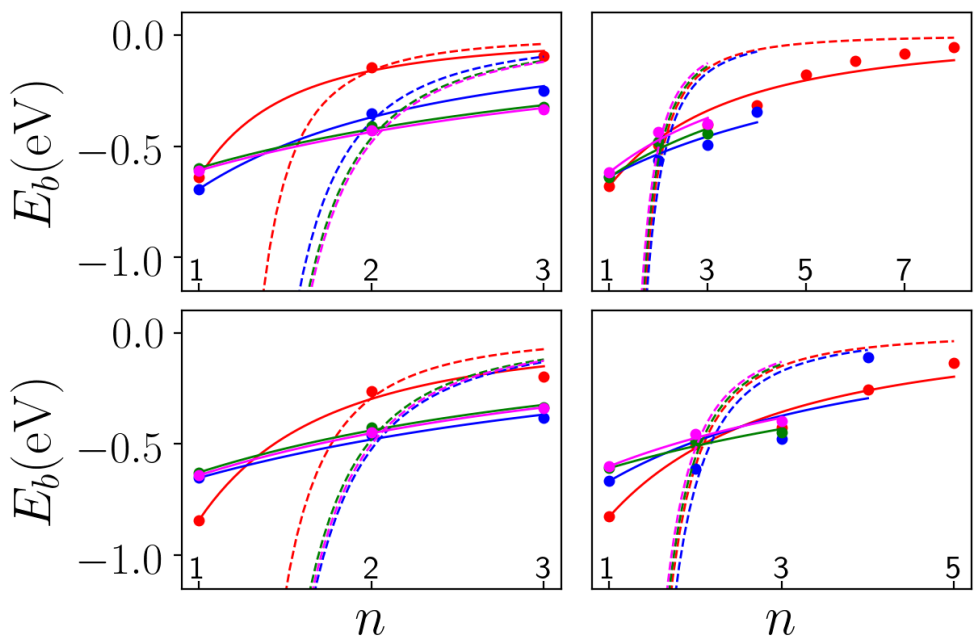


Figure 3.37: Binding energy of excitons E_{11} (upper panels) and E_- (lower panels) for CNT(10,0)-H with $q = 1$ (left panels) and $q = -1$ (right panels). Solid lines are fits using equation 3.8 and dashed lines are fits using equation 3.7 with $D = 1$. Red, blue, green and pink symbols correspond to the cases with 4, 6, 8 and 10 unit cells in the supercell respectively.

Chapter 4

Conclusions

In this work, we analyzed the effect of hydrogen doping in semiconducting zigzag CNTs using *ab initio* and TB calculations. In the electronic structure calculations, we observed the splittings of degenerate bands and the emergence of a flat impurity band in the middle of the bandgap. The band splittings depend on the impurity concentration and electronic doping in CNTs. The wavefunction associated to this impurity band is localized around the defect site. In our TB calculations for different concentrations of random arrangements of hydrogen atoms on the tube surface, we see a distribution of defect states.

In the optical absorption spectra we see new redshifted peaks in agreement with previous theoretical and experimental works. Experimentally, the position of these redshifted peaks highly depend on the withdrawing capability of the covalent defect, the conformational arrangement and concentration of defects. We analyze both the diameter dependence and the defect concentration dependence of the redshift. We also analyzed the different excitons composition, binding energy and lifetimes.

We find out a high variety of bright and dark excitons: some are also present in pristine CNT and some are involve transitions to or from the impurity state. It is important to note that, like in pristine CNTs, the lowest energy state is dark, and the difference between the E_{11} state and the lowest dark state in our results for CNT-H is as large as 600meV,

differently in pristine CNTs where this difference is about 50 meV.

We find that the redshifted peaks are associated to excitons involving the impurity band, and they do not result from brightening of previously dark transitions. We do observe this brightening effect, but it leads to excitons with energies larger than E_{11} and low intensity. As the impurity state is itself localized, the respective exciton must be localized as well, which agrees with experimental works that correlate the E_- emission with specific regions of functionalized CNTs.

By using Group Theory we concluded that the hydrogen breaks the zigzag CNT symmetry from C_{2nv} to the C_s point group (for low concentration of defects) and the impurity band couples to $c_{1'}$ ($v_{1'}$) when the impurity band is totally full (empty). Interestingly, the same trends are observed in calculations at DFT level.

The exciton binding energies do not follow Rydberg series but still show an approximate n^{-2} (the index of each bright exciton) behavior and binding energies for E_{11} excitons are close to binding energies of E_- excitons.

Bibliography

- [1] A. K. Geim and K. S. Novoselov. The rise of graphene. *Nature Materials*, 6(3):183–191, mar 2007. x, 1, 2
- [2] A. H. Castro Neto, F. Guinea, N. M. R. Peres, K. S. Novoselov, and A. K. Geim. The electronic properties of graphene. *Reviews of Modern Physics*, 81(1):109–162, jan 2009. x, 1, 4, 7, 8
- [3] Eduardo B. Barros, Ado Jorio, Georgii G. Samsonidze, Rodrigo B. Capaz, Antônio G. Souza Filho, Josué Mendes Filho, Gene Dresselhaus, and Mildred S. Dresselhaus. Review on the symmetry-related properties of carbon nanotubes. *Physics Reports*, 431(6):261–302, 2006. x, xxi, 3, 4, 5, 6, 8, 10, 11, 12, 18, 19, 81, 87, 89
- [4] Mildred S. Dresselhaus, Gene Dresselhaus, Riichiro Saito, and Ado Jorio. Exciton Photophysics of Carbon Nanotubes. *Annual Review of Physical Chemistry*, 58(1):719–747, 2007. xi, 1, 3, 13, 16
- [5] J. Jiang, R. Saito, Ge G. Samsonidze, A. Jorio, S. G. Chou, G. Dresselhaus, M. S. Dresselhaus, Departamento De Física, Universidade Federal, De Minas Gerais, and Belo Horizonte-mg. Chirality dependence of exciton effects in single-wall carbon nanotubes: Tight-binding model. *Physical Review B - Condensed Matter and Materials Physics*, 75(3):1–13, 2007. xi, 16, 17

- [6] Alexey Chernikov, Timothy C. Berkelbach, Heather M. Hill, Albert Rigos, Yilei Li, Ozgur Burak Aslan, David R. Reichman, Mark S. Hybertsen, and Tony F. Heinz. Exciton binding energy and nonhydrogenic Rydberg series in monolayer WS₂. *Physical Review Letters*, 113(7):1–5, 2014. xi, 16, 17, 95
- [7] Hyejin Kwon, Lyndsey R. Powell, George C. Schatz, Brendan Meany, Nicholas Valley, Yanmei Piao, and YuHuang Wang. Brightening of carbon nanotube photoluminescence through the incorporation of sp₃ defects. *Nature Chemistry*, 5(10):840–845, 2013. xi, 21, 22, 23, 24, 58, 59, 70, 73, 78, 81
- [8] Nicolai F. Hartmann, Sibel Ebru Yalcin, Lyudmyla Adamska, Erik H. Hároz, Xuedan Ma, Sergei Tretiak, Han Htoon, and Stephen K. Doorn. Photoluminescence imaging of solitary dopant sites in covalently doped single-wall carbon nanotubes. *Nanoscale*, 7(48):20521–20530, 2015. xi, 21, 23, 24
- [9] Richard M. Martin. *Electronic Structure*. Cambridge University Press, apr 2004. xii, 32, 39
- [10] STEVEN G. LOUIE. FIRST-PRINCIPLES THEORY OF ELECTRON EXCITATION ENERGIES IN SOLIDS, SURFACES, AND DEFECTS. In *Topics in Computational Materials Science*, pages 96–142. WORLD SCIENTIFIC, feb 1998. xii, 41, 48
- [11] Phaedon Avouris, Zhihong Chen, and Vasili Perebeinos. Carbon-based electronics, oct 2007. 1, 9
- [12] Jean-Christophe Charlier, Xavier Blase, Stephan Roche, Jean-Christophe Charlier, Xavier Blase, and Stephan Roche. Electronic and transport properties of nanotubes. *Rev. Mod. Phys.*, 79(2):677–732, 2007. 1, 6, 7, 32

- [13] Phaedon Avouris, Marcus Freitag, and Vasili Perebeinos. Carbon-nanotube photonics and optoelectronics. *Nature Photonics*, 2(6):341–350, 2008. 1, 13
- [14] A K Geim. Graphene: Status and Prospects. *Science*, 324(5934):1530–1534, jun 2009. 1
- [15] S. Das Sarma, Shaffique Adam, E. H. Hwang, and Enrico Rossi. Electronic transport in two-dimensional graphene. *Reviews of Modern Physics*, 83(2):407–470, may 2011. 1
- [16] Daniel R. Cooper, Benjamin D’Anjou, Nageswara Ghattamaneni, Benjamin Harack, Michael Hilke, Alexandre Horth, Norberto Majlis, Mathieu Massicotte, Leron Vandsburger, Eric Whiteway, and Victor Yu. Experimental Review of Graphene. *ISRN Condensed Matter Physics*, 2012:1–56, apr 2012. 1
- [17] K. S. Novoselov. Nobel Lecture: Graphene: Materials in the Flatland. *Reviews of Modern Physics*, 83(3):837–849, 2011. 1
- [18] V. Meunier, A. G. Souza Filho, E. B. Barros, and M. S. Dresselhaus. Physical properties of low-dimensional sp₂-based carbon nanostructures. *Reviews of Modern Physics*, 88(2), 2016. 1
- [19] H. W. Kroto, J. R. Heath, S. C. O’Brien, R. F. Curl, and R. E. Smalley. C₆₀: Buckminsterfullerene. *Nature*, 318(6042):162–163, nov 1985. 1
- [20] Richard E. Smalley. Discovering the fullerenes. *Reviews of Modern Physics*, 69(3):723–730, 1997. 1
- [21] M. S. Dresselhaus, G. Dresselhaus, and P.C. Eklund. *Science of Fullerenes and Carbon Nanotubes*. Elsevier, 1996. 1

- [22] K S Novoselov, A K Geim, S V Morozov, D Jiang, Y Zhang, S V Dubonos, I V Grigorieva, and A A Firsov. Electric Field Effect in Atomically Thin Carbon Films. *Science*, 306(October):666–669, 2004. 1
- [23] K. S. Novoselov, A. K. Geim, S. V. Morozov, D. Jiang, M. I. Katsnelson, I. V. Grigorieva, S. V. Dubonos, and A. A. Firsov. Two-dimensional gas of massless Dirac fermions in graphene. *Nature*, 2005. 1
- [24] A. K. Geim and I. V. Grigorieva. Van der Waals heterostructures. *Nature*, 499(7459):419–425, 2013. 2
- [25] K S Novoselov, A Mishchenko, A Carvalho, and A H Castro Neto. 2D materials and van der Waals heterostructures. *Science*, 353(6298), 2016. 2
- [26] Natalie Briggs, Shruti Subramanian, Zhong Lin, Xufan Li, Xiaotian Zhang, Kehao Zhang, Kai Xiao, David Geohegan, Robert Wallace, Long Qing Chen, Mauricio Terrones, Aida Ebrahimi, Saptarshi Das, Joan Redwing, Christopher Hinkle, Kasra Momeni, Adri Van Duin, Vin Crespi, Swastik Kar, and Joshua A. Robinson. A roadmap for electronic grade 2D materials. *2D Materials*, 6(2), 2019. 2
- [27] Feliciano Giustino, Jin Hong Lee, Felix Trier, Manuel Bibes, Stephen M Winter, Roser Valentí, Young-woo Son, Louis Taillefer, Christoph Heil, Adriana I Figueroa, Bernard Plaçais, Quansheng Wu, Oleg V Yazyev, Erik P A M Bakkers, Jesper Nygård, Pol Forn-Díaz, Silvano De Franceschi, J W McIver, L E F Foa Torres, Tony Low, Anshuman Kumar, Regina Galceran, Sergio O Valenzuela, Marius V Costache, Aurélien Manchon, Eun-Ah Kim, Gabriel R Schleder, Adalberto Fazzio, and Stephan Roche. The 2021 quantum materials roadmap. *Journal of Physics: Materials*, 3(4):042006, jan 2021. 2
- [28] Rafael R Del Grande, Marcos G Menezes, Rodrigo B Capaz, Rafael R Del Grande, Marcos G Menezes, and Rodrigo B Capaz. Layer breathing and shear modes in

- multilayer graphene : A DFT-vdW study. *Journal of Physics: Condensed Matter*, 31(29):1–9, jul 2019. 2
- [29] Stephen Carr, Daniel Massatt, Shiang Fang, Paul Cazeaux, Mitchell Luskin, and Efthimios Kaxiras. Twistorics: Manipulating the electronic properties of two-dimensional layered structures through their twist angle. *Physical Review B*, 95(7):1–6, 2017. 3
- [30] Stephen Carr, Shiang Fang, Ziyan Zhu, and Efthimios Kaxiras. Exact continuum model for low-energy electronic states of twisted bilayer graphene. *Physical Review Research*, 1(1):013001, aug 2019. 3
- [31] Stephen Carr, Shiang Fang, Hoi Chun Po, Ashvin Vishwanath, and Efthimios Kaxiras. Derivation of Wannier orbitals and minimal-basis tight-binding Hamiltonians for twisted bilayer graphene: First-principles approach. *Physical Review Research*, 1(3):033072, nov 2019. 3
- [32] Ziyan Zhu, Stephen Carr, Daniel Massatt, Mitchell Luskin, and Efthimios Kaxiras. Twisted Trilayer Graphene: A Precisely Tunable Platform for Correlated Electrons. *Physical Review Letters*, 125(11):1–6, 2020. 3
- [33] Stephen Carr, Shiang Fang, and Efthimios Kaxiras. Electronic-structure methods for twisted moiré layers. *Nature Reviews Materials*, 5(10):748–763, 2020. 3
- [34] Andreij C. Gadelha, Douglas A. A. Ohlberg, Cassiano Rabelo, Eliel G. S. Neto, Thiago L. Vasconcelos, João L. Campos, Jessica S. Lemos, Vinícius Ornelas, Daniel Miranda, Rafael Nadas, Fabiano C. Santana, Kenji Watanabe, Takashi Taniguchi, Benoit van Troeye, Michael Lamparski, Vincent Meunier, Viet-Hung Nguyen, Dawid Paszko, Jean-Christophe Charlier, Leonardo C. Campos, Luiz G. Cançado, Gilberto Medeiros-Ribeiro, and Ado Jorio. Localization of lattice dynamics in low-angle twisted bilayer graphene. *Nature*, 590(7846):405–409, feb 2021. 3

- [35] S Fang K Watanabe T Taniguchi E Kaxiras Y. Cao V. Fatemi, Pablo Jarillo-Herrero, Yuan Cao, Valla Fatemi, Shiang Fang, Kenji Watanabe, Takashi Taniguchi, Efthimios Kaxiras, and Pablo Jarillo-Herrero. Unconventional superconductivity in magic-angle graphene superlattices. *Nature*, 556(7699):43–50, 2018. 3
- [36] Yuan Cao, Valla Fatemi, Ahmet Demir, Shiang Fang, Spencer L. Tomarken, Jason Y. Luo, Javier D. Sanchez-Yamagishi, Kenji Watanabe, Takashi Taniguchi, Efthimios Kaxiras, Ray C. Ashoori, and Pablo Jarillo-Herrero. Correlated insulator behaviour at half-filling in magic-angle graphene superlattices. *Nature*, 556(7699):80–84, 2018. 3
- [37] F. J. Culchac, R. R. Del Grande, Rodrigo B. Capaz, Leonor Chico, and E. Suárez Morell. Flat bands and gaps in twisted double bilayer graphene. *Nanoscale*, 12(8):5014–5020, 2020. 3
- [38] Sumio Iijima. Helical microtubules of graphitic carbon. *Nature*, 354(6348):56–58, nov 1991. 3
- [39] R.R. R. Del Grande, Alexandre F. Fonseca, Rodrigo B. Capaz, R R Del Grande, Alexandre F. Fonseca, Rodrigo B. Capaz, R.R. R. Del Grande, Alexandre F. Fonseca, and Rodrigo B. Capaz. Energy barriers for collapsing large-diameter carbon nanotubes. *Carbon*, 159:161–165, apr 2020. 3
- [40] R. Bruce Weisman and Sergei M. Bachilo. Dependence of optical transition energies on structure for single-walled carbon nanotubes in aqueous suspension: An empirical Kataura plot. *Nano Letters*, 3(9):1235–1238, sep 2003. 3, 16, 58
- [41] Feng Wang, Gordana Dukovic, Louis E Brus, and Tony F Heinz. The optical resonances in carbon nanotubes arise from excitons. *Science (New York, N.Y.)*, 308(5723):838–41, may 2005. 3, 16, 17

- [42] Saunab Ghosh, Sergei M. Bachilo, Rebecca A. Simonette, Kathleen M. Beckingham, and R. Bruce Weisman. Oxygen doping modifies near-infrared band gaps in fluorescent single-walled carbon nanotubes. *Science*, 330(6011):1656–1659, 2010. 3, 21, 24, 70, 73
- [43] Xiaowei He, Nicolai F. Hartmann, Xuedan Ma, Younghée Kim, Rachelle Ihly, Jeffrey L. Blackburn, Weilu Gao, Junichiro Kono, Yohei Yomogida, Atsushi Hirano, Takeshi Tanaka, Hiromichi Kataura, Han Htoon, Stephen K. Doorn, Jeffrey L. Blackburn, Junichiro Kono, Han Htoon, Weilu Gao, Nicolai F. Hartmann, Stephen K. Doorn, Atsushi Hirano, Rachelle Ihly, Xuedan Ma, Yohei Yomogida, Hiromichi Kataura, and Xiaowei He. Tunable room-temperature single-photon emission at telecom wavelengths from sp₃ defects in carbon nanotubes. *Nature Photonics*, 11(9):577–582, jul 2017. 3, 21, 24
- [44] X. He, H. Htoon, S. K. Doorn, W. H. P. Pernice, F. Pyatkov, R. Krupke, A. Jeantet, Y. Chassagneux, and C. Voisin. Carbon nanotubes as emerging quantum-light sources. *Nature Materials*, 17(8):663–670, aug 2018. 3
- [45] M.S. Dresselhaus, G. Dresselhaus, and A. Jorio. *Group Theory - Applications to the Physics of Condensed Matter*, volume 84. 2013. 4, 10, 19
- [46] Ge G. Samsonidze, R. Saito, A. Jorio, M. A. Pimenta, A. G. Souza Filho, A. Grüneis, G. Dresselhaus, and M. S. Dresselhaus. The concept of cutting lines in carbon nanotube science. *Journal of Nanoscience and Nanotechnology*, 3(6):431–458, 2003. 6
- [47] R. Saito, K. Sato, Y. Oyama, J. Jiang, Ge G. Samsonidze, G. Dresselhaus, and M. S. Dresselhaus. Cutting lines near the Fermi energy of single-wall carbon nanotubes. *Physical Review B - Condensed Matter*, 72(15):1–4, 2005. 6, 9

- [48] M. V. Avramenko, S. B. Rochal, and Yu I. Yuzyuk. Symmetry of the carbon nanotube modes and their origin from the phonon branches of graphene. *Physical Review B - Condensed Matter and Materials Physics*, 87(3):1–8, 2013. 6
- [49] M BURGHARD. Electronic and vibrational properties of chemically modified single-wall carbon nanotubes. *Surface Science Reports*, 58:1–109, oct 2005. 7, 9, 93
- [50] Riichiro Saito, Mitsutaka Fujita, G. Dresselhaus, and M. S. Dresselhaus. Electronic structure of graphene tubules based on C₆₀. *Physical Review B*, 46(3):1804–1811, 1992. 9
- [51] R. Saito, M. Fujita, G. Dresselhaus, and M. S. Dresselhaus. Electronic structure of chiral graphene tubules. *Applied Physics Letters*, 60(18):2204–2206, 1992. 9
- [52] R Saito, G Dresselhaus, and M S Dresselhaus. *Physical Properties of Carbon Nanotubes*. PUBLISHED BY IMPERIAL COLLEGE PRESS AND DISTRIBUTED BY WORLD SCIENTIFIC PUBLISHING CO., jul 1998. 9, 32
- [53] Naomichi Sato, Yuki Tatsumi, and Riichiro Saito. Circular dichroism of single-wall carbon nanotubes. *Physical Review B*, 95(15):1–11, 2017. 9
- [54] Riichiro Saito, M. Shoufie Ukhtary, Sake Wang, and Yuya Iwasaki. Circular dichroism of doped carbon nanotubes. *Journal of Applied Physics*, 128(16), 2020. 9
- [55] A. Jorio, C. Fantini, M. A. Pimenta, R. B. Capaz, Ge G. Samsonidze, G. Dresselhaus, M. S. Dresselhaus, J. Jiang, N. Kobayashi, A. Grüneis, and R. Saito. Resonance Raman spectroscopy (n,m)-dependent effects in small-diameter single-wall carbon nanotubes. *Physical Review B - Condensed Matter and Materials Physics*, 71(7):1–11, 2005. 9

- [56] A.R. Amanda R Amori, Zhentao Hou, and Todd D Krauss. Excitons in Single-Walled Carbon Nanotubes and Their Dynamics. *Annual Review of Physical Chemistry*, 69(January):1–19, 2018. 9, 13, 18, 21, 24
- [57] Valentin N. Popov. Curvature effects on the structural, electronic and optical properties of isolated single-walled carbon nanotubes within a symmetry-adapted non-orthogonal tight-binding model. *New Journal of Physics*, 6, 2004. 11
- [58] Ge. G. Samsonidze, R. Saito, N. Kobayashi, A. Grüneis, J. Jiang, A. Jorio, S. G. Chou, G. Dresselhaus, M. S. Dresselhaus, A. Grüneis, N. Kobayashi, S. G. Chou, Ge. G. Samsonidze, G. Dresselhaus, R. Saito, and M. S. Dresselhaus. Family behavior of the optical transition energies in single-wall carbon nanotubes of smaller diameters. *Applied Physics Letters*, 85(23):5703–5705, 2004. 11, 16
- [59] Eduardo B. Barros, Rodrigo B. Capaz, Ado Jorio, Georgii G. Samsonidze, Antonio G. Souza Filho, Sohrab Ismail-Beigi, Catalin D. Spataru, Steven G. Louie, Gene Dresselhaus, and Mildred S. Dresselhaus. Selection rules for one- and two-photon absorption by excitons in carbon nanotubes. *Physical Review B*, 73(24):241406, jun 2006. 11, 18, 19, 81, 87, 89
- [60] Hiroshi Ajiki. Exciton states and optical properties of carbon nanotubes. *Journal of Physics Condensed Matter*, 24(48), 2012. 13
- [61] Yuhei Miyauchi. Photoluminescence studies on exciton photophysics in carbon nanotubes. *Journal of Materials Chemistry C*, 1(40):6499–6521, 2013. 13, 18, 21
- [62] Marvin L. Cohen and Steven G. Louie. *Fundamentals of Condensed Matter Physics*. Cambridge University Press, may 2016. 13, 15

- [63] Larry Lüer, Sajjad Hoseinkhani, Dario Polli, Jared Crochet, Tobias Hertel, and Guglielmo Lanzani. Size and mobility of excitons in (6, 5) carbon nanotubes. *Nature Physics*, 5(1):54–58, jan 2009. 13, 16, 58
- [64] Robert S Knox. *Theory of Excitons*. Academic Press, New York and London, 1963. 14
- [65] G. Dresselhaus. Effective Mass Approximation For Excitons. *Journal of Physical Chemistry Solids*, 1:14–22, 1956. 14
- [66] Diana Y. Qiu, Galit Cohen, Dana Novichkova, and Sivan Refaelly-Abramson. Signatures of Dimensionality and Symmetry in Exciton Bandstructure: Consequences for Time-Evolution. pages 1–6, mar 2021. 15, 16
- [67] J. Maultzsch, R. Pomraenke, S. Reich, E. Chang, D. Prezzi, A. Ruini, E. Molinari, M. S. Strano, C. Thomsen, and C. Lienau. Exciton binding energies in carbon nanotubes from two-photon photoluminescence. *Physical Review B*, 72(24):241402, dec 2005. 16, 17
- [68] Jack Deslippe, Mario Dipoppa, David Prendergast, Marcus V. O. Moutinho, Rodrigo B. Capaz, and Steven G. Louie. ElectronHole Interaction in Carbon Nanotubes: Novel Screening and Exciton Excitation Spectra. *Nano Letters*, 9(4):1330–1334, apr 2009. 16, 17, 44, 56, 95
- [69] Pierluigi Cudazzo, Ilya V. Tokatly, and Angel Rubio. Dielectric screening in two-dimensional insulators: Implications for excitonic and impurity states in graphane. *Physical Review B - Condensed Matter and Materials Physics*, 84(8):1–7, 2011. 16, 17

- [70] Diana Y. Qiu, Felipe H. Da Jornada, and Steven G. Louie. Screening and many-body effects in two-dimensional crystals: Monolayer MoS₂. *Physical Review B*, 93(23):1–12, 2016. 16, 17
- [71] Christoph Mann and Tobias Hertel. 13 nm Exciton Size in (6,5) Single-Wall Carbon Nanotubes. *Journal of Physical Chemistry Letters*, 7(12):2276–2280, 2016. 16, 17
- [72] Tsuneya Ando. Excitons in Carbon Nanotubes. *Journal of the Physics Society Japan*, 66(4):1066–1073, apr 1997. 16
- [73] Ying Zhong Ma, Leonas Valkunas, Sergei M. Bachilo, and Graham R. Fleming. Exciton binding energy in semiconducting single-walled carbon nanotubes. *Journal of Physical Chemistry B*, 109(33):15671–15674, 2005. 16
- [74] G Dukovic, G Dukovic, F Wang, F Wang, D Song, D Song, M Y Sfeir, M Y Sfeir, T F Heinz, T F Heinz, L.e, and L.e. Structural dependence of excitonic optical transitions and band gap energies in carbon nanotubes. *Nano Letters*, 5(112314):1–5, 2005. 16
- [75] H. Telg, J. Maultzsch, S. Reich, and C. Thomsen. Resonant-Raman intensities and transition energies of the E11 transition in carbon nanotubes. *Physical Review B - Condensed Matter and Materials Physics*, 74(11):1–5, 2006. 16, 58
- [76] R. Pomraenke, J. Maultzsch, S. Reich, E. Chang, D. Prezzi, A. Ruini, E. Molinari, M. S. Strano, C. Thomsen, and C. Lienau. Two-photon photoluminescence and exciton binding energies in single-walled carbon nanotubes. *Physica Status Solidi (B) Basic Research*, 2006. 16
- [77] Ying-Zhong Zhong Ma, Catalin D. Spataru, Leonas Valkunas, Steven G. Louie, and Graham R. Fleming. Spectroscopy of zigzag single-walled carbon nanotubes: Comparing femtosecond transient absorption spectra with ab initio calculations.

Physical Review B - Condensed Matter and Materials Physics, 74(8):1–9, 2006. 16, 58

- [78] Feng Wang, David J. Cho, Brian Kessler, Jack Deslippe, P. James Schuck, Steven G. Louie, Alex Zettl, Tony F. Heinz, and Y. Ron Shen. Observation of excitons in one-dimensional metallic single-walled carbon nanotubes. *Physical Review Letters*, 99(22), 2007. 16
- [79] Stephen K. Doorn, Paulo T. Araujo, Kenji Hata, and Ado Jorio. Excitons and exciton-phonon coupling in metallic single-walled carbon nanotubes: Resonance Raman spectroscopy. *Physical Review B - Condensed Matter and Materials Physics*, 78(16):1–9, 2008. 16
- [80] Sergei M Bachilo, Michael S Strano, Carter Kittrell, Robert H Hauge, Richard E Smalley, and R Bruce Weisman. Structure-Assigned Optical Spectra of Single-Walled Carbon Nanotubes. *Science*, 298(5602):2361–2366, 2002. 16, 58
- [81] Matthew Y. Sfeir, Tobias Beetz, Feng Wang, Limin Huang, X. M. Henry Huang, Mingyuan Huang, J. Hone, Stephen O’Brien, J. A. Misewich, Tony F. Heinz, Lijun Wu, Yimei Zhu, and Louis E. Brus. Optical spectroscopy of individual single-walled carbon nanotubes of defined chiral structure. *Science*, 2006. 16
- [82] Paulo T. Araujo, Stephen K. Doorn, Svetlana Kilina, Sergei Tretiak, Erik Einarsson, Shigeo Maruyama, Helio Chacham, Marcos A. Pimenta, and Ado Jorio. Third and Fourth Optical Transitions in Semiconducting Carbon Nanotubes. *Physical Review Letters*, 98(6):067401, feb 2007. 16
- [83] R. Saito, K. Sato, P. T. Araujo, A. Jorio, G. Dresselhaus, and M. S. Dresselhaus. Exciton energy calculations for single wall carbon nanotubes. *Physica Status Solidi (B) Basic Research*, 246(11-12):2581–2585, 2009. 16

- [84] Vasili Perebeinos, J. Tersoff, and Phaedon Avouris. Scaling of excitons in carbon nanotubes. *Phys. Rev. Lett.*, 2(June):8–11, 2004. 18
- [85] Rodrigo B. Capaz, Catalin D. Spataru, Sohrab Ismail-Beigi, and Steven G. Louie. Excitons in carbon nanotubes: Diameter and chirality trends. In *Physica Status Solidi (B) Basic Research*, 2007. 18, 56
- [86] Y. Miyauchi, R. Saito, K. Sato, Y. Ohno, S. Iwasaki, T. Mizutani, J. Jiang, and S. Maruyama. Dependence of exciton transition energy of single-walled carbon nanotubes on surrounding dielectric materials. *Chemical Physics Letters*, 442(4-6):394–399, 2007. 18
- [87] Yuhei Miyauchi, Hideki Hirori, Kazunari Matsuda, and Yoshihiko Kanemitsu. Radiative lifetimes and coherence lengths of one-dimensional excitons in single-walled carbon nanotubes. *Physical Review B - Condensed Matter and Materials Physics*, 80(8):1–4, 2009. 18
- [88] Yuxuan Lin, Xi Ling, Lili Yu, Shengxi Huang, Allen L. Hsu, Yi Hsien Lee, Jing Kong, Mildred S. Dresselhaus, and Tomás Palacios. Dielectric screening of excitons and trions in single-layer MoS₂. *Nano Letters*, 14(10):5569–5576, 2014. 18
- [89] Archana Raja, Andrey Chaves, Jaeeun Yu, Ghidewon Arefe, Heather M. Hill, Albert F. Rigosi, Timothy C. Berkelbach, Philipp Nagler, Christian Schüller, Tobias Korn, Colin Nuckolls, James Hone, Louis E. Brus, Tony F. Heinz, David R. Reichman, and Alexey Chernikov. Coulomb engineering of the bandgap and excitons in two-dimensional materials. *Nature Communications*, 2017. 18
- [90] Mathias Steiner, Marcus Freitag, Vasili Perebeinos, Anton Naumov, Joshua P. Small, Ageeth A. Bol, and Phaedon Avouris. Gate-Variable Light Absorption and Emission in a Semiconducting Carbon Nanotube. *Nano Letters*, 9(10):3477–3481, oct 2009. 18, 60

- [91] Catalin D. Spataru and François Léonard. Tunable band gaps and excitons in doped semiconducting carbon nanotubes made possible by acoustic plasmons. *Physical Review Letters*, 104(17):1–4, 2010. 18, 60
- [92] Catalin D. Spataru and François Léonard. Quasiparticle and exciton renormalization effects in electrostatically doped semiconducting carbon nanotubes. *Chemical Physics*, 413:81–88, feb 2013. 18, 60
- [93] Ji Ung Lee. Band-gap renormalization in carbon nanotubes: Origin of the ideal diode behavior in carbon nanotube p-n structures. *Physical Review B - Condensed Matter and Materials Physics*, 75(7):1–5, 2007. 18, 60
- [94] Klaus H. Eckstein, Holger Hartleb, Melanie M. Achsnich, Friedrich Schöppler, and Tobias Hertel. Localized Charges Control Exciton Energetics and Energy Dissipation in Doped Carbon Nanotubes. *ACS Nano*, 2017. 18, 23, 58, 60
- [95] Catalin D. Spataru and François Léonard. Many-body effects on the electronic and optical properties of strained semiconducting carbon nanotubes. *Physical Review B*, 88(4):045404, jul 2013. 18, 58
- [96] I. B. Mortimer and R. J. Nicholas. Role of bright and dark excitons in the temperature-dependent photoluminescence of carbon nanotubes. *Physical Review Letters*, 98(2):027404, jan 2007. 18, 22, 23
- [97] O. N. Torrens, M. Zheng, and J. M. Kikkawa. Energy of K-momentum dark excitons in carbon nanotubes by optical spectroscopy. *Physical Review Letters*, 101(15):3–6, 2008. 18
- [98] Jeffrey L. Blackburn, Josh M. Holt, Veronica M. Irurzun, Daniel E. Resasco, and Garry Rumbles. Confirmation of K-momentum dark exciton vibronic sidebands us-

- ing ¹³C-labeled, highly enriched (6,5) single-walled carbon nanotubes. *Nano Letters*, 12(3):1398–1403, 2012. 18
- [99] A. Ishii, H. Machiya, and Y. K. Kato. High Efficiency Dark-to-Bright Exciton Conversion in Carbon Nanotubes. *Physical Review X*, 91(4):41048, 2019. 18
- [100] Catalin D. Spataru, Sohrab Ismail-Beigi, Lorin X. Benedict, and Steven G. Louie. Excitonic effects and optical spectra of single-walled carbon nanotubes. *AIP Conference Proceedings*, 772:1061–1062, 2005. 18, 21, 58
- [101] Ryusuke Matsunaga, Kazunari Matsuda, and Yoshihiko Kanemitsu. Evidence for dark excitons in a single carbon nanotube due to the Aharonov-Bohm effect. *Physical Review Letters*, 101(14):3–6, 2008. 18
- [102] Svetlana Kilina, Ekaterina Badaeva, Andrei Piryatinski, Sergei Tretiak, Avadh Saxena, and Alan R. Bishop. Bright and dark excitons in semiconductor carbon nanotubes: insights from electronic structure calculations. *Physical Chemistry Chemical Physics*, 11(21):4113, may 2009. 18
- [103] J. Maultzsch, R. Pomraenke, S. Reich, E. Chang, D. Prezzi, A. Ruini, E. Molinari, M. S. Strano, C. Thomsen, and C. Lienau. Excitons in carbon nanotubes. *Physica Status Solidi (B) Basic Research*, 243(13):3204–3208, 2006. 18
- [104] Axel Hagen, Mathias Steiner, Markus B. Raschke, Christoph Lienau, Tobias Hertel, Huihong Qian, Alfred J. Meixner, and Achim Hartschuh. Exponential decay lifetimes of excitons in individual single-walled carbon nanotubes. *Physical Review Letters*, 95(19):1–4, 2005. 18
- [105] Z. M. Li, Z. K. Tang, H. J. Liu, N. Wang, C. T. Chan, R. Saito, S. Okada, G. D. Li, J. S. Chen, N. Nagasawa, and S. Tsuda. Polarized Absorption Spectra of Single-

Walled 4 ÅCarbon Nanotubes Aligned in Channels of an AlPO 4 5 Single Crystal.

Physical Review Letters, 87(12):127401, aug 2001. 21

- [106] Hayk Harutyunyan, Tobias Gokus, Alexander A Green, Mark C Hersam, Maria Allegrini, and Achim Hartschuh. Defect-Induced Photoluminescence from Dark Excitonic States in Individual Single-Walled Carbon Nanotubes. *Nano Letters*, 9(5):2010–2014, may 2009. 21, 22
- [107] Yuhei Miyauchi, Munechiyo Iwamura, Shinichiro Mouri, Tadashi Kawazoe, Motoichi Ohtsu, and Kazunari Matsuda. Brightening of excitons in carbon nanotubes on dimensionality modification. *Nature Photonics*, 7(9):715–719, 2013. 21, 23
- [108] Xuedan Ma, Xuedan Ma, Lyudmyla Adamska, Lyudmyla Adamska, Hisato Yamaguchi, Hisato Yamaguchi, Sibel Ebru Yalcin, Sibel Ebru Yalcin, Sergei Tretiak, Sergei Tretiak, Stephen K Doorn, Stephen K Doorn, Han Htoon, and Han Htoon. Electronic Structure and Chemical Nature of Oxygen Dopant States in Carbon Nanotubes. *ACS Nano*, 8(10):10782–10789, 2014. 21
- [109] Nicolai F. Hartmann, Kirill A. Velizhanin, Erik H. Haroz, Mijin Kim, Xuedan Ma, Yuhuang Wang, Han Htoon, and Stephen K. Doorn. Photoluminescence Dynamics of Aryl sp³ Defect States in Single-Walled Carbon Nanotubes. *ACS Nano*, 10(9):8355–8365, 2016. 21, 23, 24
- [110] Mijin Kim, Lyudmyla Adamska, Nicolai F. Hartmann, Hyejin Kwon, Jin Liu, Kirill A. Velizhanin, Yanmei Piao, Lyndsey R. Powell, Brendan Meany, Stephen K. Doorn, Sergei Tretiak, and Yu Huang Wang. Fluorescent Carbon Nanotube Defects Manifest Substantial Vibrational Reorganization. *Journal of Physical Chemistry C*, 120(20):11268–11276, 2016. 21
- [111] Hyejin Kwon, Alona Furmanchuk, Mijin Kim, Brendan Meany, Yong Guo, George C. Schatz, and Yuhuang Wang. Molecularly Tunable Fluorescent Quan-

- tum Defects. *Journal of the American Chemical Society*, 138(21):6878–6885, 2016. 21, 22, 24
- [112] Xiaojun Wei, Takeshi Tanaka, Naoto Akizuki, Yuhei Miyauchi, Kazunari Matsuda, Mari Ohfuchi, and Hiromichi Kataura. Single-chirality separation and optical properties of (5,4) single-wall carbon nanotubes. *Journal of Physical Chemistry C*, 120(19):10705–10710, 2016. 21
- [113] Yutaka Maeda, Shun Minami, Yuya Takehana, Jing Shuang Dang, Shun Aota, Kazunari Matsuda, Yuhei Miyauchi, Michio Yamada, Mitsuaki Suzuki, Rui Sheng Zhao, Xiang Zhao, and Shigeru Nagase. Tuning of the photoluminescence and up-conversion photoluminescence properties of single-walled carbon nanotubes by chemical functionalization. *Nanoscale*, 8(38):16916–16921, 2016. 21
- [114] Tomonari Shiraishi, Tomohiro Shiraki, and Naotoshi Nakashima. Substituent effects on the redox states of locally functionalized single-walled carbon nanotubes revealed by in situ photoluminescence spectroelectrochemistry. *Nanoscale*, 9(43):16900–16907, 2017. 21, 24
- [115] Xiaowei He, Brendan J. Gifford, Nicolai F. Hartmann, Rachelle Ihly, Xuedan Ma, Svetlana V. Kilina, Yue Luo, Kamran Shayan, Stefan Strauf, Jeffrey L. Blackburn, Sergei Tretiak, Stephen K. Doorn, and Han Htoon. Low-Temperature Single Carbon Nanotube Spectroscopy of sp₃Quantum Defects. *ACS Nano*, 2017. 21
- [116] Tomohiro Shiraki, Shunsuke Uchimura, Tomonari Shiraishi, Hisashi Onitsuka, and Naotoshi Nakashima. Near infrared photoluminescence modulation by defect site design using aryl isomers in locally functionalized single-walled carbon nanotubes. *Chemical Communications*, 53(93):12544–12547, 2017. 21, 22, 24, 58
- [117] Younghée Kim, Kirill A. Velizhanin, Xiaowei He, Ibrahim Sarpkaya, Yohei Yomogida, Takeshi Tanaka, Hiromichi Kataura, Stephen K. Doorn, and Han Htoon.

Photoluminescence Intensity Fluctuations and Temperature-Dependent Decay Dynamics of Individual Carbon Nanotube sp₃ Defects. *The Journal of Physical Chemistry Letters*, pages 1423–1430, 2019. 21

- [118] X. He, H. Htoon, S. K. Doorn, W. H.P. Pernice, F. Pyatkov, R. Krupke, A. Jeantet, Y. Chassagneux, and C. Voisin. Carbon nanotubes as emerging quantum-light sources. *Nature Materials*, 17(8):663–670, 2018. 21, 24
- [119] Amanda R. Amori, Jamie E. Rossi, Brian J. Landi, and Todd D. Krauss. Defects Enable Dark Exciton Photoluminescence in Single-Walled Carbon Nanotubes. *Journal of Physical Chemistry C*, 122(6):3599–3607, 2018. 21, 23
- [120] Lyndsey R Powell, Yanmei Piao, Allen L Ng, and Yuhuang Wang. Channeling Excitons to Emissive Defect Sites in Carbon Nanotube Semiconductors beyond the Dilute Regime. *The Journal of Physical Chemistry Letters*, 9(11):2803–2807, jun 2018. 21
- [121] Avishhek Saha, Brendan J. Gifford, Xiaowei He, Geyou Ao, Ming Zheng, Hiromichi Kataura, Han Htoon, Svetlana Kilina, Sergei Tretiak, and Stephen K. Doorn. Narrow-band single-photon emission through selective aryl functionalization of zigzag carbon nanotubes. *Nature Chemistry*, 10(11):1089–1095, nov 2018. 21, 24, 58, 75
- [122] Xiaojian Wu, Mijin Kim, Haoran Qu, and Yu Huang Wang. Single-defect spectroscopy in the shortwave infrared. *Nature Communications*, 10(1):1–7, 2019. 21, 23
- [123] Brendan J. Gifford, Xiaowei He, Mijin Kim, Hyejin Kwon, Avishhek Saha, Andrew E. Sifain, Yuhuang Wang, Han Htoon, Svetlana Kilina, Stephen K. Doorn, and Sergei Tretiak. Optical Effects of Divalent Functionalization of Carbon Nanotubes. *Chemistry of Materials*, 31(17):6950–6961, 2019. 21, 24

- [124] Felix J Berger, Jan Lüttgens, Tim Nowack, Tobias Kutsch, Sebastian Lindenthal, Lucas Kistner, Christine C. Müller, Lukas M Bongartz, Victoria A Lumsargis, Yuriy Zakharko, and Jana Zaumseil. Brightening of Long, Polymer-Wrapped Carbon Nanotubes by sp₃ Functionalization in Organic Solvents. *ACS Nano*, 13(8):9259–9269, aug 2019. 21, 22
- [125] Matthew E. Sykes, Mijin Kim, Xiaojian Wu, Gary P. Wiederrecht, Lintao Peng, Yu Huang Wang, David J. Gosztola, and Xuedan Ma. Ultrafast Exciton Trapping at sp₃ Quantum Defects in Carbon Nanotubes. *ACS Nano*, 2019. 21
- [126] Brendan J. Gifford, Avishek Saha, Braden M. Weight, Xiaowei He, Geyou Ao, Ming Zheng, Han Htoon, Svetlana Kilina, Stephen K. Doorn, and Sergei Tretiak. Mod(n-m,3) Dependence of Defect-State Emission Bands in Aryl-Functionalized Carbon Nanotubes. *Nano Letters*, 19(12):8503–8509, dec 2019. 21, 23, 58, 74, 75
- [127] Amit Kumar Mandal, Xiaojian Wu, Joana S. Ferreira, Mijin Kim, Lyndsey R. Powell, Hyejin Kwon, Laurent Groc, Yu Huang Wang, and Laurent Cognet. Fluorescent sp₃ Defect-Tailored Carbon Nanotubes Enable NIR-II Single Particle Imaging in Live Brain Slices at Ultra-Low Excitation Doses. *Scientific Reports*, 10(1):1–9, 2020. 21
- [128] Brendan J. Gifford, Svetlana Kilina, Han Htoon, Stephen K. Doorn, and Sergei Tretiak. Controlling defect-state photophysics in covalently functionalized single-walled carbon nanotubes. *Accounts of Chemical Research*, 53(9):1791–1801, 2020. 21, 24, 58
- [129] Tomohiro Shiraki, Yuhei Miyauchi, Kazunari Matsuda, and Naotoshi Nakashima. Carbon nanotube photoluminescence modulation by local chemical and supramolecular chemical functionalization. *Accounts of Chemical Research*, 53(9):1846–1859, 2020. 21, 24

- [130] Kasidet Jing Trerayapiwat, Sven Lohmann, Xuedan Ma, and Sahar Sharifzadeh. Tuning spin-orbit coupling in (6,5) single-walled carbon nanotube doped with sp₃defects. *Journal of Applied Physics*, 129(1), 2021. 21, 57, 58, 59, 61
- [131] Svetlana Kilina, Jessica Ramirez, and Sergei Tretiak. Brightening of the lowest exciton in carbon nanotubes via chemical functionalization. *Nano Letters*, 12(5):2306–2312, 2012. 21, 24, 52
- [132] Benjamin O. Tayo and Slava V. Rotkin. Charge impurity as a localization center for singlet excitons in single-wall nanotubes. *Physical Review B - Condensed Matter and Materials Physics*, 86(12), 2012. 21, 23
- [133] Jinglin Mu, Yuchen Ma, Huabing Yin, Chengbu Liu, and Michael Rohlfing. Photoluminescence of Single-Walled Carbon Nanotubes: The Role of Stokes Shift and Impurity Levels. *Physical Review Letters*, 111(13):137401, sep 2013. 21, 52, 57, 58, 59, 92
- [134] Jessica Ramirez, Michael L. Mayo, Svetlana Kilina, and Sergei Tretiak. Electronic structure and optical spectra of semiconducting carbon nanotubes functionalized by diazonium salts. *Chemical Physics*, 413:89–101, 2013. 21
- [135] Brendan J. Gifford, Svetlana Kilina, Han Htoon, Stephen K. Doorn, and Sergei Tretiak. Exciton Localization and Optical Emission in Aryl-Functionalized Carbon Nanotubes. *Journal of Physical Chemistry C*, 122(3):1828–1838, 2018. 21, 23, 52
- [136] Brendan J. Gifford, Andrew E. Sifain, Han Htoon, Stephen K. Doorn, Svetlana Kilina, and Sergei Tretiak. Correction Scheme for Comparison of Computed and Experimental Optical Transition Energies in Functionalized Single-Walled Carbon Nanotubes. *Journal of Physical Chemistry Letters*, 9(10):2460–2468, 2018. 21

- [137] Wutthisak Prachamon, Sukit Limpijumnong, Sittipong Komin, An International Journal, Wutthisak Prachamon, Sukit Limpijumnong, and Sittipong Komin. Optical transitions of native defects in single-walled carbon nanotubes : Time-dependent density functional theory study. *Integrated Ferroelectrics*, 4587(1):1–13, feb 2018. 21
- [138] Jinglin Mu, Yuchen Ma, Huichun Liu, Tian Zhang, and Shuping Zhuo. Optical properties of semiconducting zigzag carbon nanotubes with and without defects. *Journal of Chemical Physics*, 150(2), 2019. 21, 57, 58, 59
- [139] Xiaowei He, Kirill A. Velizhanin, George Bullard, Yusong Bai, Jean-Hubert Olivier, Nicolai F. Hartmann, Brendan J. Gifford, Svetlana Kilina, Sergei Tretyak, Han Htoon, Michael J. Therien, and Stephen K. Doorn. Solvent- and Wavelength-Dependent Photoluminescence Relaxation Dynamics of Carbon Nanotube sp³ Defect States. *ACS Nano*, 12(8):8060–8070, aug 2018. 21
- [140] Kotaro Nagatsu, Shohei Chiashi, Satoru Konabe, and Yoshikazu Homma. Brightening of triplet dark excitons by atomic hydrogen adsorption in single-walled carbon nanotubes observed by photoluminescence spectroscopy. *Physical Review Letters*, 105(15):8–11, 2010. 22, 73, 74, 77
- [141] Rodrigo B. Capaz, Catalin D. Spataru, Sohrab Ismail-Beigi, and Steven G. Louie. Diameter and chirality dependence of exciton properties in carbon nanotubes. *Physical Review B*, 74(12):121401, sep 2006. 22, 56, 58
- [142] Wyatt K. Metzger, Timothy J. McDonald, Chaiwat Engtrakul, Jeffrey L. Blackburn, Gregory D. Scholes, Garry Rumbles, and Michael J. Heben. Temperature-Dependent Excitonic Decay and Multiple States in Single-Wall Carbon Nanotubes. *The Journal of Physical Chemistry C*, 111(9):3601–3606, mar 2007. 22, 23

- [143] Hyejin Kwon, Mijin Kim, Manuel Nutz, Nicolai F Hartmann, Vivien Perrin, Brendan Meany, Matthias S Hofmann, Charles W Clark, Han Htoon, Stephen K Doorn, Alexander Högele, and Yuhuang Wang. Probing Triions at Chemically Tailored Trapping Defects. *ACS Central Science*, 5(11):1786–1794, nov 2019. 23
- [144] Mijin Kim, Xiaojian Wu, Geyou Ao, Xiaowei He, Hyejin Kwon, Nicolai F. Hartmann, Ming Zheng, Stephen K. Doorn, YuHuang Wang, Geyou Ao Xiaowei He Hyejin Kwon Nicolai F Hartmann Ming Zheng Stephen K Doorn Mijin Kim Xiaojian Wu, and YuHuang Wang. Mapping Structure-Property Relationships of Organic Color Centers. *Chem*, 4(9):2180–2191, sep 2018. 24
- [145] Han Htoon, Hidenori Machiya, Yuichiro K. Kato, Xiaowei He, Akihiro Ishii, Stephen K. Doorn, and Nicolai F. Hartmann. Enhanced Single-Photon Emission from Carbon-Nanotube Dopant States Coupled to Silicon Microcavities. *Nano Letters*, 18(6):3873–3878, 2018. 24
- [146] Paolo Giannozzi, Stefano Baroni, Nicola Bonini, Matteo Calandra, Roberto Car, Carlo Cavazzoni, Davide Ceresoli, Guido L Chiarotti, Matteo Cococcioni, Ismaila Dabo, Andrea Dal Corso, Stefano de Gironcoli, Stefano Fabris, Guido Fratesi, Ralph Gebauer, Uwe Gerstmann, Christos Gougoussis, Anton Kokalj, Michele Lazzeri, Layla Martin-Samos, Nicola Marzari, Francesco Mauri, Riccardo Mazzarello, Stefano Paolini, Alfredo Pasquarello, Lorenzo Paulatto, Carlo Sbraccia, Sandro Scandolo, Gabriele Sclauzero, Ari P Seitsonen, Alexander Smogunov, Paolo Umari, and Renata M Wentzcovitch. QUANTUM ESPRESSO: a modular and open-source software project for quantum simulations of materials. *Journal of Physics: Condensed Matter*, 21(39):395502, sep 2009. 26, 40
- [147] J Enkovaara, C Rostgaard, and J J Mortensen. Advanced capabilities for materials modelling with Quantum ESPRESSO. *Journal of Physics: Condensed Matter*,

29(46):465901, 2017. 26, 40

- [148] Adriana Vela, M. V.O. Moutinho, F. J. Culchac, P. Venezuela, and Rodrigo B. Capaz. Electronic structure and optical properties of twisted multilayer graphene. *Physical Review B*, 94(15):1–9, 2018. 29
- [149] L. Brey and C. Tejedor. Raman tensor of covalent semiconductors. *Solid State Communications*, 48(4):403–406, oct 1983. 29
- [150] Gerhard Klimeck, R.Chris Bowen, Timothy B Boykin, Carlos Salazar-Lazaro, Thomas A Cwik, and Adrian Stoica. Si tight-binding parameters from genetic algorithm fitting. *Superlattices and Microstructures*, 27(2-3):77–88, feb 2000. 30
- [151] J. D. Correa, Antônio J R Da Silva, and M. Pacheco. Tight-binding model for carbon nanotubes from ab initio calculations. *Journal of Physics Condensed Matter*, 22(27), 2010. 32
- [152] W. Kohn and L. J. Sham. Self-Consistent Equations Including Exchange and Correlation Effects. *Physical Review*, 140(4A):A1133–A1138, nov 1965. 32, 36
- [153] W Kohn. Nobel Lecture: Electronic structure of matter—wave functions and density functionals. *Reviews of Modern Physics*, 71(5):1253–1266, oct 1999. 33
- [154] P. Hohenberg and W. Kohn. Inhomogeneous Electron Gas. *Physical Review*, 136(3B):B864–B871, nov 1964. 34
- [155] Fabien Tran, Julia Stelzl, and Peter Blaha. Rungs 1 to 4 of DFT Jacob’s ladder: Extensive test on the lattice constant, bulk modulus, and cohesive energy of solids. *Journal of Chemical Physics*, 144(20), 2016. 40
- [156] Kurt Lejaeghere, Gustav Bihlmayer, Torbjörn Björkman, Peter Blaha, Stefan Blügel, Volker Blum, Damien Caliste, Ivano E. Castelli, Stewart J. Clark, Andrea Dal Corso, Stefano De Gironcoli, Thierry Deutsch, John Kay Dewhurst,

Igor Di Marco, Claudia Draxl, Marcin Dułak, Olle Eriksson, José A. Flores-Livas, Kevin F. Garrity, Luigi Genovese, Paolo Giannozzi, Matteo Giantomassi, Stefan Goedecker, Xavier Gonze, Oscar Gränäs, E. K.U. Gross, Andris Gulans, François Gygi, D. R. Hamann, Phil J. Hasnip, N. A.W. Holzwarth, Diana Iușan, Dominik B. Jochym, François Jollet, Daniel Jones, Georg Kresse, Klaus Koepernik, Emine Küçükbenli, Yaroslav O. Kvashnin, Inka L.M. Locht, Sven Lubeck, Martijn Marsman, Nicola Marzari, Ulrike Nitzsche, Lars Nordström, Taisuke Ozaki, Lorenzo Paulatto, Chris J. Pickard, Ward Poelmans, Matt I.J. Probert, Keith Refson, Manuel Richter, Gian Marco Rignanese, Santanu Saha, Matthias Scheffler, Martin Schlipf, Karlheinz Schwarz, Sangeeta Sharma, Francesca Tavazza, Patrik Thunström, Alexandre Tkatchenko, Marc Torrent, David Vanderbilt, Michiel J. Van Setten, Veronique Van Speybroeck, John M. Wills, Jonathan R. Yates, Guo Xu Zhang, and Stefaan Cottenier. Reproducibility in density functional theory calculations of solids. *Science*, 2016. 40

- [157] John P. Perdew. Jacob's ladder of density functional approximations for the exchange-correlation energy. *AIP Conference Proceedings*, 577(i):1–20, 2001. 40
- [158] Ann E Mattsson. Density functional theory: In pursuit of the "divine" functional, oct 2002. 40
- [159] R. O. Jones. Density functional theory: Its origins, rise to prominence, and future. *Reviews of Modern Physics*, 2015. 40
- [160] F. Aryasetiawan and O. Gunnarsson. The GW method. *Reports on Progress in Physics*, 61(3):237–312, 1998. 41, 42
- [161] John P Perdew. Density functional theory and the band gap problem. *International Journal of Quantum Chemistry*, 28(19 S):497–523, 1985. 41

- [162] Hedin Lars. New Method for Calculating One Particle Green Function. *Physical Review*, 139(17):796–823, 1965. 41, 43
- [163] G. Strinati. Application of the Green's functions method to the study of the optical properties of semiconductors. *La Rivista del Nuovo Cimento*, 11(12):1–86, dec 1988. 41, 42, 47
- [164] Wilfried G. Aulbur, Lars Jönsson, and John W. Wilkins. Quasiparticle Calculations in Solids. *Solid State Physics - Advances in Research and Applications*, 54(C):1–218, 1999. 41
- [165] Lars Hedin. *On correlation effects in electron spectroscopies and the GW approximation*. PhD thesis, oct 1999. 41
- [166] Xia Leng, Fan Jin, Min Wei, and Yuchen Ma. GW method and Bethe-Salpeter equation for calculating electronic excitations. *Wiley Interdisciplinary Reviews: Computational Molecular Science*, 6(5):532–550, sep 2016. 41, 47
- [167] Giovanni Onida, Lucia Reining, and Angel Rubio. Electronic excitations: density-functional versus many-body Green's-function approaches. *Reviews of Modern Physics*, 74(2):601–659, jun 2002. 41
- [168] Lucia Reining. The GW approximation: content, successes and limitations. *Wiley Interdisciplinary Reviews: Computational Molecular Science*, page e1344, 2017. 41
- [169] Dorothea Golze, Marc Dvorak, and Patrick Rinke. The GW compendium: A practical guide to theoretical photoemission spectroscopy. *Frontiers in Chemistry*, 7(July), 2019. 41
- [170] S. G. Louie. Chapter 2 Predicting Materials and Properties: Theory of the Ground and Excited State. *Contemporary Concepts of Condensed Matter Science*, 2(C):9–53, 2006. 41

- [171] Mark S. Hybertsen and Steven G. Louie. Electron correlation in semiconductors and insulators: Band gaps and quasiparticle energies. *Physical Review B*, 34(8):5390–5413, oct 1986. 43, 45
- [172] Michael Rohlfing and Steven G. Louie. Electron-hole excitations and optical spectra from first principles. *Physical Review B*, 62(8):4927–4944, aug 2000. 43, 47
- [173] Jack Deslippe, Georgy Samsonidze, David A. Strubbe, Manish Jain, Marvin L. Cohen, and Steven G. Louie. BerkeleyGW: A massively parallel computer package for the calculation of the quasiparticle and optical properties of materials and nanostructures. *Computer Physics Communications*, 183(6):1269–1289, 2012. 43, 45
- [174] Diana Y. Qiu, Felipe H. Da Jornada, and Steven G. Louie. Optical spectrum of MoS₂: Many-body effects and diversity of exciton states. *Physical Review Letters*, 111(21), 2013. 47, 78
- [175] Johannes Lischner, Jack Deslippe, Manish Jain, and Steven G. Louie. First-principles calculations of quasiparticle excitations of open-shell condensed matter systems. *Physical Review Letters*, 109(3):1–5, 2012. 52, 89
- [176] Christian Wagner, Jörg Schuster, and André Schleife. Strain and screening: Optical properties of a small-diameter carbon nanotube from first principles. *Physical Review B*, 99(7):1–9, 2019. 56
- [177] Kelvin Suggs, Vernecia Person, and Xiao Qian Wang. Band engineering of oxygen doped single-walled carbon nanotubes. *Nanoscale*, 3(6):2465–2468, 2011. 57
- [178] Charles W. Bauschlicher. High Coverages of Hydrogen on a (10,0) Carbon Nanotube. *Nano Letters*, 1(5):3–7, 2001. 93

- [179] Philippe Christol, Pierre Lefebvre, and Henry Mathieu. Fractional-dimensional calculation of exciton binding energies in semiconductor quantum wells and quantum-well wires. *Journal of Applied Physics*, 74(9):5626–5637, 1993. 95
- [180] Thomas Olsen, Simone Latini, Filip Rasmussen, and Kristian S. Thygesen. Simple Screened Hydrogen Model of Excitons in Two-Dimensional Materials. *Physical Review Letters*, 116(5):1–5, 2016. 95

Appendix A

Empty Cylinder Model

In this appendix, we provide some analytical expressions using approximations for the eigenvalues and eigenvectors in CNTs.

A.1 Pristine CNT

The pristine CNT wave functions can be approximated by

$$\psi_{\mu,k} = Ae^{i(k_z z + \mu\theta)} f_{\mu,k}(z, \theta) \quad (\text{A.1})$$

where

$$f(z, \theta) = f(z + L, \theta) = f(z, \theta + 2\pi) \quad (\text{A.2})$$

is a periodic function. In our calculations for zigzag CNTs, $L \approx 4.2\text{\AA}$.

Based on that, we approximate those solutions to plane waves $e^{i(kz + \mu\theta)}$, which are solutions to the empty cylinder shell hamiltonian

$$H = -\frac{\hbar^2 \nabla^2}{2m^*} = -\frac{\hbar^2}{2m^*} \left(\frac{1}{R^2} \frac{\partial^2}{\partial \theta^2} + \frac{\partial^2}{\partial z^2} \right) \quad (\text{A.3})$$

where R is the cylinder radius and m^* is the electron (hole) effective mass. The eigenvalues to this hamiltonian are

$$E_{k,\mu} = \frac{\hbar^2}{2m^*} \left(k^2 + \frac{\mu^2}{R^2} \right) \quad (\text{A.4})$$

We are interested in working with the two (valence) conduction degenerate bands involved in the E_{11} exciton, which have angular momentum μ and $-\mu$. As in this analysis μ is constant we modify our hamiltonian to

$$H_{e(h)} = \frac{\hbar^2 k^2}{2m_{e(h)}^*} + (-)\frac{E_g}{2} \quad (\text{A.5})$$

where the $e(h)$ index and the $+(-)$ sign hold for a electron (hole) in the conduction (valence) band. In this model the bandgap at $k = 0$ is E_g . The bandgap and effective masses are obtained from our *ab initio* results.

We define the wavefunctions as

$$\psi_{k,\mu}^{e(h)} = \frac{1}{\sqrt{2\pi RL}} e^{i(\pm kz + \mu\theta)} \quad (\text{A.6})$$

where the $+(-)$ in the exponential guarantees that $\langle \psi^e | \psi^h \rangle = 0$, except at $k = 0$.

The E_{11} exciton wave function is approximately given by

$$\Psi(z_e - z_h) = \sum_k A(k) \psi_c(z_e) \psi_v(z_h) \quad (\text{A.7})$$

From our *ab initio* results, we can write $A(k) = A_0 e^{-(k/\Delta k)^2}$. Using eq. A.6 and supposing Δk is much smaller than the boundaries of the Brillouin zone ($k = \pi/L$) the exciton wavefunction in the real space is given by

$$\Psi(z_e - z_h) \approx \int_{-\infty}^{\infty} dk A(k) \psi_c(z_e) \psi_v(z_h) = \frac{\tilde{A}_0 \Delta k}{LR} e^{i\mu(\theta_e + \theta_h)} e^{-\left(\frac{z_e - z_h}{2/\Delta k}\right)^2} \quad (\text{A.8})$$

so the exciton size is given by $\delta_0 = 2/\Delta k$. It is important to note that this wavefunction intensity depends on the relative coordinate $z_e - z_h$ and does not depend on the exciton center of mass coordinate $Z_{CM} = (m_e z_e + m_h z_h)/(m_e + m_h)$.

A.2 CNT-H

Now we add an impurity to the CNT. In our calculations two important features were observed: the split of degenerate bands and an impurity state in the middle of the bandgap.

We can easily understand the split of the degenerate pristine CNT bands by treating the impurity effect as a local perturbing potential

$$H' = -V_0 \delta(z - z_0) \delta(\theta - \theta_0) \quad (\text{A.9})$$

Now we write the pristine wavefunctions as in eq. A.1. We can recover the plane wave by setting $f(z, \theta) = 1$. The normalization factor is given by

$$\int R d\theta dz \psi_{\mu,k} \psi_{\mu,k}^* = 1 \rightarrow |A|^2 \int R d\theta dz |f(z, \theta)|^2 = 1 \quad (\text{A.10})$$

$$|A|^2 = \frac{1}{R \int_0^L dz \int_0^{2\pi} d\theta |f(z, \theta)|^2} \quad (\text{A.11})$$

When working with supercells with size $N_{cells}L$, containing N_{cells} unit cells, the normalization factor is given by

$$|A|^2 = \frac{1}{R \int_0^{N_{cells}L} dz \int_0^{2\pi} d\theta |f(z, \theta)|^2} \quad (\text{A.12})$$

As the periodic function f has a period L in the z direction we can state that

$$R \int_0^{N_{cells}L} dz \int_0^{2\pi} d\theta |f(z, \theta)|^2 = N_{cells} \left(R \int_0^L dz \int_0^{2\pi} d\theta |f(z, \theta)|^2 \right) \quad (\text{A.13})$$

and, finally

$$|A|^2 = \frac{1}{N_{cells} I} \quad (\text{A.14})$$

where $I = R \int_0^L dz \int_0^{2\pi} d\theta |f(z, \theta)|^2$.

The unperturbed states of pristine CNT obey

$$H^{(0)}\psi_{\pm\mu,k}^{(0)} = E_{\mu,k}^{(0)}\psi_{\pm\mu,k}^{(0)} \quad (\text{A.15})$$

where the states $\psi_{\mu,k}$ and $\psi_{-\mu,k}$ are degenerate.

By applying first order degenerate perturbation theory, we have to solve the following determinant

$$\begin{pmatrix} W_{\mu\mu} & W_{\mu-\mu} \\ W_{-\mu\mu} & W_{-\mu-\mu} \end{pmatrix} \quad (\text{A.16})$$

where

$$W_{\mu\mu} = W_{-\mu-\mu} = \langle \psi_{\mu,k} | H' | \psi_{\mu,k} \rangle = -V_0 |f(z_0, \theta_0)|^2 |A|^2 \quad (\text{A.17})$$

$$W_{\mu-\mu} = W_{-\mu\mu}^* = \langle \psi_{\mu,k} | H' | \psi_{-\mu,k} \rangle = -V_0 e^{2i\mu\theta_0} |f(z_0, \theta_0)|^2 |A|^2 \quad (\text{A.18})$$

The first order corrections are given by

$$E_{\pm} = \frac{1}{2} \left[W_{\mu\mu} + W_{-\mu-\mu} \pm \sqrt{(W_{\mu\mu} - W_{-\mu-\mu})^2 + 4|W_{\mu-\mu}|^2} \right] \quad (\text{A.19})$$

for which the solutions are

$$\begin{aligned} E_+ &= -2V_0 |A|^2 |f(z_0, \theta_0)|^2 \\ E_- &= 0 \end{aligned} \quad (\text{A.20})$$

Which means that one state has an energy change equal to E_+ and the other remains in the same, which agrees with our *ab initio* results (see Fig. 3.4).

The split is then given by

$$\Delta E = |E_+ - E_-| = 2V_0 |A|^2 |f(z_0, \theta_0)|^2 = \frac{2V_0 |f(z_0, \theta_0)|^2}{N_{cells} I} \quad (\text{A.21})$$

The important feature to observe here is that this split is proportional to N_{cells}^{-1} . In our DFT and GW calculations, by changing the supercell size, we observed splits $\propto N_{cells}^{-1}$

converging to 0 when supercell size goes to infinity. The impurity band goes to a constant value and the bandgap does not change substantially. Those trends are summarized in Fig. 3.6.

Another important observation is that the splits in the above equation are proportional to the electronic density $|f(z_0, \theta_0)|^2$ in the (z_0, θ_0) point. In Fig. 3.10 we observed that the bands for which the wavefunctions have maximum density (nodes) for $\theta = 0$ had (did not have) energy variations.

We now introduce the impurity wave function, following an effective mass approach, as

$$\psi_i(z - z_i) = F(z - z_i)\psi_{c(v)}(z - z_i) \quad (\text{A.22})$$

where we use $\psi_{c(v)}$ if we are dealing with a donor (acceptor) impurity and its eigenvalue is E_i , and it is located between the last valence band and the first conduction band. Based on our *ab initio* results we choose $F(z - z_i) = (1/\sqrt{\pi}\sigma_z)e^{-(z-z_i)^2/\sigma_z^2}$

Based on our results for CNT(10,0)-H (see section 3.5) we may write the exciton composed by the impurity state as

$$\Psi(z_e - z_h) = \sum_k A(k)\psi_i(z_{e(h)} - z_i)\psi_{v(c)}(z_{h(e)}) \quad (\text{A.23})$$

which is equal to

$$\Psi(z_e - z_h) = F(z_{e(h)} - z_i) \sum_k A(k)\psi_{c(v)}(z_{e(h)} - z_i)\psi_{v(c)}(z_{h(e)}) \quad (\text{A.24})$$

After some algebra, we obtain:

$$\Psi(z_e - z_h) = \frac{\tilde{A}_0\Delta k}{LR\sigma_z} e^{-\left(\frac{z_{e(h)} - z_i^2}{\sigma_z^2}\right)} e^{2i\mu\theta} e^{-\left(\frac{z_e - z_h}{2/\Delta k}\right)^2} \quad (\text{A.25})$$

and the probability density is given by

$$\rho_{ex}(z_e - z_h) \propto e^{-\left(\frac{z_{e(h)} - z_i}{\sigma_z/\sqrt{2}}\right)^2} e^{-\left(\frac{z_e - z_h}{1/\Delta k}\right)^2} \quad (\text{A.26})$$

Notice that the excitonic wavefunction in this case displays an interplay between the dynamics of the electron-hole pair and the localization induced by the impurity.